

Microscale Cavitating Flow Patterns and Spray
Characteristics with Applications

by
Morteza Ghorbani

Submitted to the Graduate School of Engineering and Natural Sciences
in partial fulfillment of
the requirements for the degree of
Doctor of Philosophy

Sabanci University

January 2017

MICROSCALE CAVITATING FLOW PATTERNS AND SPRAY
CHARACTERISTICS WITH APPLICATIONS

APPROVED BY:

Prof. Dr. Ali Koşar
(Thesis Supervisor)



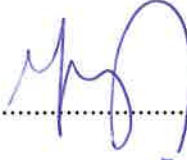
Prof. Dr. Mustafa Ünel



Assoc. Prof. Dr. Mehmet Yıldız



Prof. Dr. Asiye Işın Doğan Ekici



Asst. Prof. Dr. Hüseyin Üvet



DATE OF APPROVAL: 06/01/2017

© Morteza Ghorbani 2017
All Rights Reserved

Microscale Cavitating Flow Patterns and Spray Characteristics with Applications

Morteza Ghorbani

Mechatronics Engineering, PhD Thesis, 2017

Thesis Supervisor: Prof. Ali Koşar

Abstract

Spray formation occurring at the outlet of short micro/mini-orifices due to the cavitation phenomenon is of great importance in biomedical and engineering applications. Recent studies show the destructive effect of the energy released from the collapse of cavitation bubbles, which are generated in micro domains, on the targeted surfaces. The cavitation phenomenon occurs at low local pressures within flow restrictive elements and strongly affects fluid flow regimes inside micro-channels which results in spray formation. Extended cavitation bubbles toward the outlet of the micro-channel, droplet evolution, and spray breakup are among crucial mechanisms to be considered in spray structure. In this study, spray formation and atomization, bubble and droplet evolution, break-up, and corresponding cavitating flow at the outlet of short micro/mini-channels are discussed at different physical and thermo-dynamical conditions. Cavitation phenomenon inside micro/mini-channel configurations are numerically investigated in detail. The results of this study show that the static pressure drops down to a very low magnitude (tensile stress) in micro-channels while the minimum static pressure in mini-channels is found to be equal to vapor saturation pressure, and higher velocity magnitudes particularly at the outlet are visible in the micro-channels. It is shown that for higher upstream pressures, the cavitating flow extends over the length of the micro/mini-channel thereby increasing the possibility of collapse at the outlet. A detailed study on the effect of energy associated with turbulence is investigated at high Reynolds numbers for both

micro/mini-channels and its impact is analyzed using wall shear stress, turbulence kinetic energy and mean velocity at various locations of the channels. We find that there is a considerable difference on the flow regime between the emerging sprays at the outlet of the channels in micro and mini/macro scales. The spray at the outlet of nozzle has a conical shape with separated droplet/bubbles, however, interestingly the spray shape entirely differs in macro scale presenting spray jet flow regime at the same thermo-physical conditions. We showed that with the aid of the hydrodynamic cavitation in a low-cost and clean system, the spray jet has the capability of heat generation in contrast to the common use of spray jet in the cooling applications. The emerging spray is under the effect of the micro scale cavitating flow inside the micro/mini-channels which is much more intense in comparison to its correspondence at macro scale. The temperature measurements on a black-covered aluminum plate subjected to the spray interestingly show a considerable increase for a specific micro-channel. This temperature rise would be potentially utilized as a power source in miniature electric appliances with a simple energy conversion device. Herein, we present a complete set of numerical and experimental results on the micro/mini scale cavitating flow, spray emergence and its interaction with a solid body which will increase our understanding about the physics of the cavitating flow inside the micro/mini-channel and its relation with the emerging spray structure.

Keywords: Cavitation; Spray; Micro/Mini-Channel; Turbulence; Energy; Collapse

Mikro Boyutlu Kaviteasyon Akış Modelleri ve Sprey Özellikleri ile Uygulamaları

Morteza Ghorbani

Mekatronik Mühendisliği, Doktora Tezi, 2017

Tez Danışmanı: Prof. Ali Koşar

Özet

Kaviteasyon olayı nedeniyle kısa mikro / mini deliklerin çıkışında oluşan püskürtme oluşumu, biyomedikal ve mühendislik uygulamalarında büyük önem taşımaktadır. Son zamanlarda yapılan çalışmalar, mikro alanlarda oluşturulan kabarcıklarının çökmesinden ıkan enerjinin hedeflenen yüzeylerde tahrip edici etkisini göstermektedir. Kaviteasyon olayı, akış sınırlayıcı unsurlar içindeki düşük yerel basınçlarda ortaya çıkar ve mikro kanallardaki sıvı akış rejimlerini sprej oluşumuyla sonuçlanan şiddetle etkiler. Mikro kanalın çıkışına doğru uzatılmış kaviteasyon kabarcıkları, damla gelişimi ve sprej parçalanması, sprej yapısında dikkate alınması gereken önemli mekanizmalardır. Bu çalışmada, kısa mikro / mini kanalların çıkışında sprej oluşumu ve atomizasyon, kabarcık ve damlacık gelişimi, parçalanma ve bunlara karşılık gelen kaviteasyon akışı, farklı fiziksel ve termodinamik koşullarda tartışılmıştır. Mikro / mini kanal konfigürasyonlarındaki kaviteasyon olayı sayısal olarak ayrıntılı bir şekilde incelenmiştir. Bu çalışmanın sonuçları, mikro kanallarda statik basınçın çok düşük bir gerilime (çekme gerilmesi) düştüğünü, mini kanallardaki minimum statik basınç, buhar doyum basınçına eşit olduğunu ve özellikle de mikro kanal çıkışında daha yüksek hız büyüklüklerine sahip olduğunu göstermektedir. Daha yukarı akış basınçlarında kaviteasyon akışı, mikro / mini kanalın uzunluğu boyunca uzanır ve böylece çıkışta çökme olasılığı artar. Türbülans ile ilişkili enerjinin etkisi üzerine ayrıntılı bir çalışma, mikro / mini kanallar için yüksek Reynolds sayılarıyla araştırılmış ve etkileri, kanalların çeşitli yerlerinde, duvar kayması gerilmesi, türbülans

kinetik enerjisi ve ortalama hız kullanılarak analiz edilmiştir. Mikro ve mini / makro ölçeklerde kanalların çıkışında ortaya çıkan spreylere arasındaki akış rejimi üzerinde önemli bir fark olduğunu buluyoruz. Püskürtme ağzı çıkışındaki püskürtme, ayrılmış damlacık / kabarcıklarla konik bir şekle sahiptir; ancak ilginç bir şekilde, püskürtme şekli, aynı termo-fiziksel koşullarda püskürtme jeti akış rejimini sunan makro ölçekte tamamen farklıdır. Düşük maliyetli ve temiz bir sistemdeki hidrodinamik kaviteasyonun yardımıyla püskürtme jetinin, soğutma uygulamalarında püskürtme jetinin ortak kullanımından farklı olarak ısı üretme kabiliyetine sahip olduğunu gösterdik. Ortaya çıkan spreylere, mikro / mini kanallardaki mikro boyuttaki kaviteasyon akışının etkisindedir ve makro ölçekte yazışmalara kıyasla çok daha şiddetlidir. Sprey uygulanan siyah kaplı bir alüminyum plakadaki sıcaklık ölçümleri ilginç bir şekilde belirli bir mikro kanal için önemli bir artış göstermektedir. Bu sıcaklık artışı, potansiyel olarak basit bir enerji dönüştürme cihazı ile minyatür elektrikli cihazlarda bir güç kaynağı olarak kullanılabilir. Burada, mikro / mini ölçekli kaviteasyon akışı, spreylere ortaya çıkışı ve katı cisim ile etkileşimi ile mikro / mini kanaldaki kaviteasyon akışının fiziği ve ortaya çıkan spreylere yapısı ile olan ilişkisi hakkındaki bulgularımızı artıracak olan sayısal ve deneysel sonuçların eksiksiz bir dizisi sunulmaktadır.

Acknowledgements

Firstly, I would like to express my sincere gratitude to my advisor Prof. Dr. Ali Koşar for the continuous support of my Ph.D study and related research, and for his patience, friendship, and immense knowledge. His excellent guidance enabled me to perform high quality research and to write this thesis.

I would like to thank my thesis committee members: Prof. Dr. Mustafa Ünel, Assoc. Prof. Dr. Mehmet Yıldız, Prof. Dr. Asiye Işın Doğan Ekici and Asst. Prof. Dr. Hüseyin Üvet for their invaluable comments and suggestions on my thesis. In particular, I am grateful to Prof. Ünel and Prof. Yıldız for sharing their knowledge and providing tremendous help during my doctoral studies. I had fruitful discussions with Prof. Ünel about several imaging concepts, computer vision techniques and important mathematical tools that significantly enhanced the content of this thesis. Prof. Yıldız provided enormous help on modeling and computational aspects of my thesis work.

My sincere thanks also goes to Asst. Prof. Dr. Luis Guillermo Villanueva, who provided me an opportunity to join his team as a visiting Ph.D student, and who gave access to the laboratory and research facilities at Ecole Polytechnique Federale de Lausanne (EPFL).

I thank my fellow labmates; Abdolali Khalili Sadaghiani, Mostafa Shojaeian, Ali Mohammadi, Ahmadreza Motazakker, Sarp Akgonul, Yagmur Sisman and Merve Zuvin at the Microfluidics and Microthermal Systems Laboratory for the great environment they provided me in terms of both research and friendship. I also want to thank Gokhan Alcan and Canberk Sozer for their friendship and collaboration in the context of TUBITAK 1003 project. Likewise, I have to acknowledge Gamze Tillem for the support she provided whenever I need her.

I also want to mention my gratitude to my friends Vahid Tavakkoli Aghaei, Sonya Javadi, Ebru Demir and Fereshteh Hojatisaeidi for encouraging me in all parts of my graduate education.

Last but not the least, I would like to thank to my parents Karam Ghorbani and Sakineh Balaghi, my brothers Reza Ghorbani, Nima Balaghi, Sasan Akbarpour, Ali Falahat, Mohsen Rostami and Manouchehr Nasreisfahani, my sisters Leila Ghorbani, Mina Ghorbani and Rana Ghorbani and, my niece and nephew Nazli Falahat and Amirmohammad Rostami. I am grateful for their unlimited love and support throughout my life.

My research was supported by the TUBITAK (The Scientific and Technological Reserach Council of Turkey) through the TUBITAK 1003 Project-113S092.

Contents

1	Introduction and Motivation	1
1.1	Cavitation Phenomenon	1
1.1.1	Cavitation Versus Boiling	2
1.1.2	Nucleation and Growth of Bubbles	3
1.2	Motivation	5
1.2.1	Objectives of this study	9
1.2.2	Thesis Structure	10
2	State-of-the-art Literature Review	11
2.1	Cavitating Flow inside the Constrictive Elements	11
2.2	Spray Characteristics under the Effect of the Cavitation Phenomenon .	16
2.3	Lithotripsy and Cavitation in Urinary Stone Therapy	21
2.3.1	Urinary Stone Therapy Using Lithotripsy and Ultrasound Cav- itation	22
2.3.2	Shock Wave Lithotripsy (SWL)	23
2.3.3	Secondary and Tandem Shock Waves in SWL	25
2.3.4	Cavitation Effects on SWL	29
2.4	An Alternative for Ultrasound Cavitation; Hydrodynamic Cavitation	31
2.5	Side Effects and Limitations in Biomedical Use of Ultrasound and Hydrodynamic Cavitation	34
3	Numerical Simulations of Cavitating Flow Inside Micro and Mini- Channels	39
3.1	Introduction	39
3.2	Numerical Modelling	40

3.2.1	Model Equations	40
3.2.2	Cavitation modeling in cavitating flow configuration	41
3.2.3	Numerical Validation Test Case: Micro-Jet Impingement	44
3.2.4	Estimation of Uncertainty due to Discretization Error Using Grid Convergence Index	44
3.2.5	Modeling Cavitating Flows in Micro/Mini-Channels	47
3.3	Results and Discussion	50
3.3.1	Micro-Jet Impingement	50
3.3.2	The effect of Turbulence on the Fluid Flow Regime Inside Micro/Mini-Channels	52
3.3.3	The Pressure Variations Inside Micro-channels with Different Diameters	56
3.3.4	The Variation of the Vapor Volume Fraction Inside Channels with Different Diameters	62
3.3.5	Numerical Analysis of Bubble Number Density (BND)	63
3.3.6	The Effect of Bubble Number Density on Cavitation	66
3.3.7	Hydraulic Characteristics of Cavitating Flows with the Bubble Number Density of 1.0e13	68
4	Spray at the Outlet of the Micro-Channel under the Effect of the Cavitation Phenomenon	71
4.1	Introduction	71
4.2	Experimental Procedure and Setup	72
4.2.1	Hydrodynamic Cavitation	73
4.2.2	High Speed Imaging System	74
4.3	Results and Discussion	75
4.3.1	Spray Characteristics under the Effect of the Cavitation Phe- nomenon	75
4.3.2	Structure of the Spray for Various Pressures at Different Seg- ments	79
4.3.3	A Correlation; Pressure Drop in the Presence of Cavitation Phenomenon	88
4.3.4	Flow Pattern Classification at the Outlet of The Micro-Channel	90

5	Spray Collapse at the Outlet of the Micro-Channel	93
5.1	Introduction	93
5.2	Methods and Materials	94
5.3	Results and Discussion	96
5.3.1	Spray Structure at the Outlet of the Micro-channel at Different Upstream Pressures	96
5.3.2	Collapse of the Cavitation Bubbles	99
5.3.3	Collapse of Cavitation Bubbles: An Application Case Study	102
6	Energy Harvesting in Micro Scale with Cavitating Flow	107
6.1	Introduction	107
6.2	Experimental Procedure and Characterization	108
6.2.1	Device Characterization	108
6.2.2	Experimental Procedure	109
6.2.3	Flow Characterization	110
6.3	Results and Discussion	110
6.3.1	Temperature Variation on a Solid Body under the Effect of Cavitating Flow	112
6.3.2	Flow Regimes Hysteresis from Micro to Macro Scale Cavitating Flow	116
6.3.3	Electric Power Output as a Result of the Heat Generation During the Spray Collision	119
7	Conclusion	122
8	Recommendations for Future Research	126

List of Figures

1.1	Schematic of occurrence of cavitation phenomenon in a flow restrictive element	3
1.2	Traveling bubble to the outlet of the micro-channel	8
1.3	Bubble detection inside a droplet for different upstream pressures (a) 10 <i>bar</i> (b) 100 <i>bar</i>	9
2.1	Schematic of a conical spray with detailed breaks and spray characteristics (Baumgarten 2006)	17
2.2	Nozzle flow and spray regimes at a channel with width of 4 <i>mm</i> and liquid temperature of 292 <i>K</i> (Sou et al. 2007)	18
2.3	Schematic of the Experimental Set-up (Ikeda et al. 2006). The Set-up Consists of an Acrylic water Tank, an Ultrasound Generation Unit and a Data Acquisition Unit	30
2.4	The Hydrodynamic Setup used to Fragment Kidney Stones (Perk et al. 2012)	33
3.1	The computational domain used in modeling micro-jet impingement for validation ($H/D=5$)	45
3.2	The skin friction coefficient for different cell numbers for the aspect ratio of 5	46
3.3	The second study domain for modeling the micro-channel ($D_m = 762 \mu\text{m}$)	48
3.4	Pressure coefficient as a function of Reynolds number for different aspect ratios (a) $H/D=2$ (b) $H/D=3$ (c) $H/D=4$ (d) $H/D=5$	51
3.5	The comparison of the pressure coefficient with the available numerical results in the literature	52

3.6	The velocity profile for different aspect ratios at $Re=500$ (a) $H/D=2$ (b) $H/D=3$ (c) $H/D=4$ (d) $H/D=5$	53
3.7	The variation of mean velocity on the lines inside the micro/mini- channels	54
3.8	The ratio of TKE for different upstream pressures. (a, b, c) the ratio of TKE of the micro-channel with the diameter of $152 \mu m$ to the micro-channels with diameter of $254 \mu m$, $504 \mu m$, and $762 \mu m$, respectively	55
3.9	Normalized Cavitation length for different channel diameters and pressure drops	57
3.10	Pressure variation for different upstream pressures on different lines ($D_m = 152 \mu m$)(a) $p_i = 10 \text{ bar}$ (b) $p_i = 30 \text{ bar}$ (c) $p_i = 80 \text{ bar}$ (d) $p_i = 150 \text{ bar}$	57
3.11	Pressure variation for different upstream pressures on different lines ($D_m = 254 \mu m$)(a) $p_i = 10 \text{ bar}$ (b) $p_i = 30 \text{ bar}$ (c) $p_i = 80 \text{ bar}$ (d) $p_i = 150 \text{ bar}$	58
3.12	Pressure variation for different upstream pressures on different lines ($D_m = 504 \mu m$)(a) $p_i = 10 \text{ bar}$ (b) $p_i = 30 \text{ bar}$ (c) $p_i = 80 \text{ bar}$ (d) $p_i = 150 \text{ bar}$	59
3.13	Pressure variation for different upstream pressures on different lines ($D_m = 762 \mu m$)(a) $p_i = 10 \text{ bar}$ (b) $p_i = 30 \text{ bar}$ (c) $p_i = 80 \text{ bar}$ (d) $p_i = 150 \text{ bar}$	60
3.14	Pressure variation for different upstream pressures and inner diame- ters on Line-1	60
3.15	Pressure variation for different upstream pressures and inner diameter on Line-3	61
3.16	Pressure profile inside the channels at an upstream pressure of 150 bar for (a) $152 \mu m$ (b) $254 \mu m$ (c) $504 \mu m$ (d) $762 \mu m$	62
3.17	Vapor volume fraction for channels with different inner diameters at upstream pressure of (a) $p_i = 10 \text{ bar}$ (b) $p_i = 30 \text{ bar}$ (c) $p_i = 80 \text{ bar}$ (d) $p_i = 150 \text{ bar}$	63
3.18	Computational domain of the study	64

3.19	Validation of the present numerical model against the results of Payri et al. 2004	65
3.20	Validation of the present numerical model against the results of Nurick 1976	66
3.21	Discharge coefficient for three bubble number density (BND) values as a function of time step	67
3.22	Transferred mass per bubble number density (BND) for different time steps	67
3.23	Vapor volume fraction contours for bubble number densities (BNDs) of 1.0e9, 1.0e11 and 1.0e13 at different time steps	68
3.24	Vortices in the cavitating flow for bubble number density (BND) =1.0e13 at the upstream pressure of 100 <i>bar</i>	69
3.25	Velocity profiles and vapor phase distributions near the outlet of the micro-channel	70
4.1	Experimental setup with the orifice throat and exit area	73
4.2	The variation of the flow rate with respect to the upstream pressure	76
4.3	The variation of the Cavitation number with respect to upstream cavitation	77
4.4	Spray cloud diameter at different segments for various upstream pressures	78
4.5	Detection of bubble/droplet contours under low inlet pressures	82
4.6	Detection of bubble/droplet contours under medium inlet pressures	83
4.7	Detection of bubble/droplet contours under high inlet pressures	84
4.8	Droplet size distribution at different segments of the liquid jet processed using active contour method for mean major axis length	85
4.9	Droplet size distribution at different segments of the liquid jet processed using active contour method for mean minor axis length	86
4.10	Non-dimensional pressure drop with respect to Reynolds number for single phase flow along with the predictions of the correlation of Cioncolini et al. 2015	89

4.11	Non-dimensional pressure drop with respect to Reynolds number for two phase flow data along with the predictions of the developed correlation	90
4.12	Emerging jets from the probe exit at different cavitation intensities .	91
4.13	Flow patterns in various locations at different Cavitation numbers . .	92
5.1	The evidence which shows the sensitivity of the spray cone angle with respect to the upstream pressure. First segments of the spray at the outlet of micro-channel were shown at upstream pressure of a) 10 <i>bar</i> , b) 50 <i>bar</i> , c) 80 <i>bar</i> , d) 100 <i>bar</i> and, the end of spray was shown at upstream pressure of e) 10 <i>bar</i> and f) 100 <i>bar</i>	95
5.2	Schematic of the experimental setup, the micro-channel configuration, and the spray structure at the outlet	96
5.3	Spray cone angle for different upstream pressures	97
5.4	Discharge coefficient for different upstream pressures	98
5.5	Spray at the outlet of the micro-channel for different segments ($p_i=10$ <i>bar</i>)	98
5.6	Spray at the outlet of the micro-channel for different segments ($p_i=30$ <i>bar</i>)	99
5.7	Spray at the outlet of the micro-channel for different segments ($p_i=50$ <i>bar</i>)	99
5.8	Spray at the outlet of the micro-channel for different segments ($p_i=80$ <i>bar</i>)	99
5.9	Spray at the outlet of the micro-channel for different segments ($p_i=100$ <i>bar</i>)	100
5.10	Spray at the outlet of the micro-channel for different segments ($p_i=120$ <i>bar</i>)	100
5.11	The collapse process along the spray length at the outlet of the micro-channel ($p_i=100$ <i>bar</i>)	101
5.12	The collapse process along the spray length at the outlet of the micro-channel ($p_i=120$ <i>bar</i>)	102
5.13	Schematic of the proposed technique	103

5.14	Reduction ratio of nanoparticles size as a function of the Cavitation number	105
6.1	A schematic of the proposed system for generating the cavitation bubbles and spray emergence under the effect of the cavitation	109
6.2	Thermal counters captured by thermal camera on the solid surface for (a) without spray apply (152 μm) (b) At the time of first collision (152 μm), (c) 30 seconds after the collision (152 μm), (d) without spray apply (504 μm), (e) At the time of first collision (504 μm), (f) 30 seconds after the collision (504 μm)	112
6.3	The temperature variation on the solid surface with respect to the upstream pressure for (a) just on the time of spray collision on the surface, (b) 30 <i>seconds</i> after the collision, (c) 120 <i>seconds</i> after the collision	115
6.4	The spray flow regime at the outlet of the micro/mini-channels for different upstream pressures and at first and last segments of the spray structure	117
6.5	The output power produced as a result of the thermal energy creation on a solid surface subjected to the cavitating induced spray	120
8.1	Design and surface behavior of the recommended system. (a) Overall structure of the cavitating nozzle vibrator (b) The extended channels to study the collapse and interaction between solid-fluid-bubble (c) Surface roughness indication	127
8.2	The interaction between spray and the targeted areas at different conditions for kidney stone and prostate tissue	128

List of Tables

1.1	Studies related to single and multiphase flows under laminar and turbulent flow conditions	7
2.1	Preliminary Significant Reports in SWL	25
2.2	Summary of Tandem Shock Wave Studies	28
2.3	Cavitation Contribution in SWL	31
2.4	Summary Of Studies on Hydrodynamic Cavitation in Biomedical Applications	35
2.5	Summary of Studies in Relation with SWL Side Effects	37
2.6	Mechanisms of Stone Fragmentation in SWL	38
3.1	Results of skin friction coefficient for different grid spacing sizes	47
3.2	Grid convergence index (GCI) for different Reynolds numbers	48
3.3	Wall shear stress (Pa) for different channels at low and high upstream pressures	56
3.4	The cavitation number for the first three lines across different micro/minichannels	62
4.1	Uncertainties in experimental parameters	74
4.2	Standard deviation and eccentricity of the processed droplets using active contour method at different segments for various upstream pressures	87
4.3	Droplet characteristics processed using active contour method at different segments for various upstream pressures	88
6.1	The electrical characteristics of some miniature daily-used energy-harvesting devices	121

Nomenclature

Roman Symbols

Symbol	Units	Description
A	[m ²]	Cross-sectional Area
a	[m/s]	Speed of sound
c	[J/K]	Heat capacity
C	[–]	Constant
C_f	[–]	Friction factor
C_p	[–]	Pressure coefficient
D	[m]	Diameter of channel
E	[–]	Solution error
E_s	[Kg/m · s ²]	Young modulus
f	[–]	Function
fl	[m]	Focal length
\vec{f}	[N]	Body force
F	[–]	Factor
\vec{g}	[m/s ²]	Gravitational Acceleration
G	[m ² /s ²]	Generation of TKE
Gb	[–]	Gibbs number
h	[m]	Grid Spacing
H	[KJ/Kg]	Enthalpy
H	[m]	Height
i	[–]	Iteration
I	[A]	Current
J	[–]	Nucleation rate

J_0	[–]	Factor of proportionality
k	[m ² /s ²]	Turbulent kinetic energy
K	[–]	Pressure drop
l	[m]	Thickness
L	[m]	Length
LH	[KJ/Kg]	Latent heat of evaporation
m	[Kg]	Mass
\dot{m}	[Kg/s]	Mass flow rate (transfer)
M	[times]	Magnification
Ma	[–]	Mach number
n	[–]	Number of bubbles
N	[–]	Total number of cells
Oh	[–]	Ohnesorge number
p	[bar]	Pressure
P	[W]	Power
Pr	[–]	Prandtl number
q	[J]	Heat energy
r	[–]	Order of Convergence
R	[m]	Radius of bubble
Re	[–]	Reynolds number
Res	[Ω]	Resistance
s	[Kg/s]	Mass transfer source term
S	[N · s/m]	Surface tension
S	[–]	Mean rate of strain tensor
S_k, S_ϵ	[–]	User defined source terms
t	[s]	Time
T	[K]	Temperature
u	[–]	Constant refinement ratio
v	[m/s]	Velocity magnitude
\bar{V}	[m/s]	Mean velocity
\vec{V}	[m/s]	Mass averaged velocity
W	[J]	Net energy

x	[-]	Local vapor quality
X	[m]	Distance from the nozzle
Y_M	[-]	Fluctuating dilatation

Greek Symbols

Δ	[-]	Difference
ρ	[kg/m ³]	Density
σ	[-]	Cavitation number
α	[-]	Volume fraction
μ	[Pa · s]	Dynamic viscosity
ϵ	[-]	Turbulence dissipation rate
ν	[m ² /s]	Kinematic viscosity
γ	[-]	TKE ratio
ζ	[-]	Mesh quality indicator
τ	[Pa]	Shear stress
φ	[-]	Impulse of SWL

Subscripts

A	Acceleration
b	Bouyancy
B	Bubble
C	Critical
dr	Drift
D	Discharge
f, q	Phases
FR	Friction
g	Gravitational

<i>G</i>	Gas
<i>i</i>	Injection/Upstream/Inlet
<i>imp</i>	Impact
<i>in</i>	Initial
<i>jet</i>	Jet flow
<i>l</i>	Liquid
<i>m</i>	Micro/mini-channel
<i>o</i>	Outlet
<i>ref</i>	Reference
<i>s</i>	Solid
<i>S</i>	Safety
<i>t</i>	Turbulence
<i>T</i>	Mixture
<i>TP</i>	Two-phase
<i>v</i>	Vapor
<i>w</i>	Wall

Chapter 1

Introduction and Motivation

1.1 Cavitation Phenomenon

Cavitation is a direct consequence of static pressure reductions down to a critical value (vapor pressure), and leads to the formation of inchoate vapor/gas bubbles (cavitation inception) or large-scale attached cavities (Supercavitation) [1–3]. Cavitation is associated with the explosive growth and subsequent catastrophic collapse of vapor bubbles. Therefore, it is a dynamic phenomenon and its occurrence is not restricted to the fluid medium.

Cavitation occurs when a liquid is subjected to high pressure fluctuations. The pressure drop in ultrasound cavitation is a consequence of acoustic fields with sufficient intensity, while low local pressures as a result of constriction in the liquid flow direction generate hydrodynamic cavitation. The liquid is compressed in positive half cycle of the sound in a small region and is expanded during its negative half cycle. The generated vapor bubbles in the positive cycle collapse in the negative half cycle, and therefore, lead to a shock wave in the liquid as a result of energy released from the collapse of ultrasound cavitation bubbles. The additional pressures by the ultrasound cause an augmentation in the acoustic pressure in cavitation bubbles and make the collapse and hence fragmentation quicker, which is exploited in the disintegration of stones using ultrasound cavitation. The generated cavitation bubbles can experience low energy fluctuations as a result of the sound effect, which is called as non-inertial cavitation (stable cavitation). The inertial cavitation (transient cavitation) starts to form when the bubbles undergo higher energy fluctu-

ations. There is a threshold depending upon parameters relating to acoustic sound field and bubble behavior, which determines the incipient of inertial cavitation. The population of bubbles plays an important role in determination of stable and transient cavitation. While many applications such as cavitation erosion, cell killing and ultrasound shock wave exploit inertial cavitation, non-inertial cavitation may also take place depending on the bubble population and sound effect. In addition, if the initial bubble size is small, the bubble growth is affected due to high surface tension. In the case of the large initial bubble size, the bubbles growth would not be able to control the energy released from the collapse of the bubbles [4].

1.1.1 Cavitation Versus Boiling

Cavitation and boiling are two mechanisms in which the liquid rupture is happened. The pressure difference in the cavitation phenomenon between the liquid pressure and vapor saturated pressure at a roughly constant temperature is called the tension and the value at which the process of collision a liquid is considered the tensile strength (Δp_C). On the other hand boiling occurs when temperature increases to the saturation temperature at constant pressure, so the difference between the aforementioned temperatures is called superheat and the point at which the liquid rupture takes place is considered as critical superheat (ΔT_C). Therefore, although the physical mechanism of these phenomena is similar, but thermodynamic characteristics are different. The Clausius-Clapeyron relation is used to explain the relevance of superheat and tensile strength when their values are small:

$$\Delta T_C = \Delta p_C \cdot \frac{T}{LH \cdot \rho_v} \quad (1.1)$$

where ρ_v is the saturated vapor density and LH is the latent heat of evaporation.

The cavitation phenomenon has been investigated in many studies with applications in bioengineering, chemical engineering, micro-pumps, micro-valves and diesel injection engines [5,6]. Cavitation number is the basic parameter accounting for the intensity of cavitation:

$$\sigma = \frac{p_{ref} - p_v}{\frac{1}{2}\rho\bar{V}^2} \quad (1.2)$$

where p_{ref} is the local pressure, ρ is the density, p_v is the vapor pressure, and \bar{V} is the mean velocity at the flow restrictive element. Additionally, the discharge coefficient, which is another significant parameter in cavitating flows, is defined as the ratio of the actual discharge to the theoretical discharge and is computed using the mass flow rate and pressure drop. A schematic of occurrence of cavitation phenomenon is displayed in Figure 1.1, where a recirculation zone is generated as a result of emerging bubbles in a low pressure region. Above and below the recirculation zone, vena contracta is formed and causes a decrease in the cross-sectional area at the constriction.

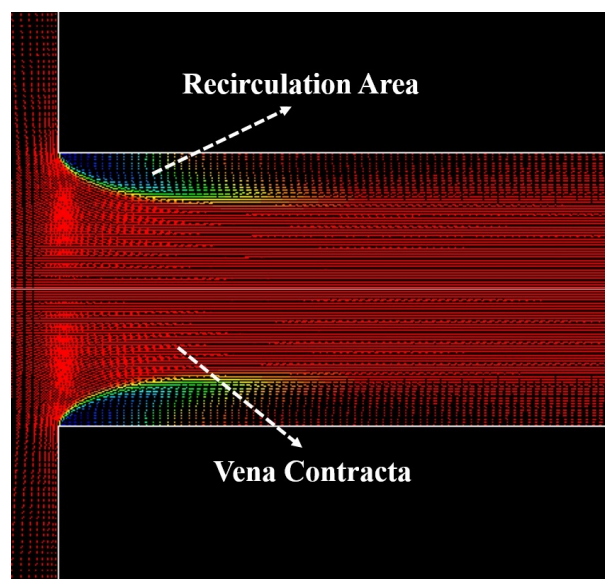


Figure 1.1: Schematic of occurrence of cavitation phenomenon in a flow restrictive element

1.1.2 Nucleation and Growth of Bubbles

The nucleation in any experimental investigations may happen in two types. In the first type, thermal motion results in the formation of voids in the liquid medium which is considered as Homogeneous nucleation. The second type is Heterogeneous nucleation where the nucleation occurs between liquid and small particles and also at the boundaries of the liquid with the solid interface.

Three sets of equations present the bubble dynamics in the Homogeneous nucleation. The first row of these relations manifests the relevance of surface tension

with pressure difference of the void as follows:

$$p_B - p = \frac{2S}{R} \quad (1.3)$$

where S is the surface tension, p is the liquid pressure, R is the bubble radius and p_B is the bubble's interior pressure. To prevent the rupture of bubble, the bubble's interior pressure must be less than $p_v - 2S/R$, since raising the pressure would lead to growth the bubble, R will rise, to maintain the equilibrium condition and hence, collision may occur. Therefore, there would be a critical bubble radius which shows the maximum size of the radius prior to collapsing the void. The term included in Equation 1.3 is considered as tensile strength when the bubble reaches its critical value:

$$\Delta p_C = \frac{2S}{R_C} \quad (1.4)$$

The second set provides the relations on the energy deposited in the liquid medium to form the bubbles. In this step, the energy required to be deposited at the surface of the bubble, $4\pi R_C^2 S$, is firstly computed and then the work done by the system to move the liquid in order to constitute the bubble, $4\pi R_C^3 \Delta p_C / 3$, is subtracted. Thus, the net energy to generate the bubbles after eliminating R_C with the aid of Equation 1.4 is expressed as follows:

$$W_C = \frac{16\pi S^3}{3(\Delta p_C)^2} \quad (1.5)$$

The final expression provides the probability of occurrence of the energy deposition at the available time. In this step, the net energy is connected to the kinetic energy of the molecules and the nucleation rate, J , is expressed with respect to the Gibbs number, G_b , as follows:

$$J = J_O \cdot e^{-G_b} \quad (1.6)$$

where J_O is some factor of proportionality.

The relations above is valid when the bubble is free of any contaminant and dissolved gas which is practically impossible. If nucleation site contains some gas,

then the pressure stated in Equation 1.3 is changed to the following relation:

$$p = p_v + p_G - \frac{2S}{R} \quad (1.7)$$

where p_G is the gas pressure and $2S/R - p_G$ is considered as the critical tension. The importance of the gas pressure is manifested when its value is high enough to neglect the tensile strength. In this case the bubbles would have the ability to grow at the pressure higher than the vapor pressure.

As mentioned above, the Heterogenous nucleation occurs at the boundaries and between the liquid and solid surfaces. Therefore, the pressure variations which is considered in the Homogeneous nucleation would be affected by the surface contact angles and surface roughness. To sume up, the parameters which should be controled during the cavitation bubble's nucleation are Cavitation number, the flow velocity, liquid temperature, liquid and surface qualities in terms of contaminants and roughness, respectively. While the cavitation may practically characterized in term of the flow dynamics, but it is almost impossible to control the cavitation process in term of the aforementioned parameteres particularly when the cavitation bubbles start to constitute (incipient cavitation).

1.2 Motivation

Investigation of cavitating flows in micro and mini domains are of great importance in microfluidic systems. The effect of the caviation bubbles on the fluid flow regime and its relation with the emerging spray structure are the first step to understand the role of the cavitation in the microfluidic devices.

The preliminary results revealed that the cavitating flow at the outlet of the micro-channel depending on the pressure difference has a destructive effect on the abnormal tissues and stones. This was the first motivation of the project to discover detail of the cavitating flow inside the micro-channel and the spray at the outelt of it. Hence, various micro/mini-channels with different inner diameters are modeled while varying the injection pressure from 10 to 150 *bar* in the first phase. The vapor volume fraction is thoroughly taken into account as the crucial parameter, and its profile along the channels presented at different pressures. The static pressure was

displayed for different cases, and pressure recovery was also elaborated in order to prove the occurrence of the cavitation phenomenon and its presence even at the outlet of the micro-channel. This is for the first time that the effect of the turbulence using turbulence kinetic energy, wall shear stress and mean velocity were analyzed at high Reynolds numbers.

As can be seen in Table 1.1 which briefly summarizes some of the important experimental and numerical studies on cavitation phenomenon for different applications, most of these studies do not consider turbulence effect [7], use single phase models, and target low Reynolds numbers in micro scale conditions. Therefore, the effect of energy associated with turbulence, orifice size, flow patterns, high Reynolds number needs to be investigated in detail for the better design of energy efficient systems and devices for a variety of application in small scale ranging from diesel engines to microfluidic and energy conversion systems.

Table 1.1: Studies related to single and multiphase flows under laminar and turbulent flow conditions

Study	Inlet Diameter	Reynolds Number	Upstream Pressure		Cavitation Number	L/D	Classification	Potential Application
			Pressure Drop (<i>bar</i>)	or Pressure Drop (<i>bar</i>)				
Payri et al. [8]	170 μm	-	$p_i=300-800$	-	5.71	Single Phase and Cavitation	Diesel Injection Engines	
Desantes et al. [9]	880 μm	-	$p_i=250-750$	1115-1026	-	Single Phase and Cavitation	Diesel Injection Engines	
Sou et al. [10]	4 mm	45,000-78,000	-	1.57-0.52	4	Single phase and Cavitation	Diesel Engines and Rocket Engines	
De Giorgi et al. [11]	2.5 mm	35,000-801,000	$p_i=2-8$	5.2-1.34	3	Cavitation	Cryogenic Systems	
Perpar et al. [12]	1 mm	-	-	0.49-0.41	6	Cavitation	Hydraulic Devices	
Henry and Collicott [13]	0.127-1.525 mm	-	$\Delta p = 0.93 - 5.98$	-	1.96-10.71	Cavitation	Diesel Fuel Injectors	
Cioncolini et al. [14]	150 - 600 μm	6,000-25,000	-	-	1.87-6.93	Single Phase	Microfluidic Systems	
Rooze et al. [15]	100 - 300 μm	-	$p_i=10.8$	-	0.033-0.1	Cavitation	Hydraulic Devices	
Schlender et al. [7]	224 μm	18,613-62,404	$p_i=50-550$	0.0286-0.0025	1.78	Cavitation	Energy Efficient Systems	
Mishra and Pates [16]	11.5 μm	160-550	$\Delta p = 0.5 - 8.50$	3.644-0.284	1.7	Single Phase and Cavitation	Microfluidic Systems	

The findings of this study are believed to provide an improved understanding on cavitating flows in both micro and mini scale thereby helping design and development of economical, energy efficient and new generation energy conversion and microfluidic devices that can be used in lab on a chip systems, micro-injectors and therapies such as abnormal tissue (e.g., Benign prostate hyperplasia or tumors) ablation and kidney stone treatment [17–20].

Moreover, the first observations on the spray structure at the outlet of the micro-channel suggest that the created cavitation bubbles may move to the outlet as shown in Figure 1.2. This visual detection bolsters the possibility of collapse process at the outlet of the microchannel. Therefore, if it is proven that the cavitation bubbles travel to the outlet of the micro-channel, then there would be a good possibility to increase the rate of erosion of the abnormal tissues and stones. It is also observed that even for lower upstream pressures (10 *bar*), there are some tiny bubbles in nano scale at the outlet of the microchannel when the flow was cut off through the pressure valves Figure 1.3. The experiments for the higher upstream pressures exhibit that more cavitation bubbles exit from the microchannel. These cavitation bubbles are mostly in bigger scale compared to the low upstream pressure

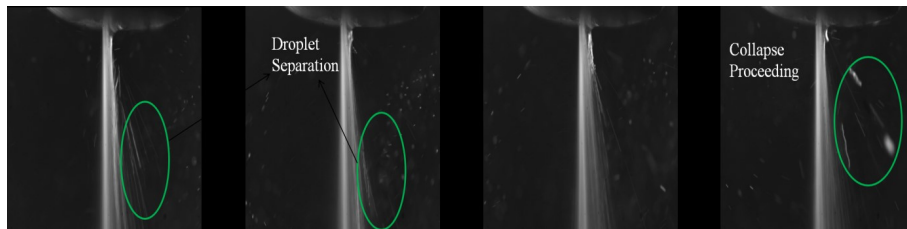


Figure 1.2: Traveling bubble to the outlet of the micro-channel

To identify these phenomena in a wide extent, spray structure at the outlet of the micro-channel is observed using high speed visualization system and utilizing Particle Shadow Sizing (PSS) imaging technique. The significance of the study of spray characteristics emerging from the micro-channel is to obtain a flow map in the micro scale and record the droplet breakup, droplet pattern, spray cone angle and collapse process. Therefore, the spray domain is classified to the segments starting from the outlet of a short micro-channel/micro-orifice. The visualization performed in this study helps to visualize the formation of spray in and to capture cavitation

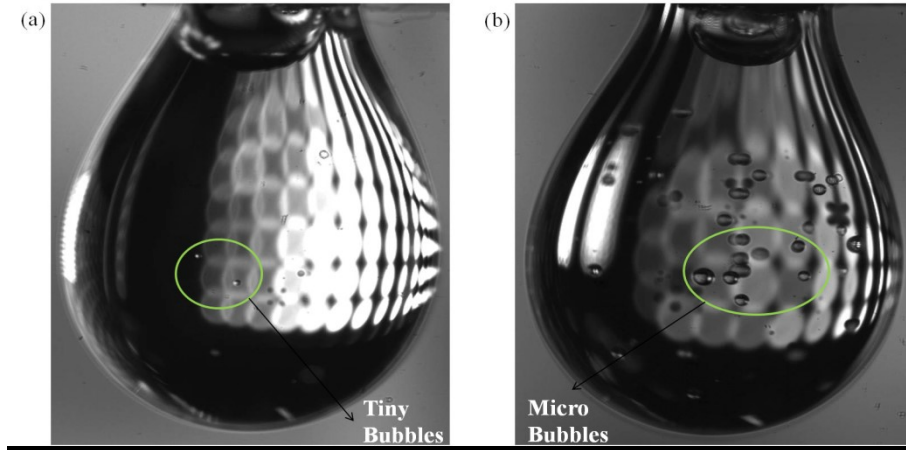


Figure 1.3: Bubble detection inside a droplet for different upstream pressures (a) 10 *bar* (b) 100 *bar*

droplets in micro scale. The results reported in this study about spray behavior have great potential in many biomedical and engineering applications.

1.2.1 Objectives of this study

The current study analyzes the flow inside the channel from numerical point of view from the inlet to the outlet and spray characteristics under the effect of the different mechanisms occurred inside the channel.

The objectives of this study are:

- To design, build and validate an extensive experimental facility;
- To manifest the flow regime difference between micro and macro scale cavitating flow;
- To provide a detailed information on the turbulence effect on the micro cavitating flow for high Reynolds numbers;
- To recognize the pressure recovery hysteresis along the micro/mini-channels;
- To identify the vapor volume fraction inside the micro/mini-channels;
- To investigate the bubble number density inside the channels and the amount of the bubbles survived from the channels to the outlet;

- To manifest the difference between the flow regimes of the sprays in micro and mini scales;
- To quantitatively analyze the droplet generation and evolution at the lower segments of the spray;
- To quantitatively characterize the heat generation due to the spray collision on a solid body;
- To evaluate the utilization feasibility of the proposed system on the fragmentation of the abnormal tissues.

1.2.2 Thesis Structure

This thesis is comprised of seven chapters: Chapter 2 presents a literature review and intro of available scientific studies relevant to this thesis. It includes the fundamental studies and significant improvements on the cavitating flow, spray formation and biomedical aspects of the proposed idea which clarify the rationale and direction of this study. Chapter 3 presents a depth numerical modelling of the problem with different user-defined functions for boundary conditions and the obtained results are illustrated with a detailed discussion. The experimental studies commence in Chapter 4 with a description of the proposed system and spray structure. The collapse process and its significance under the effect of the cavitation phenomenon are elaborated in Chapter 5. Chapter 6 is devoted to an entirely new idea in the field of cavitation about the heat generation and power production as a result of the spray collision on a solid body. Concluding remarks are reported in Chapter 7. Recommendations related to the output of this study with some preliminary results on the suggestions are provided in Chapter 8.

Chapter 2

State-of-the-art Literature Review

2.1 Cavitating Flow inside the Constrictive Elements

The cavitation phenomenon has been widely used in many industrial applications, and its significance in energy efficient devices such as diesel injection and rocket engines, microfluidic systems and energy conversion systems has been extensively reported. However, since scaling laws are not applicable to multiphase flows, in-depth numerical and experimental studies are of great importance to provide better understanding on cavitating flows in micro scale. The assessment of size effects is vital for the design and development of new generation microfluidic devices involving phase change. Hydrodynamic cavitation (HC), as a major phase change phenomenon, is considered a crucial parameter affecting the performance of fluidic devices and occurs when the static pressure of the fluid drops down to the vapor saturation pressure. As a result, the volume fraction of the vapor phase will increase along the channel, thereby generating a two-phase flow therein. Keller [21] claimed that the scaling relations can be extended to various cavitating flow regimes. Therefore, this study offers an explanation for the scaling effects on cavitation phenomenon.

The difference in flow characteristics between macro and micro scales not only affects hydrodynamic cavitation but also alters heat transfer and thermal-hydraulic performances as stated in literature [22]. Moreover, molecular approach is needed to investigate the fluid dynamic phenomena within the cavitation process. It was

experimentally shown that not only can the cavitation bubbles be formed inside the orifice, but also they can be present downstream of it or even move to the exit of the orifice [10,13].

The classification of flow regime in the macro scale flows is entirely different from the one in micro scale. The first parameters come to our mind in diminishing the size scale are surface and viscous effects. Two types of nuclei are frequently addressed in the literature called as free stream and surface nuclei. While the free stream nuclei play important role in the characterization of cavitation in conventional scale, surface nuclei dominate the flow in the micro scale due to their almost constant residence time despite the size reduction and their independent nature of the system size. Moreover, the surface forces become crucial in the micro scale cavitation, since the generated bubbles cannot grow beyond the boundaries and surface forces would not be neglected.

It is reported that the incipient cavitation number is much more smaller in micro scale cavitation in comparison to the corresponding macro scale one [16]. Therefore, there would need larger pressure difference between reference and vapor saturated pressures to instigate the cavitation. This phenomenon would definitely affect the later flow regimes including choked, super-cavitation and hydraulic flip. Moreover, due to the small magnitude of incipient number, the choked flow condition arrives quicker in the micro scale cavitating flow and therefore the range of the cavitation hysteresis between incipient and desinent cavitation would be dramatically affected. In addition, the surface effects lead to utilization of various materials in the micro scale. As it is well-known different materials are utilized in the microfluidic and MEMS-based applications.

Mala et al. [23] indicated a severe deviation in the flow characteristics of experiments from the conventional theory for the micro-tubes. The deviation was observed especially when Reynolds number increases, which lead to a significant increase in pressure gradient. Furthermore, they claimed that an early transition from laminar to turbulent flow occurred in micro scale. Garstecki et al. [24] reviewed the formation of gas bubbles in liquids in microfluidic systems using hydrodynamic techniques. They confirmed that the flow rate influenced the formation of bubbles during the transition from break-up controlled type to inertial type. Xiong et

al. [25] experimentally studied adiabatic two-phase flow patterns and void fraction in micro-channels. They examined the effect of micro-channel size on void fraction and recorded bubbly slug flow, slug-ring flow, dispersed-churn flow, and annular flow as flow patterns. By decreasing the size of micro-channels, the superficial velocity of the gas phase reached a higher value due to the effect of surface tension. Cubaud et al. [26] reviewed the micro-bubble formation in the microfluidic systems and expressed that the domination of the liquid pressure gradient over the vapor pressure gradient leads to decreased fluid volume fraction.

De Giorgi et al. [11] studied cavitation in conventional scale orifices at very high Reynolds numbers without considering the effect of turbulence, and the upper and lower bond of Cavitation and Reynolds numbers. Henry and Collicott [13] performed visualization in different micro and conventional channels at various pressure drops. They did not provide any information about the effect of turbulence and the pressure or velocity distribution inside orifices. Mishra and Peles [16] investigated cavitation and flow hysteresis in micro-channels. Although, they investigated the hydrodynamic cavitation in a micro-orifice and used the results of this study to make a comparison between micro and macro scale orifices, but the pressure drops and Reynolds numbers are rather low. Perpar et al. [12] used a channel with a diameter of 1 *mm* and focused on the bubbly flow inside the orifice. Although they presented some results regarding the pressure and velocity inside the orifice, the velocity of the flow was low. Rooze et al. [15] also investigated flows with cavitation bubbles in a small flow restrictive element while, the velocity inside the orifice was also low. Although high speed flows with high upstream pressures in the diesel injection engines were widely investigated in the literature [8,9], the effect of turbulence at high Reynolds numbers and cavitating nozzle flows at high upstream pressures were not extensively investigated in micro scale. Additionally, in micro scale, mostly single phase flows were considered at high Reynolds numbers [14], therefore, cavitation phenomenon as an important parameter in the energy efficient product and systems should be considered in details.

Numerical simulations of the cavitating flows inside channels were considered by many researchers in recent years [27–29]. In this regard, various modelling methods were employed to improve the understanding about the cavitating flow behavior

and emerging spray. There are important parameters affecting the flow simulation including bubble number density, velocity field and the nozzle geometry. Wang et al. [30] proposed a two-fluid cavitation model and simulated cavitating flows by developing the bubble number density model. Their model successfully predicted cavitation bubbles existing in the fluid flow inside a nozzle and correlated the discharge coefficient with cavitation number. Sou et al. [31] numerically simulated transient cavitating flows and combined Large Eddy Simulation (LES), Eulerian-Lagrangian Bubble Tracking Method (BTM), and the Rayleigh-Plesset (RP) equations in order to study cavitation incipience for sheet and cloud cavitation. Their model enabled to predict the recirculation zone at the inlet of the channel and the vortex shedding separated from the attachment point. The suggested model was capable of successfully simulating cavitating flows inside the channel, while spray formation was not numerically analyzed. Dietrich et al. [32] investigated the bubble formation of various liquids in three different shaped (involving cross-shape and two converging shapes) channels. They studied the size and shape of the bubbles for different flow rates, physical characteristics and mixer geometries. They found that the size of the bubble strongly depended on the geometry of the two-phase interface. They took the effect of the surface tension, liquid viscosity and flow rates on the bubble formation in account. Ming et al. [33] numerically studied the effect of cavitating flows inside a conical-spray injector using the mixture model. They concluded that the cavitation evolution dramatically affected the liquid sheet thickness and velocity at nozzle exit, which could further significantly change the spray angle and droplet Sauter mean diameter (SMD). Battistoni et al. [34] investigated unsteady injector flow and spray characteristics of different fuels. Their results indicated that vapor pressure had a minor impact on SMD of emerging spray in comparison to the mass flow rate and outlet liquid volume fraction. Shibata et al. [35] correlated the flow under the effect of cavitation inside a channel with the atomization of the liquid jet at the outlet of the jet. They analyzed separation of the cavitation from the main cavitating flow by Fourier transform and concluded that the separation of cavitation is an important parameter in the enhancement of jet atomization. Cavitating flows in nozzles of diesel injection engines were widely studied in the literature [36, 37]. Kanfoudi et al. [38] proposed a mixture model for the steady cavitating flow in-

side nozzles of diesel injection engines. They used Navier-Stokes equations for the mixture of the liquid and vapor to study the effect of the numerical and physical parameters on cavitating flows and used the pressure variation effects to investigate the change in the evaporation and condensation processes. The bubble dynamics in the cavitating flow inside nozzles of the diesel injection engines plays an important role on the progress and collapse of the created cavitation bubbles. In this regard, Bicer et al. [39] proposed an improved Rayleigh-Plesset equation to study the bubble, growth and collapse, and validated their model using the radius of the generated bubbles by comparing the numerical results to the experimental ones.

Although spray effects due to the cavitation and their applications have been studied in the literature to some extent, spray characteristics and cavitating flow behavior in micro scale have not been taken into account in a wide range of experimental conditions. Furthermore, sprays main properties and significant locations along the spray were mainly investigated from a numerical point of view [40]. Spray visualization displaying the spray morphology has not been considered, and instead, numerical approaches were present for displaying spray formation [41]. Although there are some studies simultaneously considering the numerical simulation of the cavitation formation and spray collapse [42], experimental investigations are still necessary to study the structure of the spray and processes affecting the atomization i.e, collapse in the micro scale. Dollet et al. [43] showed that geometrical parameters had a significant effect on the bubble formation in rectangular channels. They claimed that the linear 2D collapse of the bubble was stable in disturbance of the two-phase interface, while the 3D pinch-off part of the bubble collapse was unstable and led to bubble polydispersity. Che et al. [44] focused on droplet break-up to measure the size and number of daughter droplets. They observed that the break-up process depended upon the interaction between interfacial tension and shear force. They also found that the break-up process could be controlled by varying the flow rate of the continuous phase and mother droplets size. Agarwal et al. [45] studied the cavitating flow from numerical point of view and experimentally investigated the spray characteristics for different fuels. They used the mixture model to simulate the flow containing liquid, vapor and non-condensable gases and employed the k-model for the turbulence. They utilized the Rayleigh-Plesset equation to study the

evaporation and condensation processes. They also visualized the emerging spray for different fuels at the outlet of the nozzle and showed that the cavitation phenomenon reduces the mass flow rate of the fuel entering to the combustion chamber. He et al. [46] studied the effect of the cavitation bubbles on the formed near-nozzle spray and showed that the collapse process is a significant parameter affecting the cone angle of the spray. They illustrated that when the collapse of the cavitation bubbles took place inside the nozzle, the fluid flow inside the nozzle became more turbulent and the cone angle of the spray decreased. However, the cone angle of the spray dramatically increased when the collapse process occurred outside of the nozzle.

2.2 Spray Characteristics under the Effect of the Cavitation Phenomenon

Spray formation and its structure are of great importance in many engineering and industrial applications and typically include liquid jet formation, primary and secondary breakups, droplet evolutions and bubble collapse. One of the most significant parameters affecting spray characteristics is cavitation bubbles, which are generated inside a flow restrictive element, may extend to the outlet, and impact the spray by energy released during the collapse process. Small bubbles and particles as the contaminant have catastrophic effects on the efficiency of various processes such as the semiconductor cleaning. Hence, the studies dealing with reducing the size of these particles and removing the instability of the bubbles using the ultrasound technology are crucial in such systems.

Schematic of a high-pressure conical spray is shown in Figure 2.1 [47]. This figure shows the bottom part of an injector with sac hole needle and injection hole. As it is illustrated, the fluid starts to break inside a conical sprat just after the tip of the nozzle, which is called primary break-up. The primary break-up leads to creation of big droplets/bubbles which makes the region close to the nozzle dense and thick. The next step is secondary break-up where smaller droplets/bubbles are generated from the big droplets/bubbles. The secondary break-up occurs due to the aerodynamic forces existed on the relative velocity between droplets/bubbles

and the surrounding's gas. Aerodynamic forces decrease the droplets velocity and droplets at the vertex of the spray tolerate much more drag forces. Therefore, The droplets at the tip of the nozzle change to new ones consistently and the spray penetration increases.

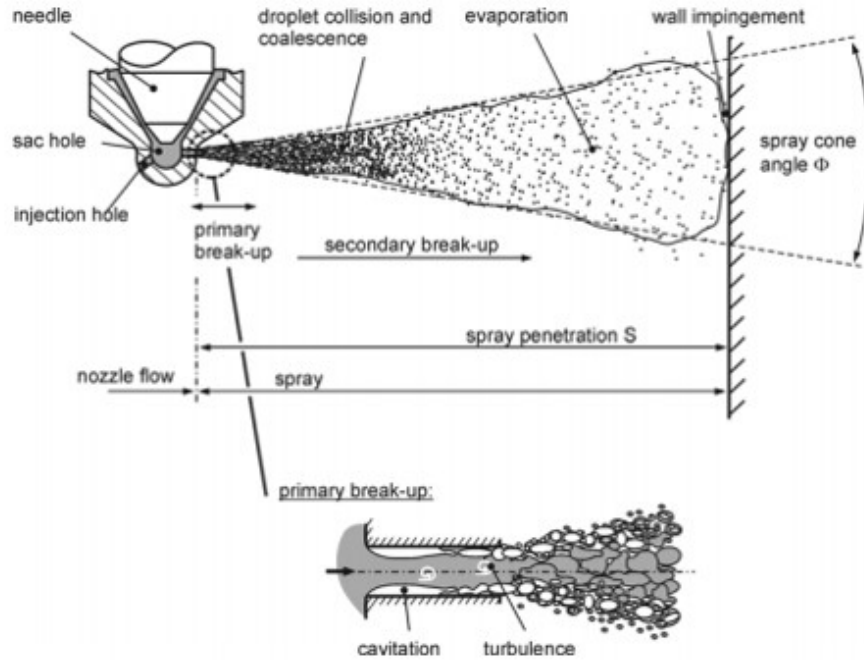


Figure 2.1: Schematic of a conical spray with detailed breaks and spray characteristics (Baumgarten 2006)

A typical classification of the spray at the outlet of a conventional nozzle was shown in a study by Sou et al. [10]. They classified the nozzle flow as no cavitation, developing cavitation, super-cavitation and hydraulic flip and, classified spray as wavy jet, spary and flipping jet as shown in Figure 2.2.

In last decades, hydrodynamic cavitation as an alternative approach to ultrasound cavitation was considered by many researchers, and cavitation bubbles and cavitation patterns were experimentally visualized in transparent nozzles [16]. Payri et al. [48] visualized cavitation bubbles at the outlet of an orifice using the special near-nozzle field visualization technique with the aid of a test rig pressurized with fuel. They attempted to investigate the effect of the nozzle geometry on cavitation patterns and the spray formation. It was observed that the cavitation inception and choked flow conditions were dependent on pressure, and the spray cone an-

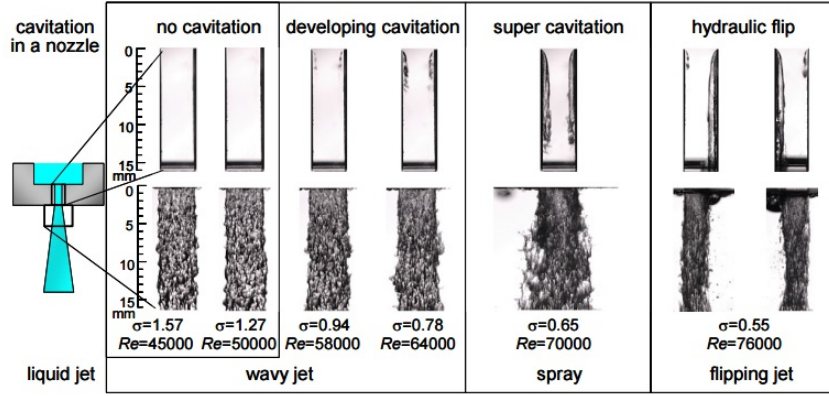


Figure 2.2: Nozzle flow and spray regimes at a channel with width of 4 mm and liquid temperature of 292 K (Sou et al. 2007)

gle increased with cavitation intensity. The focus of the studies on flow regimes under cavitating conditions was on how the frequency of cavitation shedding varied in internal nozzles [49] as well as images of periodic cavitation shedding [50]. De Giorgi et al. [11] studied flow regimes using a CCD camera and presented an analysis based on pressure fluctuation frequency. Their experimental observations illustrated different flow regimes (from inception to cavitating jets) under various working conditions. They also compared the frequency obtained from pressure fluctuations with visual observation spectra and captured a dramatic augmentation in the first peak of the frequency spectra, while the flow regime changed to jet cavitation. Cloud cavitation is regarded as a significant form of cavitation instability and is formed when a considerable value of cavitation bubbles periodically merge and form a cloud. This type of cavitation instability was observed in several domains such as hydrofoil, orifice and venturi [11]. Stanley et al. [51] experimentally focused on the periodic shedding of cavitation in macro cylindrical nozzles and examined the existing re-entrant mechanism. Their results obtained from the visualization of cavity and re-entrant jets revealed that cavity cloud was detached from the wall by a liquid layer sub. Visualization of cavitation phenomenon inside nozzles and its effect on spray characteristics [10, 16] along with flow structure were recently studied in the literature using different measurements techniques such as qualitative description, pressure point and velocity measurement [52].

Payri et al. [53] visualized internal flow regimes for four different fuels inside a

nozzle installed into a pressurized rig test and visualized cavitation bubbles with the aid of differences in refractive indices between vapor and liquid. They demonstrated that cavitation bubbles were generated prior the mass flow collapse condition. Moreover, they observed that the fully developed cavitation condition lead to mass flow collapse depending upon the upstream and downstream pressure and fuel viscosity.

Kravtsova et al. [54] used the PIV (Particle-Imaging Velocimetry) technique and high-speed images visualization in order to observe and analyze cavitating flows around semi-circular leading edge plates and NACA0015 hydrofoils with different angles at various Cavitation numbers. For small attack angles, the flow patterns observed in these geometries were dependent on attack angles. Streak array was visualized as the initial cavitation occurrence for the plate and traveling bubbles for the hydrofoil. Increasing the attack angle of the hydrofoil lead to a change in the cavitation regime type around the hydrofoil (to the steak array) similar to the plate at lower angles. Gavaises et al. [42] observed the formation of cavitation cloud in axial symmetric geometries and showed that the cavitation cloud developed in the radial direction until the collapse, which was deduced from the vortex shedding analysis. The collapse frequency decreased with Reynolds number due to high density of the vortex cavities. Naoe et al. [55] studied the behavior of cavitation bubbles in mercury by visualizing the growth and collapse of generated bubbles in the vicinity of the solid structures. The bubble collapses enforced the acoustic emission. They also observed annulated mist expansion as a result of the shock wave propagation. Perpar et al. [12] experimentally visualized cavitation bubbles inside slot orifices and cavitation inception. They conducted two distinct experiments in order to study a single cavitation bubble and huge amount of bubbles at atmospheric and saturation pressures, respectively. They classified flow regimes in the slot region into single bubble and macroscopic bubble cluster, bubble cloud and collapsing bubbles regimes under different working conditions.

Recent studies [56, 57] relevant to the investigation of bubbly cavitation in micro scale presented eroded surfaces due to the destructive energy of the collapse of cavitation bubbles. The domination of surface cavitation in micro domains due to augmented surface tension effects was exploited using micro patterns with hydrophobic and hydrophilic strips in order to control cavitation bubbles [58]. Belova-Magri

et al. [58] visualized emerging cavitation bubbles from thin micro-patterned surfaces with a high speed imaging. It was observed that the intensity of cavitation in micro scale is highly dependent upon the surface energy and the size of the strips.

Spray formation downstream of micro flow restrictive elements strongly depends on the flow regimes inside them. Although it is possible to simulate the sprays details including primary and secondary break-ups, spray and break-up visualization are vital and challenging in micro scale studies, where the dimensions are very small, and the process occurs within a very short period of time. Recently, high velocity jets along the spray, bubble evolution, collapse of the bubbles, and droplet segmentation in the spray have become popular due to their exploitation in engineering and biomedical applications. It is crucial to identify the appearance of the spray and to concentrate on the whole shape of the spray in such a way that the spray length and energy released from the collapse of resulting bubbles could be applied on a possible target at the optimum distance for such applications. For this, rigorous studies are necessary to assess flow characteristics downstream of the micro flow restrictive elements, and experimental investigations are required to gain insight into cavitating flow physics with visualization as well as with numerical approaches.

Fluids utilized in turbomachinery are prone to cavitation, where bubbles with different sizes are generated depending on fluid flow characteristics [2, 59, 60]. The nature of such bubbles is strongly dependent on the ambient and discharge pressures [61]. Studies in the literature proved that hydrodynamic cavitation in turbomachinery is detrimental for the system and badly affects the performance of the device [3, 62, 63]. Cavitation phenomenon was also observed in micro scale, and it was reported that micro scale cavitation significantly differs from conventional scale [16].

Spray formation was studied both numerically and experimentally in conventional orifices within a wide range of operating conditions [27, 28, 64]. Most of these studies focused on the applications of nozzles and flows at the outlet of nozzles in automotive industries [65]. Although some of the studies included experiments on mini/micro-nozzles [66, 67], there is still a considerable lack of information about spray characteristics in micro scale and exploitation of potential applications such as biomedical treatment with cavitation erosion. Im et al. [68] took X-radiography

measurements to investigate the influence of the internal geometry of a nozzle on the morphology of a high speed liquid jet immediately downstream of the nozzle. They found that cavitation inside the nozzle is strongly affected by internal geometry variations in micro scale. There are also some investigations focusing on the effect of the sprays on small targeted areas [17–20]. Liao et al. [69] used the VOF (Volume of Fluid) model to simulate the collapse process in order to determine the optimum stand-off between the targeted point and probe. They showed that this model was capable of measuring the jet velocity and pressure impulse. Moreover, they illustrated that the main mechanism in the cavitation erosion concept is high pressure instead of the jet velocity.

While major properties of the spray and significant locations along the spray were mainly investigated from a numerical point of view [70, 71], spray visualization displaying the spray morphology has not been considered. Balewski et al. [72] experimentally studied nozzle flows and resulting spray formation without the effect of the cross-flow velocity and turbulence in a pressure atomizer. They used a Phase Doppler System (PDS) to measure droplet sizes in the spray and the velocity distribution. Hossainpour et al. [73] simulated the spray process in a diesel injection engine and considered various break-up models to study their effect on the variation of spray characteristics.

2.3 Lithotripsy and Cavitation in Urinary Stone Therapy

The propagation of an acoustic wave with the frequency from few tenths of kHz to several hundreds of MHz refers to the term "ultrasound". In liquids, the propagation of longitudinal waves causes local oscillatory motions of particles around their initial positions, resulting in local changes in liquid pressure. Depending on the frequency, the level of acoustical energy and/or pressure can be targeted to the desired area, thereby enabling the use of ultrasound in therapeutic applications. Because of its ability to exert localized energy from surface of the skin into soft tissues, ultrasound has attracted much interest as a non-invasive and targeted therapeutic treatment [74].

Even though biomedical uses of cavitation phenomena are rapidly increasing, a recent comprehensive review on its physical and/or biological effects and clinical applications in biomedical sciences is missing in the literature. Here, we focus on recent studies and advances in the use of ultrasound and hydrodynamic cavitation in biomedical treatment. Physical properties and currently available applications are reviewed, and exponentially growing new approaches are discussed. Improved understanding of this field is of vital importance and would open a new area for the development of novel therapeutic techniques.

2.3.1 Urinary Stone Therapy Using Lithotripsy and Ultrasound Cavitation

Ultrasound cavitation became an important method in disease therapy because it offers non-invasive and extracorporeal treatment possibilities. In low-intensity pulsed ultrasound (LIPUS), a major method, mechanical energy is transcutaneously transmitted as high-frequency acoustical pressure waves into biological tissues [75]. Today, this medical technology is an established, widely applied intervention for enhancing bone healing in fractures and non-unions [76, 77]. Sonoporation is a well-established ultrasound-based phenomenon for drug delivery, which increases gene uptake into tumor cells. Collapsing bubbles are believed to change the permeability of cell plasma membrane by creating transient holes, allowing efficient delivery. Although ultrasound cavitation has various applications in biomedical sciences, majority of the articles published in this field is concentrated on its biomedical effects in urinary stone treatment. Non-focused ultrasound might result in hyperthermia in targeted areas and might lead to side-effects, such as nerve and vasculature damage in surrounding normal tissues. The usage of high-intensity focused ultrasound (HIFU) or histotripsy methods overcomes these limitations to a certain extent, leading to precise tissue destruction by ultrasound cavitation and utilization in thermal ablation of tumors. Another ultrasound-based non-invasive method is shock wave lithotripsy (SWL), which offers important advantages for the treatment of renal and ureteral stones. The targeted surfaces are successfully destroyed with shock waves with slow rate resulting to reduced renal injury [78]. Recent studies also demonstrated successful therapeutic applications of SWL in orthopedic problems and heart

diseases. In this section, recent studies and advances in SWL and lithotripsy will be presented.

2.3.2 Shock Wave Lithotripsy (SWL)

It is well-known that the shock wave lithotripsy provides effective biomedical treatment particularly for kidney stone fragmentation. Its effects are based on two fundamental mechanisms, shock wave-related effects and cavitation phenomenon. Mechanical stresses generated by shock wave lithotripsy (SWL) lead to stone fragmentation [79]. Many researchers proposed new methods to enhance the effectiveness of SWL by intensifying shock waves. Sass et al. [80] used kidney stones and gallstones, which were exposed to shock waves, and reported a two-step process in resulting erosion. They showed that first slits formed as a result of the interaction between shock wave and targets and then the liquid filled small cracks at the first step. Secondly, the collapse with cavitation caused significant erosion on the surface of stones, and finally, fragmentation took place. Holmer et al. [81] also showed that acoustic cavitation and streaming significantly contributed to the disintegration of stones.

Extracorporeal shock wave lithotripsy (ESWL) is a kind of the shock wave lithotripsy method, in which the source of the shock waves is outside the body and the shock profile of the ESWL impulse can be determined using a lithotripter device. The main structure of an ESW lithotripter device includes a shock wave generator, a focusing device and a system used for locating the stone. There are three significant sources in ESWL, namely electrohydraulic, electromagnetic, and piezoelectric sources. The generation of ultrasound cavitation and collapse of the bubbles are of great importance to treat the urinary stones with ESWL. Although effectiveness and safety of this method in urinary treatments were proven by many investigations [82], investigators have shown that the modern lithotripters were highly ineffective compared to the original devices and might cause severe injury [83].

While, ESWL typically works best with stones between 0.4 *cm* and 2 *cm* in diameter, which are located in the kidney, Wu et al. [84] in a study on the treatment of the renal stones with a size of 20 *mm* or bigger on 376 patients reported 64.4 % overall stone-free rate and 70.7 % efficiency rate after 3 months. They claimed

that ESWL is the first choice for the stone with a surface area of 400 mm^2 and for the bigger ones, successive treatments are required. On the other hand, ESWL has a lower rate of success, when stones are located in the ureter. In regards to the guidelines on urolithiasis of the European Association of Urology, ESWL is implementable in minimally invasive endoscopic modalities to treat stones of the upper urinary tract in humans [85]. Success rate of this method could be increased by using a ureteral stent, which allows for easier passage of the stone by relieving obstruction and through passive dilatation of the ureter. In fact, the results of this method are also dependent on many factors such as shock wave rate, probe to sample distance and pressure profile. Howle et al. [86] studied shock waves in the kidney stone treatment under the framework of lithotripsy and presented an expression for profile of the ESWL impulse:

$$p(t) = \begin{cases} 2p_{max} \exp^{-t/\varphi_1} \cos\left(\frac{t}{\varphi_2} + \frac{\pi}{3}\right) & \text{if } 0 < t < \frac{7\pi}{6}\varphi_2 \\ 0 & \text{otherwise} \end{cases} \quad (2.1)$$

where φ_1 and φ_2 determine the profile of the extracorporeal SWL impulse.

The repeated use of SWL in the same patient has been shown to be correlated with an increase in the amount of phosphate in the kidney stone [87]. This is a huge issue in light of the large increase in the number of patients with phosphate stones. There are some studies showing a correlation between SWL number and phosphate content of the resulting kidney stone. Williams et al. [88] attempted to correlate the stone fragmentation rate with the structure of the internal stone using Brushite stones imposed to SWL. However, their proposed tomography technology did not anticipate any correlation between brushite stones break and SWL. Pramanik et al. [89] used the ground stone powder and utilized a three-step extraction method to predict the protein content in the kidney stone. They showed that brushite and apatite stones contain higher amount of protein in comparison to the previous studies. In this regard, Kacker et al. [90] investigated the effect of the calcium phosphate stone on the stone-free rate and found that the higher rate of phosphate contains in the renal stone results in the reduction of the stone-free rate. Moreover, Evan et al. [91] performed an experiment in pigs showing a rise in urinary pH as a long term effect of SWL on kidney function as well as changes in renal morphology

and tubular changes consistent with a dysfunctioning thick ascending thick limb. Some important preliminary studies in SWL are presented in Table 2.1.

Table 2.1: Preliminary Significant Reports in SWL

Study	Strategy	Major Findings	References
Gallstones in humans exposed to shockwave lithotripsy	An alternative method of gallstone clearance in adults	Using cholecystectomy impacts on biliary physiology as an alternative conservative treatment for cholesterol gallstones	Sauerbruch et al. [79]
Exposure of kidney stones and gallstones to shock waves	Visualization of the destruction on the targeted surface	Collapse of the cavitation bubbles as the most significant mechanism in the erosion-Two-step process in resulting erosion	Sass et al. [80]
Kidney stone exposure to SWL	Surrounded target to determine the destruction rate	Mechanical effects including acoustic cavitation and streaming effect on stone fragmentation	Holmer et al. [81]
Urinary stones treatment using extracorporeal shock wave lithotripsy	Using focused shock waves to fracture calculi instead of surgery (First report)	Reducing the need for surgery with the aid of shock wave lithotripsy	Chaussy et al. [82]
Immediate focus on the renal morphology after extracorporeal shock wave lithotripsy	Using renography assess renal function in patients after shock wave lithotripsy	Significant acute renal trauma as a result of shock wave lithotripsy impose	Kaude et al. [85]

2.3.3 Secondary and Tandem Shock Waves in SWL

Secondary shock waves are of great importance in treatment of urinary stones. The implementation of tandem shock waves and the time of sending the second shock wave play a crucial role in SWL. In order to intensify the collapse of the cavitation bubbles, which were produced as a result of the tensile phase of the shock waves, a second shock wave is sent within some hundred micro-seconds after the first wave. Cavitation bubbles are nucleated in the presence of the tensile part of the waves, and bubble collapse near the stone generates secondary shock wave leading to erosion [92]. Later on, Delacretaz et al. [93] emphasized that in addition to the ordinary stresses on the stone target, there are always second shock waves induced by cavitation collapse, which are more destructive than the initial stresses during SWL. Sheir et al. [94] investigated twin-pulse (TP) treatment in eliminating the kidney stone. They conducted the first prospective clinical study with the twin-pulse lithotripter on 50 patients, whose renal stones had the diameters less than 2 cm. The capability of the tandem shock wave was investigated in other studies in the literature [95, 96]. Loske et al. [97] evaluated the capability of the dual-pulse SWL (tandem shock

wave) in controlling and collapsing the cavitation bubbles, which were induced by second shock waves. They found that this method was efficient in intensifying bubble implosion. The comminution of stones was increased without any tissue damage in *In vitro* studies. Loske et al. [98] tried to enhance cavitation damage on kidney stone during extracorporeal SWL by generating shock waves with time delays of 50 to 950 μs in their earlier studies. The fragmentation ratio was increased at 250 and 400 μs shock wave delays. Alvarez et al. [99] used a modified piezoelectric shock wave generator to produce single-pulse and dual-pulse shock waves and studied the effect of shock waves on the viability of bacteria in solutions. They claimed that tandem shock wave could inactivate the bacteria, while low-pressure single-pulse did not have any significant effect on the bacteria. They also found that tandem shock wave could control bubble growth and prevent their collapse by sending the second shock wave beforehand. Furthermore, tandem shock wave could be used to shorten the SWL process.

The conclusion of the enhancement with strong micro-jets, which the second shock wave delivers for tenths of micro-seconds prior to collapsing the bubbles, was reported in the literature [100, 101]. Fernandez et al. [102] conducted an *In vitro* study to reduce the SWL time using tandem shock waves. They did their experiments with and without fluid-filled expansion chambers and observed few variations in stone comminution for both single and tandem shock waves in the presence of the fluid field. However, they recorded a significant decrease in SWL time for tandem shock waves.

Recent studies confirm the strong effect of the focused shock wave lithotripsy on the cancer treatment. Lukes et al. [103] developed a focused tandem shockwave lithotripsy (FTSW) generator in order to provide two successive waves with a time delay of 10 μs . The waves generated in this study were at peak positive and tensile pressures of 80 and -80 *MPa* for first and tandem ones, respectively, while the time delay was adjusted with parabolic reflector and the electrode structure. They reported a remarkable enhancement of the antitumor effect of chemotherapeutic drugs due to generation and collapse of cavitation bubbles during FTSW process. Tandem shock waves boost attention in pharmaceutical industry recently. Loske et al. [104] used tandem shock wave (underwater) in order to transfer filamentous fungi

used in generating antibiotics and proteins. They showed a significant superiority of tandem shock wave with a delay of $300 \mu\text{s}$ in genetic transformation of filamentous fungi compared to standard shock wave. Numerical modeling on the secondary shock wave was also taken into account, and stress and cavitation effects were determined as the key parameters in the fragmentation of the targeted surfaces during tandem shock waves [105]. Some important investigations on the tandem shock wave are presented in Table 2.2.

Table 2.2: Summary of Tandem Shock Wave Studies

Strategy	Tandem shock wave significance	Methodology	Outcome	Reference
Comparison between secondary and ordinary waves	Secondary shock wave's superiority compared to ordinary waves	Characterisation of cavitation erosion using collapse process to produce secondary shock wave	Critical impact of cavitation on the ESWL	Delacretaz et al. [93]
Controlling and collapsing the cavitation bubbles induced by TP	Efficiency of TP in intensifying the bubble implosion	Applied successive shockwaves (tandem) to the targets using modified piezoelectric lithotripter	No reported tissue damage <i>In vitro</i> study during comminution increase	Loske et al. [97]
Treatment time reduction during ESWL by enhancing fragmentation of the kidney stone	Cavitation damage enhancement on kidney stone	Piezoelectrically Generating shock waves with time delays of 50 to 950 μ s	Increase in fragmentation ratio for 250 and 400 μ s shock wave delays	Loske et al. [98]
Investigation on the raise of micro-organism death via tandem shock wave generation	Focus on the effect of shock waves on the livability of bacteria in solution	Utilizing piezoelectric shock wave generator to produce single-pulse and dual-pulse shock waves	Tandem shock wave capability in activating bacteria	Alvarez et al. [99]
Decreasing the SWL process duration using tandem shock wave via animal model	Significant decrease in SWL time for tandem shock waves	Use of fluid-filled expansion chamber to study the stone fragmentation Standard for single-pulse and tandem shockwaves	Variations in stone comminution for both single and tandem shock waves	Fernandez et al. [102]
Application of focused tandem shock waves in cancer treatment	Delay in tumor growth with the aid of tandem shock wave	Using parabolic reflector (cathode) to produce diverging cylindrical pressure wave at a specific point (focused)	Strong interaction between first and second waves at time delay of 8-15 μ s	Lukes et al. [103]
Improvement of DNA transformation to fungal cells using tandem shock waves	<i>Aspergillus niger</i> ransformation improvement with tandem shock wave compared to standard one	Using underwater shock waves to transfer filamentous fungi genetically	Genetic transformation of filamentous fungi is significantly affected by acoustic cavitation μ s	Loske et al. [104]

2.3.4 Cavitation Effects on SWL

Cavitation phenomenon and bubble collapse were considered as important parameters in SWL [106]. The aim of the studies on this field was to increase the comminution of stones while reducing the tissue injury. Williams et al. [107] observed that gas bubbles existing in the air-fluid interfaces had the potential for serving as cavitation nuclei and found that even small bubbles had an important impact on the lysis of red blood cells during the shock wave exposure.

The cavitation phenomenon is in a close association with SWL in the processes of formation and collapse of cavitation bubbles. While the acoustic aspect of the lithotripsy induces the cavitation bubbles, cavitation bubbles and clouds dramatically influence the lithotripsy treatment and the pressure distribution in the focal region of the SWL. The collapse of the cavitation bubbles, distance between the applied laser and the targeted stone, the topology of the targeted stone sample are the most significant parameters, which were considered in the literature to control the cavitation phenomenon. Ikeda et al. [108] investigated cavitation cloud and its effect on the pressure field. They discovered that the control of cavitation collapse had a big potential in lithotripsy treatment. They suggested that since the cavitation cloud was the most destructive feature, it had the capability to concentrate intensive pressure fields in the case of acoustically induced collapse of the bubbles (Fig. 2.3). It was extensively reported in the literature that the collapse due to cloud cavitation might generate local pressures having a more dominant effect than initial waves.

Yoshizawa et al. [109] investigated the effect of the cloud cavitation on high intensity focused ultrasound (HIFU). The energy released from the cavitation bubble collapse induced by acoustic field has the capability of focusing very high pressures. Their method, which included two steps, namely, high frequency ultrasound (1 to 5 *MHz*) and then low frequency ultrasound (100 *kHz* to 1 *MHz*) with short pulses, offered localization of cavitating bubbles on the stone. Both of the frequencies were applied to the stone surface. However, the second one induced cavitation cloud collapse by generating an oscillating field in the cavitation bubbles and led to powerful shock waves interior the cloud. Thus, the bubbles in the vicinity of the center of the cloud collapsed, and a high pressure field was generated, which resulted

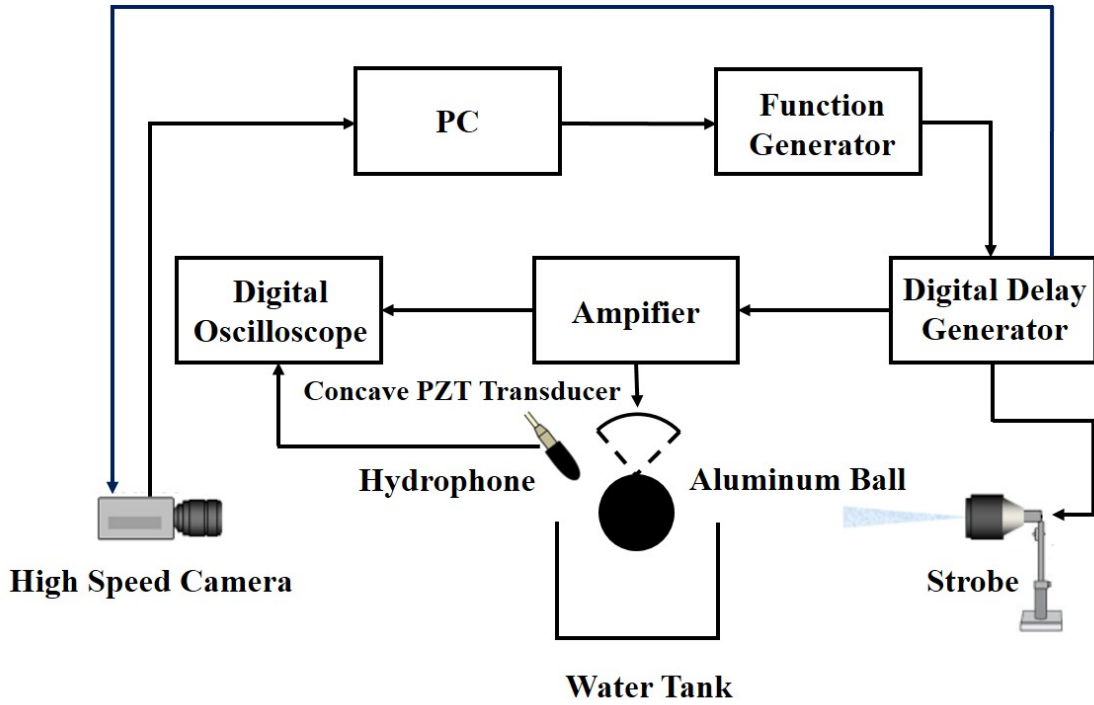


Figure 2.3: Schematic of the Experimental Set-up (Ikeda et al. 2006). The Set-up Consists of an Acrylic water Tank, an Ultrasound Generation Unit and a Data Acquisition Unit

in fragmentation of the stone.

The collapse of the shock-induced cavitation bubbles and their contributions to SWL were extensively reported [110]. Johnsen et al. [111] found that shock-induced collapse of air bubbles had a considerable effect on damaging the stone in SWL. Their numerical results were in a good agreement with experimental observations. They showed that bubble collapse near the rigid wall raised the wall pressure (wall pressure determines the damaging power of cavitation bubble collapse), and affected the stand-off distances in kidney stone erosion. Ultrasound cavitation effects are enhanced with delayed second shock waves. Therefore, the importance of intensifying the effect of cavitation collapse is of great interest in this field. Pishchalnikov et al. [112] considered cavitation control as an important mechanism in the SWL. The formation of single bubbles resulted in clusters in proximal locations and sides of the stones, and the collapse of each cluster led to erosion and also helped the crack growth.

Another significant issue in the relation between cavitation phenomenon and

SWL is the distance between the probe and the targeted area. Fuh et al. [113] studied the effect of the distance of laser fiber to stone on the ultrasound cavitation. They studied the effect of the laser fiber proximity on the fragmentation of the stone and examined the distance between the laser fiber and stone target in order to study cavitation bubble behavior. The diameter of cavitation bubbles was increased at larger distances between the stone and fiber. The effect of the collapse of reflected bubbles on rigid bodies was investigated by Calvisi et al. [114]. They developed a boundary integral method to study the effect of non-spherical collapse of bubbles influenced by SWL on the near rigid body. They found that the bubble-wall distance had a dramatic effect on dynamics of bubbles collapse in the case of reflection. The results were independent of initial radius of the bubbles. Selected studies on the effect of the cavitation on SWL are gathered in Table 2.3.

Table 2.3: Cavitation Contribution in SWL

Strategy	Outcome	Cavitation Contribution	Reference
Cavitation observation in the interface	Even small bubbles affect the lysis of red blood cells	Gas bubbles	Williams et al. [153] [107]
Degassed water and castor oil usage in disintegration of renal calculi in SWL	89% and 22% Fragmentations in kidney stones after 200 shocks in degassed water and castor oil, respectively	Ultrasound cavitation	Zhu et al. [137] [106]
Cavitation collapse control in lithotripsy treatment	The capability of cavitation cloud to concentrate intensive pressure fields. Crack growth in the case of cluster collapse	Cavitation cloud and cluster collapse	Pishchalnikov et al. [112]
Effect of focusing on shock-induce collapse of air bubbles on stone damage	Wall pressure increase and variation in stand-off distances in presence of near wall collapse	Collapse of air bubbles	Johnsen et al. [111]
Cloud cavitation effect on high intensity focused ultrasound (HIFU)	Very high pressures concentration due to energy released from cavitation collapse	Cloud cavitation and collapse	Yoshizawa et al. [109]

2.4 An Alternative for Ultrasound Cavitation; Hydrodynamic Cavitation

While hydrodynamic cavitation has been extensively studied in applications involving hydromachinery, potential biomedical applications were recently considered as an emerging research area particularly in micro scale. Although ultrasound cavitation is very popular in disease therapeutics, side effects caused by ultrasound cavitation motivated researchers to seek for different, local and efficient methods, such as hydrodynamic cavitation (Table 2.5). In a very early study, Rooney [115,116]

found that hydrodynamic cavitation had the capability of generating high intensity jet flows, which could be used in order to fragment stone and damage the tissues. Then, Palanker et al. [117] used a two-dimensional Rayleigh-type hydrodynamic simulation in order to study the interaction between a jet containing bubbles and a soft tissue made of chorioallantoic membrane (CAM). They tried to avoid generating cavitation bubbles, which might cause considerable damage to tissues using concave endoprobes. Their results were obtained under the condition of a maximum velocity of 80 m/s and tissue distance up to 1.4 mm . They indicated that concave endoprobes could be used to prevent tissue damage by slowing down the bubble back boundary diffusion. Toytman et al. [118] investigated hydrodynamic interactions among simultaneous cavitation bubbles originating from multiple laser foci, which are widely used in ophthalmologic surgery. If multiple cavitation bubbles were produced at once, with a target tissue trapped between them, cutting efficiency was enhanced. Focusing problem by a series of pulses could be solved.

Different from previous studies, experimental setup that was used in the study of Koşar et al. [17] did not include any moving part, and their experiments were carried out at various inlet pressures while visualizing bubbly cavitating flow patterns (Figure 2.4). The authors studied the impact of released bubbles on kidney chalk specimens and two different leukemia cells. On chalk specimens, they observed that the penetration in the chalk medium increased with time. The distance between the micro-probe and the specimen was an important parameter. The penetration depth was larger for closer distances due to stronger bubble specimen surface interactions. The interaction between emerging bubbles (from the micro-probe) and the chalk surface caused significant erosion and created rough local spots on the surface leading to augmented roughness on chalk surfaces. The findings implied that the erosion resulting from the exposure to bubbly cavitation was produced by micrometer-size bubbles rather than the shear effect of the liquid flow. Moreover, the authors measured the size of the eroded stone debris and maximum debris size was found to be $50\text{ }\mu\text{m}$. On the other hand, the data of Koşar et al. [17] with leukemia cells showed that after bubbly cavitation exposure cancer cells died as a result of two different mechanisms: First effect was seen shortly after exposure, in which most of the cells lost their membrane integrity, Second effect was the late effect on cell

survival. Although the short-term effects of cavitation caused a form of cell injury following with premature cell death due to the mechanical forces of cavitation, the late effects might be controlled by a programmed cell death mechanism.

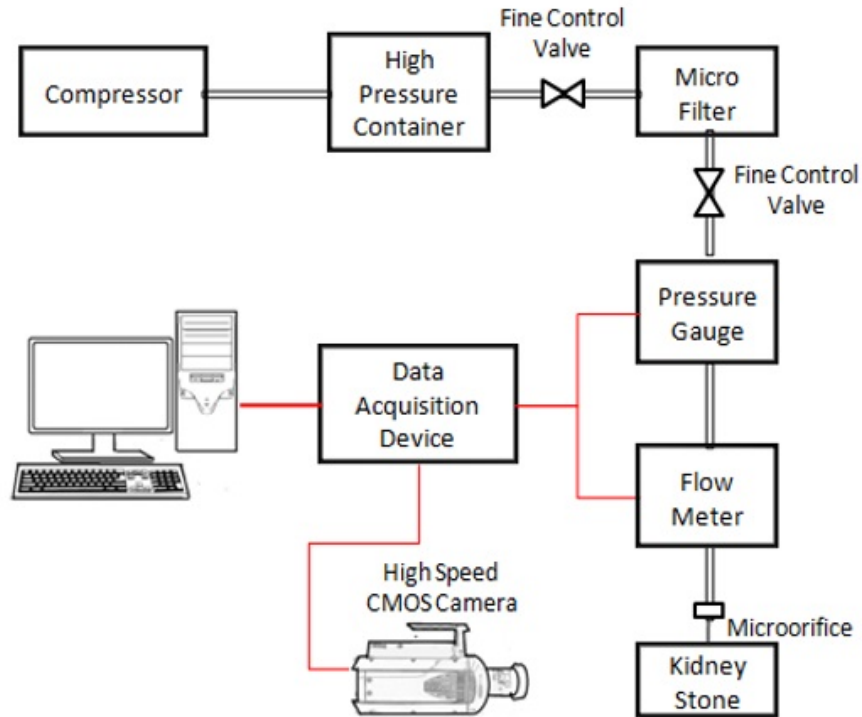


Figure 2.4: The Hydrodynamic Setup used to Fragment Kidney Stones (Perk et al. 2012)

As an extended study, Perk et al. [18] assessed the capability and applicability of hydrodynamic cavitation method for kidney stone treatment utilizing 18 kidney stone samples made of calcium oxalate. The authors used phosphate buffered saline (PBS) solution as the working fluid. At a cavitation number of 0.017 and a probe to specimen distance of 1 *mm*, their experiments resulted in an erosion rate of 0.31 *mg/min*. By using a similar experimental design in the study of Itah et al. [19], the authors investigated the destructive effects of hydrodynamic cavitation on prostate cancer cells and benign prostatic hyperplasia (BPH) tissues as well [19]. Here, the detailed molecular mechanisms hydrodynamic cavitation effect were also analyzed using prostate cancer cells. The micro-orifice was a polyether ether ketone (PEEK) with an inner diameter of 147 μm , while the pressure at the inlet was varied from 50 to 150 *psi* for cell culture experiments, and the physiological solution was phos-

phate buffered saline (PBS). The results on prostate cancer cells PC-3 and DU-145 exposed to hydrodynamic cavitation showed the destructive effect of bubbly cavitation in a pressure- and time-dependent manner. There was a further increase in dead cells after 24 *h* since the cavitation exposure. There was no evidence of the activation of apoptotic programmed cell death, shown by the analysis of nuclear changes, caspase activation, PARP cleavage, sub-G1 fraction cells and DNA laddering. Additionally, activation of other type of programmed cell death, autophagy, was also not observed. These results indicated that hydrodynamic cavitation damaged prostate cancer cells instantly and pulverized cells upon exposure. Moreover, the authors proved significant damage and penetrating effect of hydrodynamic cavitation to exposed BPH tissue specimen compared to the non-cavitating conditions, which suggests that hydrodynamic cavitation could be a viable alternative in BPH tissue treatment.

Similar experimental set up was used to show the effect of hydrodynamic cavitation on protein structure [20]. In this study, the authors had chosen Hen egg-white lysozyme as a protein model. Via biochemical and biophysical methods, they found that hydrodynamic cavitation had no significant effect on lysozyme structure and function. The authors revealed a reversible change of hydrodynamic diameter and bioactivity outside the cavitation regime. Their results suggested that side effects of the application due to local protein damage is expected to be minimal. Studies on hydrodynamic cavitation in biomedical treatment are summarized in Table 2.4.

2.5 Side Effects and Limitations in Biomedical Use of Ultrasound and Hydrodynamic Cavitation

Ultrasound cavitation treatment of cells or tissues was reported to have several side effects in various systems. At a cellular level, cell death either resulting in instant cell lysis or in the induction of programmed cell death is the main outcome of ultrasonic cavitation treatment. Cell membrane disruption following by induction of apoptotic cell death was detected after administration of low intensity ultrasound cavitation in

Table 2.4: Summary Of Studies on Hydrodynamic Cavitation in Biomedical Applications

Method	Target	Effect	Reference
Rayleigh-type hydrodynamic simulation of interaction between bubbles and tissue	Soft tissue made of chorioallantoic membrane (CAM)	Prevention of tissue damage using concave endoprobes	Palanker et al. [117]
Bubbly cavitating flow effect on cell cultures	Kidney chalk specimens and cancerous cells	Significant reduction in cell livability	Kosar et al. [17]
Hydrodynamic cavitation exposure on target area	Kidney stone samples	Considerable erosion rate in an optimum probe-specimen distance	Perk et al. [18]
Hydrodynamic cavitation exposure on target area	Prostate cells and benign prostatic hyperplasia (BPH) tissue	Hydrodynamic cavitation as an alternative to ultrasound cavitation in treatments involving BPH tissues	Itah et al. [19]
Hydrodynamic cavitation exposure on target area	Lysozyme structure	No irreversible effect No deactivation	Turkoz et al. [20]

leukemic cells [119]. Similarly, *In vitro* application of high frequency ultrasound has also been shown to lead to irreversible cellular damage via apoptotic programmed cell death. Activation of programmed cell death mechanism by ultrasonic cavitation was revealed in various human and murine cancer cells.

In addition to cellular damage, the cavitation phenomenon induced by shock waves caused serious injuries in organs of the body. Brujan [120] reviewed the effects of cavitation bubbles in the cardiovascular application of ultrasound and laser surgery as well as the effects of cavitation in mechanical heart valves. He indicated that the interaction between cavitation bubbles and tissue during pulsed laser surgery caused damage to surrounding tissues. The author also emphasized on the effects of bubbles collapse resulting in the generation of shock waves, high-velocity liquid jets, free radical species, and strong shear forces, which might damage the nearby tissues during cardiovascular application of ultrasonic cavitation.

Although the most commonly used technique, SWL, has a good success rate for kidney stone treatment in adults [121], there are many studies reporting the side effects of SWL. Its destructive effects result in intensification of stone malady due to several shock wave lithotripsies, tissue injury, nephron and blood vessel injury [122,

123].

Recker et al. [124] investigated vulnerable parts of the body exposed to the effects of shock waves and found that critical intra-renal hematomas were one of the most serious harmful outcomes. Shock waves indirectly stimulated the sciatic nerves, and its consequences were studied by Schelling et al. [125]. They found that cavitation caused significant pain during extracorporeal SWL. Induced shear stress and hydrostatic tension were considered as factors affecting kidney injury in pre-focal region. Al-Awadi et al. [126] studied the effect of the antioxidation on renal injury. They performed a clinical study to determine how antioxidants could decrease short-term damage of SWL treatment. Their experiments focused on three groups of patients: patients not taking any antioxidants (control group) and the other two groups taking different amounts of antioxidants capsules, "Nature Made R". Blood and urine samples were gathered during various periods before and after extracorporeal SWL. The serum albumin amount measured in the group taking antioxidants was higher in comparison to the control group. Their results proved that free radicals were produced during treatment, and antioxidants reduced renal injury in blood generated after extracorporeal SWL administration. Aksoy et al. [127] focused on the effect of SWL on plasma and malondialdehyde (MDA) concentrations and found that this method led to disruption in the renal capillary, which led to renal ischemia-reperfusion (I/R) injury. They also claimed that erythrocyte glucose-6-phosphate dehydrogenase and its catalytic function were considerab. Benyi et al. [128] proposed a method, in which a randomized investigation was applied to several patients, and a calcium antagonist (nifedipine) and also a xanthine oxidase inhibitor (allopurinol) were examined on high energy renal function. They tried to reduce renal damage induced by SWL and found that calcium antagonist could affect the urine rate of albumin in patients exposed to SWL.

Table 2.5: Summary of Studies in Relation with SWL Side Effects

Observation	Side Effects Considered	Reference
<i>In vitro</i> experiments	Hypertension inception	Barbosa et al. [129]
Renal function observation under SWL	Tissue injury	Connors et al. [122]
<i>In vitro</i> functional outcome of extracorporeal SWL	Hematoma formation	Fainas et al. [130]
Renal calculi observation under SWL	Scar formation	Morris et al. [131]
Renal and proximal ureteral stones under SWL	Diabetes	Krambeck et al. [132]
<i>In vitro</i> observation of renal calculi under SWL	Nephron and blood vessel injury	McAteer et al. [123]
<i>In vitro</i> experiments Vulnerable organs observation under SWL Sciatic nerves exposure to SWL	Vascular defects Intrarenal hematomas Sciatic nerves	Shao et al. [133] Recker et al. [124] Schelling et al. [125]
Pre-focal region observation in SWL	Hydrostatic tension and shear stress	Sturtevant et al. [134]
Plasma and malondialdehyde (MDA) concentrations observation under SWL	Renal ischemia-reperfusion (I/R) injury.	Aksoy et al. [127]

Despite the increasing potential of hydrodynamic cavitation, its clinical application has also some limitations. *In vivo* applications might only be possible through the integration of a cavitation tube system into an endoscopy device. This system may require a flow tube in order to generate negative pressure, and the treatment could only be performed in tissues, where the tip of the device can be positioned. Precise manipulation of the endoscopic probe in the body is another critical point. The endoscopy device should allow the application of hydrodynamic cavitation in a localized and targeted manner. Table 2.5 summarizes SWL Side Effects reported in the literature, while important mechanisms of stone fragmentation in SWL are gathered in Table 2.6.

Table 2.6: Mechanisms of Stone Fragmentation in SWL

Mechanism	Advantage and Disadvantage	Implementation	Reference
Tear and shear forces	Restricted to small area target observation	Occurrence of pressure drop and front and distal surface pressure variation	Chaussy [135]
Quasi-static Squeezing	Restricted to large area target observation	Occurrence of pressure gradient in squeezing of the stone	Eisenmenger [136]
Dynamic Squeezing	High accuracy in numerical simulation analysis	Squeezing waves effect on the shear waves generated at the stone corner	Sapozhnikov et al. [137]
Cavitation	Privilege in stone fragmentation and shock wave exposure	Pressure drop occurrence in low static pressure and negative pressure wave generation	Crum [92]
Spallation	Restricted to small area target observation	High tension level generation at distal surface of the stone	Zhong et al. [101]

Chapter 3

Numerical Simulations of Cavitating Flow Inside Micro and Mini-Channels

3.1 Introduction

In this chapter, cavitation phenomenon inside micro and mini-channel configurations are numerically investigated. The simulations for each channel are performed at different upstream pressures varying from 10 to 150 *bar*. Two micro-channel configurations with inner diameters of 152 and 254 μm and two mini-channel configurations with inner diameters of 504 and 762 μm are simulated. In order to validate the numerical approach, micro-jet impingement from a micro-channel with an inner diameter of 152 μm is first simulated at different Reynolds numbers. Then, the mixture model is used to model the multiphase flow inside the channels. The results of this study present major differences in cavitating flows between the micro and mini scale channels and show that the pressure profile and vapor phase distribution exhibit different features. The static pressure drops down to negative values (tensile stress) in micro-channels while the minimum static pressure in mini-channels is found to be equal to vapor saturation pressure, and higher velocity magnitudes especially at the outlet are visible in the micro-channels. It is shown that for higher upstream pressures, the cavitating flow extends over the length of the micro/mini-channel thereby increasing the possibility of collapse at the outlet. The effect of en-

ergy associated with turbulence was investigated at high Reynolds numbers for both micro/mini-channels and its impact was analyzed using wall shear stress, turbulence kinetic energy and mean velocity in various location of the micro/mini-channels. In addition, the effects of bubble number density on two-phase flow hydrodynamics were studied using the numerical approach, where transient model was utilized to obtain the changes in vapor quality inside the micro-channel and velocity field near the inlet and outlet of the nozzle.

3.2 Numerical Modelling

A two-phase flow is composed of two distinct phases with different physical and chemical properties. Generally, the secondary phase is dispersed into the primary phase. The mixture model as a submodel of the Euler-Euler approach has the capability of simulating homogeneous multiphase flows whereby the relative velocity due the secondary phase is neglected [138]. In this study, the mixture model is used to simulate multiphase flows, and Reynolds Averaged Navier Stokes (RANS) equations are employed to numerically study turbulence in cavitation formation for cavitating flows. Continuity and momentum balance equations are solved for the mixture, the volume fraction equation is solved for the secondary dispersed phase, and the relative velocities are taken into account using the algebraic expressions under the scheme of the mixture model.

The study of multiphase flows in small channels requires extensive knowledge and understanding on the flow characteristics. Therefore, it is essential to focus on the flow morphology inside the channels and decide on how variations of the physical and thermodynamical properties affect the flow.

3.2.1 Model Equations

The conservation of mass and momentum for the mixture in the case of steady state can be respectively written as,

$$\nabla \cdot (\rho \vec{v}) = 0 \tag{3.1}$$

$$\nabla \cdot (\rho \vec{\mathbf{v}} \vec{\mathbf{v}}) = -\nabla p + \nabla \cdot \left[\mu_T \left(\nabla \vec{\mathbf{v}} + (\nabla \vec{\mathbf{v}})^T \right) \right] + \nabla \cdot \left(\sum_{f=1} \alpha_f \rho_f \vec{\mathbf{v}}_{dr,f} \vec{\mathbf{v}}_{dr,f} \right) + \rho_T \vec{\mathbf{g}} + \vec{\mathbf{f}} \quad (3.2)$$

where $\vec{\mathbf{v}}$ is the mass-averaged velocity defined as $\vec{\mathbf{v}} = \sum_{f=1} \alpha_f \rho_f \vec{\mathbf{v}}_f / \rho$, ρ_T is the mixture density, α_f is the volume fraction of phase f , ρ_f is the density of the phase f , p is the pressure, $\vec{\mathbf{g}}$ is the gravitational acceleration, $\vec{\mathbf{f}}$ is the force body, μ_T is the mixture viscosity defined as $\mu_T = \sum_{f=1} \alpha_f \mu_f$, $\vec{\mathbf{v}}_{dr,f}$ is the drift velocity of the secondary phase defined as $\vec{\mathbf{v}}_{dr,f} = \vec{\mathbf{v}}_f - \vec{\mathbf{v}}$, and the superscript T is the transpose symbol.

The volume fraction equation for phase f can be introduced as,

$$\nabla \cdot (\alpha_f \rho_f \vec{\mathbf{v}}_f) = -\nabla \cdot (\alpha_f \rho_f \vec{\mathbf{v}}_{dr,f}) + \sum_{q=1} (\dot{m}_{qf} - \dot{m}_{fq}) \quad (3.3)$$

where \dot{m}_{qf} is the mass transfer from phase q to phase f and \dot{m}_{fq} is the mass transfer from phase f to phase q .

3.2.2 Cavitation modeling in cavitating flow configuration

In order to model turbulence in cavitation, instead of using computationally expensive Direct Numerical Simulation (DNS), RANS, being a more practical model, is used together with k - ϵ model with a standard wall function for the near-wall treatment. The turbulence viscosity is neglected in this model unlike the standard k - ϵ model. The transport equation for k (turbulent kinetic energy) and ϵ (turbulent dissipation rate) are given respectively as,

$$\nabla \cdot (\rho k \vec{\mathbf{v}}) = \nabla \cdot \left[\left(\mu + \frac{\mu_t}{Pr_k} \right) \nabla k \right] + G_k + G_b - \rho \epsilon - Y_M + S_k \quad (3.4)$$

$$\nabla \cdot (\rho \epsilon \vec{\mathbf{v}}) = \nabla \cdot \left[\left(\mu + \frac{\mu_t}{Pr_\epsilon} \right) \nabla \epsilon \right] + \rho C_1 S \epsilon + \rho C_2 \frac{\epsilon^2}{k + \sqrt{\nu \epsilon}} + C_{1\epsilon} \frac{\epsilon}{k} C_{3\epsilon} G_b + S_\epsilon \quad (3.5)$$

where $C_1 = \max[0.43, \eta/\eta + 5]$, $\eta = Sk/\epsilon$, and $s = \sqrt{2\mathbf{S} : \mathbf{S}}$, Here, S_k and S_ϵ are the user defined source terms, G_k , G_b and Y_M are the generation of the

turbulent kinetic energy due to mean velocity gradient, buoyancy, and fluctuations due to overall dissipation energy, respectively, Pr_k and Pr_ϵ are turbulent Prandtl numbers, μ_t is the turbulence viscosity, C_1 , $C_{1\epsilon}$, $C_{3\epsilon}$ and C_2 are constants and \mathbf{S} is the mean rate of strain tensor.

Modeling of cavitation as an unsteady process is a very challenging simulation task, and most of CFD softwares use basic cavitation models to simulate this phenomenon. The interface-tracking and multiphase approaches relying on the interfacial flow theorem and phase averaging concept are two possible methods that can be used to simulate cavitation. There are mainly three available cavitation models within the multiphase flow approach namely, the Singhal et al. model [139], the Zwart-Gerber-Belamri model [140] and the Schnerr and Sauer model [141]. In this study, the Schnerr and Sauer model is used since this model is capable of using various turbulence models, and can also be used with the Eulerian multiphase model. However, the interface-tracking methods such as explicit volume of fluid (VOF) is not suitable for all the cavitation models given that the surface tracking schemes in the VOF model are inconsistent with the fundamental assumptions of the cavitation models.

To account for mass transfer between liquid and vapor in the process of cavitation bubble formation, the required vapor transport equation can be formulated as,

$$\nabla \cdot (\alpha \vec{v}_v) = s \quad (3.6)$$

where α is vapor volume fraction, v is the vapor phase, \vec{v}_v is the velocity of vapor phase, and s is mass transfer source term. It should be noted that according to the saturation density of the vapor at a given temperature, the vapor density is constant. Cavitation models used in numerical simulations are based on the Rayleigh-Plesset equation given as,

$$R_B \cdot \frac{D^2 R_B}{Dt^2} + \frac{3}{2} \left(\frac{DR_B}{Dt} \right)^2 = \frac{p_B - p}{\rho_l} - \frac{4\nu_l}{R_B} \cdot \frac{DR_B}{Dt} - \frac{2S}{\rho_l R_B} \quad (3.7)$$

where R_B is the bubble radius, p_B is the pressure of the bubble surface, p is the far-field liquid pressure, S is the surface tension of the liquid and ν_l is kinematic viscosity of the liquid. Neglecting the surface tension force as well as the second-

order terms, the above equation simplifies to,

$$\frac{DR_B}{Dt} = \sqrt{\frac{2}{3} \cdot \frac{p_B - p}{\rho_l}} \quad (3.8)$$

The Schnerr and Sauer model used in this work is based on the simplified Rayleigh-Plesset equation and assumes that a large number of micro bubbles exist in the vapor phase of the flow. Considering the vapor volume fraction and the vapor transport equation presented in Equation 3.6, the net mass source term is obtained as,

$$s = \frac{\rho_v \rho_l}{\rho} \cdot \frac{D\alpha}{Dt} \quad (3.9)$$

The vapor volume fraction is expressed as a function of the number of bubbles present in a unit volume of liquid as follows [141],

$$\alpha = \frac{n_b 4/3\pi R_B^3}{1 + n_b 4/3\pi R_B^3} \quad (3.10)$$

Vapor volume fraction is then written as,

$$\frac{D\alpha}{Dt} = \frac{(1 - \alpha) 4n_b \pi R_B^2}{1 + n_b 4/3\pi R_B^3} \cdot \frac{DR_B}{Dt} = \frac{3}{R_B} \alpha (1 - \alpha) \frac{DR_B}{Dt} \quad (3.11)$$

Finally, the mass transfer rate can be obtained using Equations 3.6, 3.8 and 3.11 as,

$$s = \frac{\rho_v \rho_l}{\rho} \cdot \frac{3\alpha(1 - \alpha)}{R_B} \cdot \sqrt{\frac{2}{3} \cdot \frac{p_B - p}{\rho_l}} \quad (3.12)$$

The final form of the model to represent evaporation and condensation processes is expressed as follows,

Evaporation when $p_B \geq p$,

$$s = \frac{\rho_v \rho_l}{\rho} \cdot \frac{3\alpha(1 - \alpha)}{R_B} \cdot \sqrt{\frac{2}{3} \cdot \frac{p_B - p}{\rho_l}} \quad (3.13)$$

Condensation when $p_B \leq p$,

$$s = \frac{\rho_v \rho_l}{\rho} \cdot \frac{3\alpha(1 - \alpha)}{R_B} \cdot \sqrt{\frac{2}{3} \cdot \frac{p - p_B}{\rho_l}} \quad (3.14)$$

3.2.3 Numerical Validation Test Case: Micro-Jet Impingement

Micro-jet impingement simulations were performed in order to provide a validation for the numerical approach, which was utilized in the rest of the present work. To this end, the computational domain in Figure 3.1 is simulated using the FLUENT 16.0 software and user defined subroutines. The results are benchmarked with the existing data in the literature. The domain has an inlet in the middle of the upper wall with a velocity boundary condition, while the upper and lower walls are subjected to no-slip boundary condition. The outlets at both sides of the study domain are treated as non-reflecting boundaries by prescribing convective flux therein [142], which is implemented writing a user defined function (udf). The validation test problem at hand is simulated for four different aspect ratios (H/D), namely from 2 to 5 and for different Reynolds numbers ranging from 50 up to 500. The effect of jet impingement on the stagnation point and wall is investigated referring to the skin friction factor and pressure coefficient, respectively, which are calculated as $C_p = (p - p_{jet}) / 0.5\rho v_{jet}^2$, and $C_f = \tau_w / 0.5\rho v_{jet}^2$. Here, v_{jet} is the velocity magnitude in y direction. Moreover, velocity contours of the test cases are also compared among each other.

A pressure-based solver is chosen for simulations, and the laminar-viscous model is selected for all the Reynolds numbers in a steady single phase flow. Coupled scheme is utilized as the pressure-velocity coupling solution method, and the least squares cell based, standard, second order upwind scheme is used to discretize the gradients in pressure and, momentum equations, respectively. Continuity and velocity components are selected as the residuals, and the absolute error for the convergence criterion is set to 1e-5. In the transient solutions, adaptive time stepping is employed with the initial time step of 1e-2 *seconds*.

3.2.4 Estimation of Uncertainty due to Discretization Error Using Grid Convergence Index

Grid refinement study is performed to ensure that by reducing the size of grid cells and increasing the number of cells, the spatial discretization error asymptotically

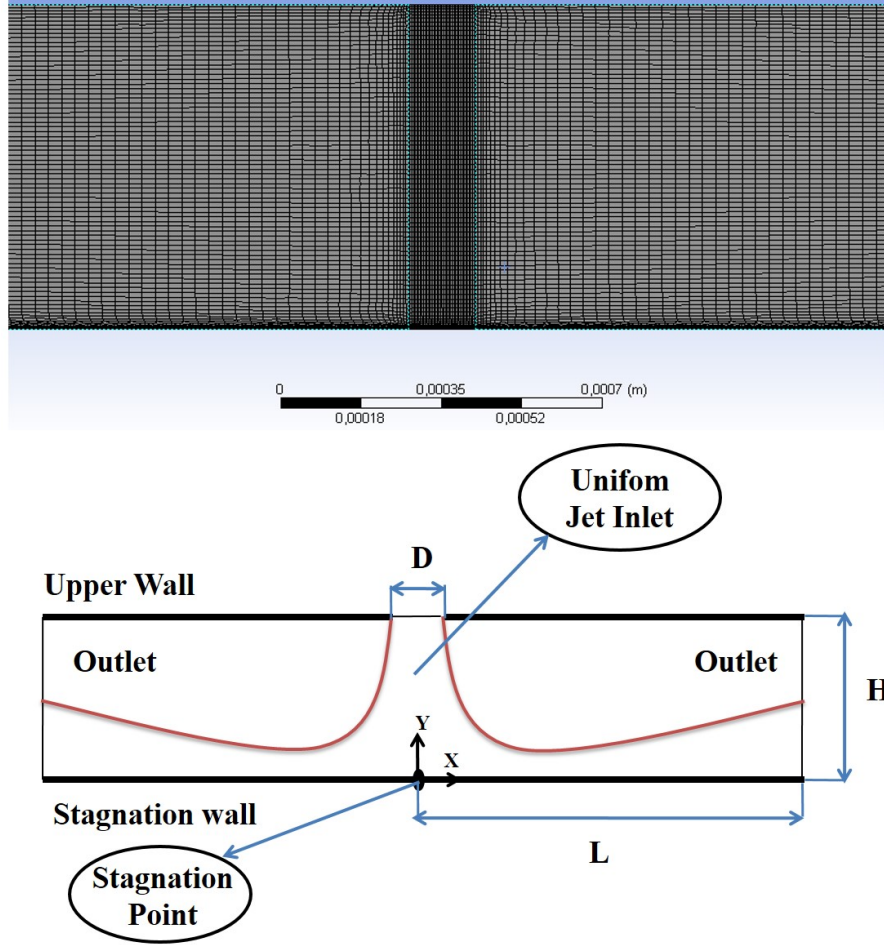


Figure 3.1: The computational domain used in modeling micro-jet impingement for validation ($H/D=5$)

approaches to zero. Convergence criterion studied by Roache [143] based on the Richardson's extrapolation presented Convergence Grid Index (GCI). This index provides an error band, which involves the convergence of the solution and investigates the asymptotic range of convergence for the obtained solutions. Therefore, the GCI provides an estimation of how small is the discrepancy between the measured value and the asymptotic numerical value. The discretization error studied in GCI does not include the round off error, which is small enough to neglect. The solution error, which is the difference between exact and measured values, is related to the order of grid convergence as follows:

$$E = f(h) - f_{exact} = C \cdot h^r + H.O.T. \quad (3.15)$$

where h is the grid spacing, r is the order of convergence and C is a constant. Neglecting higher order terms (H.O.T.) and taking logarithm of both sides, Equ-

tion 3.15 leads to:

$$\log(E) = \log(C) + r \log(h) \quad (3.16)$$

Representative mesh size is obtained from the below formula for two dimensional calculations:

$$h = \left[\frac{1}{N} \sum_{i=1}^N (\Delta A_i) \right]^{0.5} \quad (3.17)$$

where ΔA_i is the area of the i -th cell, and N is the total number of cells used for the computations, and the above equation is used for calculating the integral quantity, namely skin friction coefficient. Mesh independency tests are performed for the test case with an aspect ratio of 5 via conducting simulations with coarse, intermediate and fine grids (Figure 3.2).

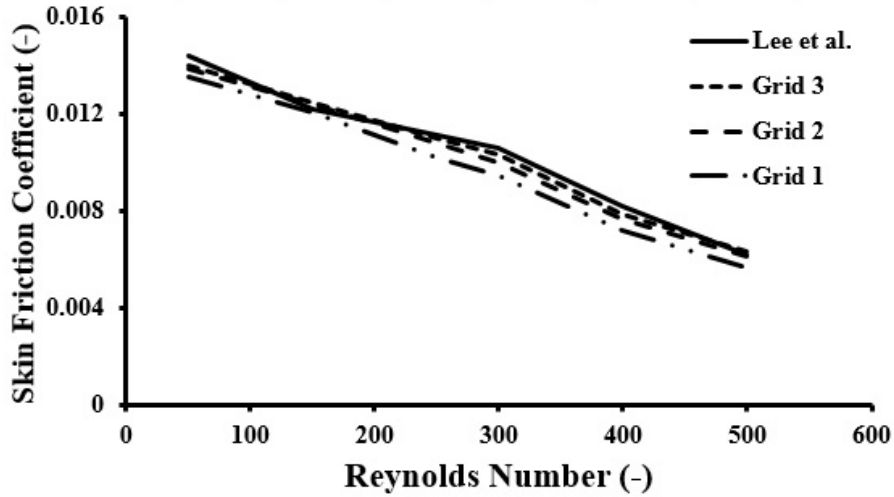


Figure 3.2: The skin friction coefficient for different cell numbers for the aspect ratio of 5

Since three solutions were considered in the grid refinement study, the order of convergence is obtained using a constant grid refinement ratio u as follows:

$$r = \ln \left[\frac{f_3 - f_2}{f_2 - f_1} \right] / \ln u \quad (3.18)$$

Asymptotic solution is obtained using the Richardson extrapolation generalized for a r -th order methods and u -value of grid ratio as follows:

$$f_{h=0} = f_1 + \frac{f_1 - f_2}{u^r - 1} \quad (3.19)$$

The GCI on the fine grid is defined as follows:

$$GCI_{fine} = \frac{F_S |f_2 - f_1|}{(u^r - 1)} \quad (3.20)$$

where F_S is a factor of safety and is recommended to be 1.25 when three or more grids are compared. Finally, to check whether the solutions are within the range of the asymptotic convergence, three computed grids were compared using the below equation:

$$GCI_{23} = u^r \cdot GCI_{12} \quad (3.21)$$

Table 3.2 illustrates the convergence criteria based on the data presented in Table 3.1 for the order of convergence, the asymptotic solution, GCI for the different solutions and the ratio between the grid convergence indices. Table 3.2 shows that the solutions are in the asymptotic range and indicates that lower Reynolds number results have higher convergence order and lower grid convergence index, while higher Reynolds numbers solutions have a lower convergence order and higher grid convergence index, which is related to the higher velocity field and disturbed flow regime. Asymptotic solution presented in Table 3.2 exhibits the best approximations based on the data gathered from different grid sizes.

Table 3.1: Results of skin friction coefficient for different grid spacing sizes

Re Number	Mesh	h (mm)	C_f
50	1	0.044	0.013505
	2	0.022	0.013871
	3	0.011	0.013964

3.2.5 Modeling Cavitating Flows in Micro/Mini-Channels

Having validated the numerical approach, cavitating flows inside micro/mini-channels are simulated using the numerical approach used in the validation step whereby the effect of upstream pressure and diameter on vapor fraction inside the channel and

Table 3.2: Grid convergence index (GCI) for different Reynolds numbers

Reynolds Number	Order of Convergence (r)	Asymptotic Solution ($f_{h=0}$)	$a = GCI_{12} \%$	$b = GCI_{23} \%$	$a/u^r b$
50	2.0199	0.0139	0.0026	0.0107	1.0064
150	2.4993	0.0124	0.0012	0.0068	1.0045
250	1.8828	0.0110	0.0073	0.0274	1.0160
300	1.0435	0.0105	0.0331	0.0702	1.0289
400	1.1129	0.0083	0.0291	0.0648	1.0279
500	1.0426	0.0065	0.0427	0.0914	1.0377

major differences between micro/macro flow morphologies could be substantiated. The computational domain is a channel with a micro/mini-orifice as shown in Figure 3.3.

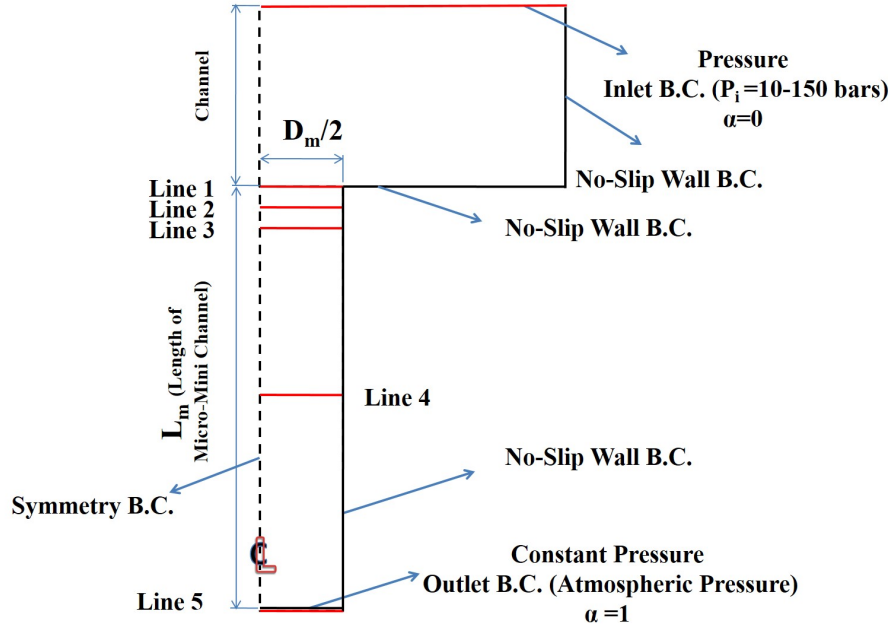


Figure 3.3: The second study domain for modeling the micro-channel ($D_m = 762 \mu\text{m}$)

The domain considered in this study is chosen considering the experimental setup utilized in our previous study [18], which is a channel with different inner diameters connected to a channel with an inner diameter of 3 mm. The lengths, diameters, aspect ratios, and thermophysical properties in the previous study [18] are used as the input in numerical simulations. The boundary conditions are inlet pressure for the channel and constant outlet pressure for the orifice. For the inlet and outlet, different volume fractions are assigned to the mixture of primary liquid and secondary

vapor phases. The computational domain is discretized with quadrilateral mesh along the channel and orifice. To be able to improve the accuracy of the numerical solution, finer and uniform mesh is utilized at the orifice given that cavitation bubbles start forming here. In this study, the multiphase-mixture module using a pressure-based solver is utilized wherein the gravity is neglected, and steady cavitating flow was simulated in the 2-D axisymmetric geometry. The turbulence is modeled using the two-equation based $k-\epsilon$ model with a standard wall function for the near-wall treatment as explained in section 3.2.2. The no-slip and symmetric boundary conditions are imposed for the walls and the left-hand side of the model, respectively. The numerical procedure utilized for this problem is the same as one used in micro-jet impingement simulations. Quick scheme is selected for discretization of the momentum, volume fraction, and turbulent kinetic energy. Continuity, velocity, k and epsilon components are selected as the residuals for monitoring the convergence, and the absolute error for the convergence figure criterion is $1e-5$. Similar to micro-jet impingement simulations, in transient simulations, adaptive time incrementation is used with the initial time step of $1e-2$ seconds.

In this study, four micro and mini-channels/orifices with different inner diameters, D_m , (152, 254, 504 and, 762 μm) are modeled, and flow characteristics inside the micro and mini-channel/orifice are analyzed in detail on five different lines as illustrated in Figure 3.3. Three of these lines are located at distances of 0.0006, 0.0008, and 0.0016 mm from the inlet of the channel/orifice, while the other two are located exactly at the inlet and outlet of the channel/orifice. The second and third lines are close to the contraction since the significant portion of cavitation bubbles are formed in these sections, which are rather critical for cavitation inception. L_m is the length of the micro/mini-channel, which is 3 mm , and the edge at the beginning of the micro/mini-channel is completely sharp in order to control the separation and reference single phase flow. The static pressure, vapor volume fraction, velocity magnitude, and cavitation number are evaluated in these regions and then presented in detail for different cases.

3.3 Results and Discussion

The results of numerical and experimental investigations are provided in this section. The results of the micro-jet impingement modeling study are compared with the results of literature and are discussed in detail. Subsequently, pressure variations for cavitating flow conditions are provided along mini and micro-orifice configurations. Referring to results of numerical studies, one can observe that the vapor phase extends to the end of the orifice configurations at higher upstream pressures whereby bubble collapse occurs not only inside the orifice, but also at its outlet.

3.3.1 Micro-Jet Impingement

Figure 3.4 shows the pressure coefficient at four different aspect ratios (namely, 2, 3, 4 and, 5). Reynolds number used in this section is defined as $Re = \rho v_{jet} D / \mu$, where ρ is the density of the fluid flow, v_{jet} is the velocity of the flow at the inlet, D is the inlet diameter, and μ is the viscosity of the fluid flow. The variation of the pressure coefficient as a function of position for the given aspect ratio is dependent on Reynolds number. It follows a similar trend for all Reynolds numbers except $Re=50$. For $Re=50$, the velocity has a rather low magnitude (0.34 m/s), and the pressure coefficient has a negative magnitude at the end of the domain at both sides. However, as the aspect ratio increases, the pressure coefficient for $Re=50$ becomes larger and approaches to the other cases. This is because as the aspect ratio becomes larger, the liquid jet has more space to be distributed along the domain and the jet pressure becomes lower. At higher aspect ratios, due to severe separation effects of the liquid jet from the lower wall and lower jet pressure, the pressure coefficient increases at both sides. For these aspect ratios, as the outlet boundary condition is convective flux and the liquid jet slightly contacts with the lower and upper wall, the pressure coefficient distribution retains the same trend. The pressure coefficient has the highest value exactly at the stagnation point and increases with Reynolds number for all aspect ratios.

Figure 3.5 illustrates the comparison of simulation results with the available numerical studies in the literature for different aspect ratios. The pressure coefficient was calculated at the lower wall for all Reynolds numbers and aspect ratios. This

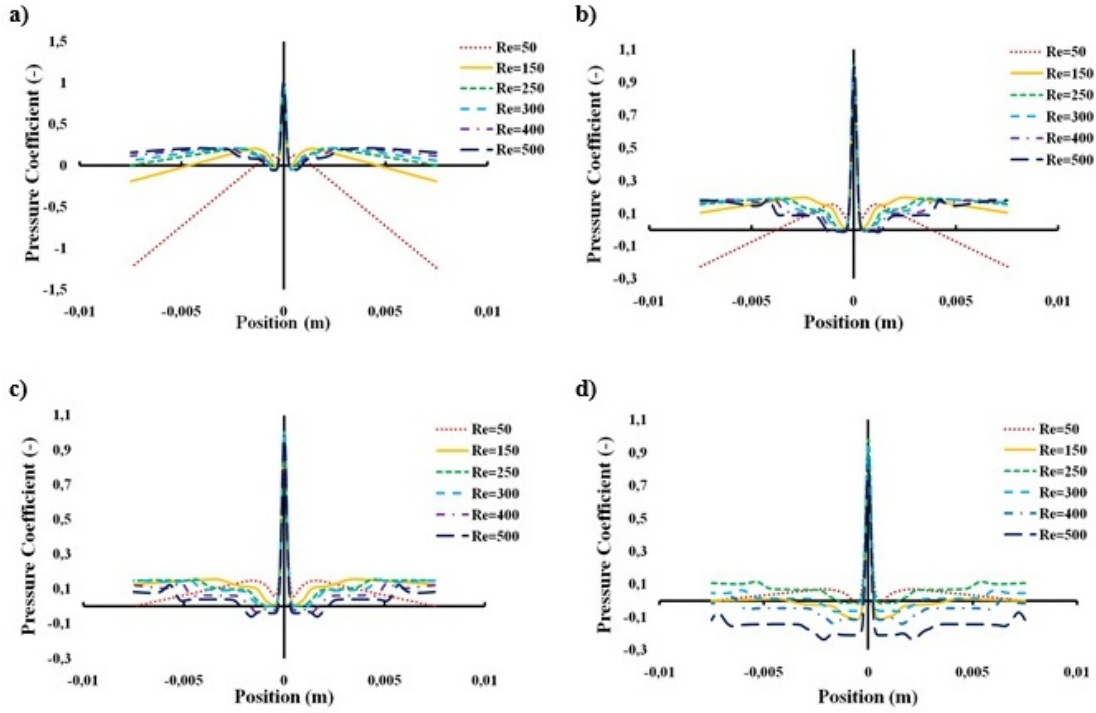


Figure 3.4: Pressure coefficient as a function of Reynolds number for different aspect ratios (a) $H/D=2$ (b) $H/D=3$ (c) $H/D=4$ (d) $H/D=5$

figure indicates that the results are in a good agreement with the numerical study of Lee et al. [142]. As can be seen from this figure, the mean pressure coefficient at the lower wall dramatically increases at Reynolds numbers between 50 to 150 for all the cases and decreases beyond this point particularly for the aspect ratio of 5, which matches with the results of Lee et al. [142]. Velocity contours for different aspect ratios at $Re=500$ are shown in Figure 3.6. It can be observed that the fluid flow extends after contacting the stagnation point with the increase in the aspect ratio. The intensity of the liquid jet is also augmented at higher aspect ratios. The maximum velocity of the liquid jet is 3.223 m/s corresponding to $Re=500$ for all the cases, and the contacting point on the upper wall changes with the aspect ratio. The fluid flow at the outlet of the domain exits to the outside, while it does not get back to the domain for all the cases, since the boundary condition for the outlet was set to the convective flux boundary condition [142].

Figure 3.5 shows that the pressure coefficient for $Re=50$ is lower than 1 for all the aspect ratios, since the convective force of the micro-jet at the inlet of the domain is not enough to change the momentum of the jet to the pressure at the lower wall. The micro-jet sways more along the center of the domain for aspect ratios of 4 and 5

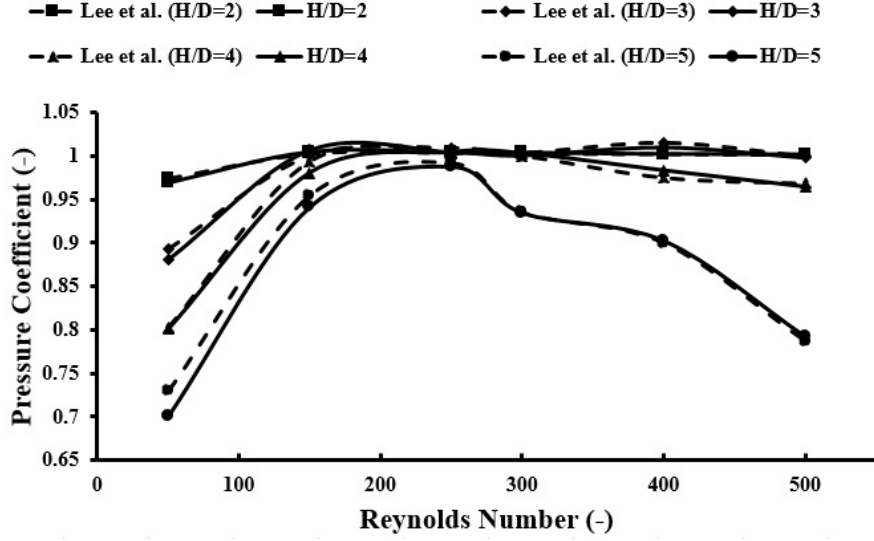


Figure 3.5: The comparison of the pressure coefficient with the available numerical results in the literature

at higher Reynolds numbers and loses the kinetic energy while the small vortices are being formed. Therefore, high velocities at the higher Reynolds numbers for aspect ratios of 4 and 5 hinder the micro-jet from stagnating with the lower wall and cause a reduction in pressure coefficient as shown in Figure 3.5.

3.3.2 The effect of Turbulence on the Fluid Flow Regime Inside Micro/Mini-Channels

The mean velocity of the flow is obtained on the lines inside the micro/mini-channels. The velocity inside the micro/mini-channels varies between 29 and 149 m/s . The Mach number is expressed as $Ma = \bar{V}/a$, where a is the speed of sound in the liquid and \bar{V} is the mean velocity value on each line, and it varies between 0.019 and 0.1, which implies an incompressible flow for all the cases. The orifice Reynolds number is calculated using the definition, $Re = \rho \bar{V} D_m / \mu$, where ρ is the density of the flow, D_m is the diameter of the micro/mini-channel and μ is the fluid viscosity. The viscosity is found on each line. By utilizing the average velocity on the lines, Reynolds number is found to be between 4,534 and 77,041, which proves turbulent effects on fluid flow on all the lines and all the micro/mini-channels. Although fluid flows inside small channels have been studied under both laminar and turbulent conditions, the data for turbulent flows is rather scarce for micro scale structures in the litera-

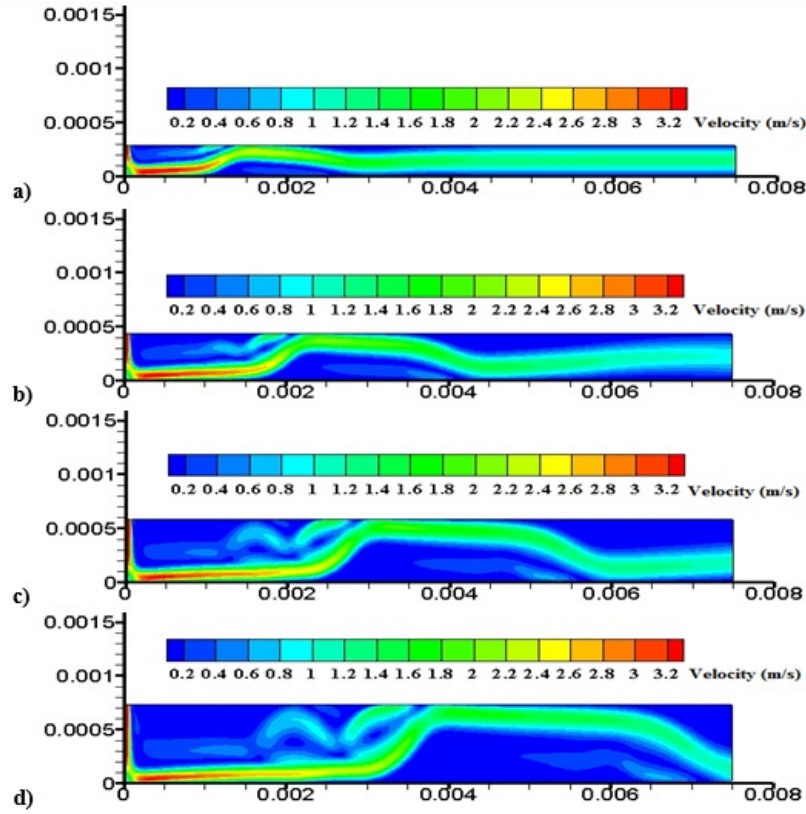


Figure 3.6: The velocity profile for different aspect ratios at $Re=500$ (a) $H/D=2$ (b) $H/D=3$ (c) $H/D=4$ (d) $H/D=5$

ture such that the highest value of Reynolds number reported was 25,000 [14] and only single phase flows were considered. In this study, cavitating flow characteristics in mini/micro-orifices are examined at high Reynolds number while considering the turbulent effects which is vital for the implementation of hydrodynamic cavitation to futuristic economical and energy efficient therapies such as abnormal tissue ablation and kidney stone treatment [18].

Mean velocities on each line for the micro/mini-channels are shown in Figure 3.7 for upstream pressures of 10, 50, 80 and 150 *bar*. As shown in this figure, an increase in the upstream pressure leads to an increase in the velocity on all lines and the slope of each line. For all cases, the mean velocity has the highest value on the line 4, which is located at the middle of the channel.

The maximum value of the mean velocity on this line necessitates that the local static pressure should have the lowest value at this location whereby the vapor phase can extend to this location. The velocity beyond this line decreases due to decline in the vapor phase fraction and getting closer to the outlet of the micro/mini-channel.

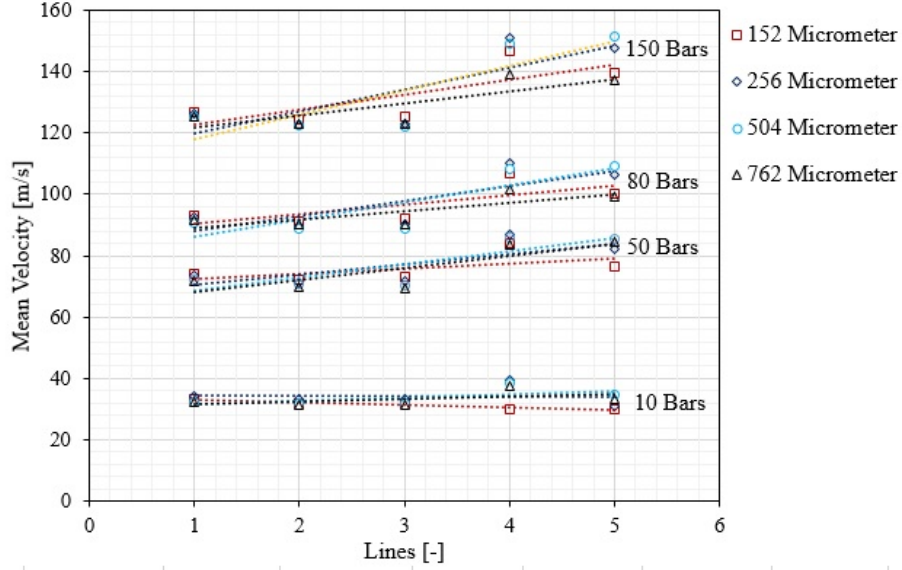


Figure 3.7: The variation of mean velocity on the lines inside the micro/mini-channels

Microchannels have higher velocities on the first lines compared to mini-channels, since many vapor bubbles form in the vicinity of the inlet of micro-channels. In addition, the local static pressure has lower values at the inlet of micro-channels. On the other hand, mini-channels have higher velocities toward the outlet, which suggests that more cavitation bubbles are present near the outlet of mini-channels. Decreasing trend in the velocity on the lines 2 and 3 in all the cases proves that vena contracta exists in these regions, which are close to the inlet. This behavior is somewhat less observed at the upstream pressure of 10 *bar* indicating that fewer cavitation bubbles are generated at this pressure.

Figure 3.8 shows the ratio of the turbulence kinetic energy for different upstream pressures. Turbulence kinetic energy (TKE), which is approximately the summation of velocity variance, indicates the intensity of the vorticities generated due to the instabilities and unsteadiness. Cavitation phenomenon is often accompanied by turbulence and as indicated in Figure 3.7, the existence of high velocities and high Reynolds numbers intensifies the generation of vorticities. It is well-known that the collapse of cavitation bubbles inside the nozzle is one of the significant reasons of turbulence and vorticity generation. The results in this study present large values for turbulence kinetic energy especially for micro-channels, when the upstream pressure is high. Turbulence kinetic energy at low pressures shows the same behavior. An increase in the pressure results in big deviations between micro and mini-channels.

The turbulence intensity in the whole channel is almost two times bigger for micro-channels at higher upstream pressures compared to mini-channels. γ presented in Figure 3.8 is the TKE ratio.

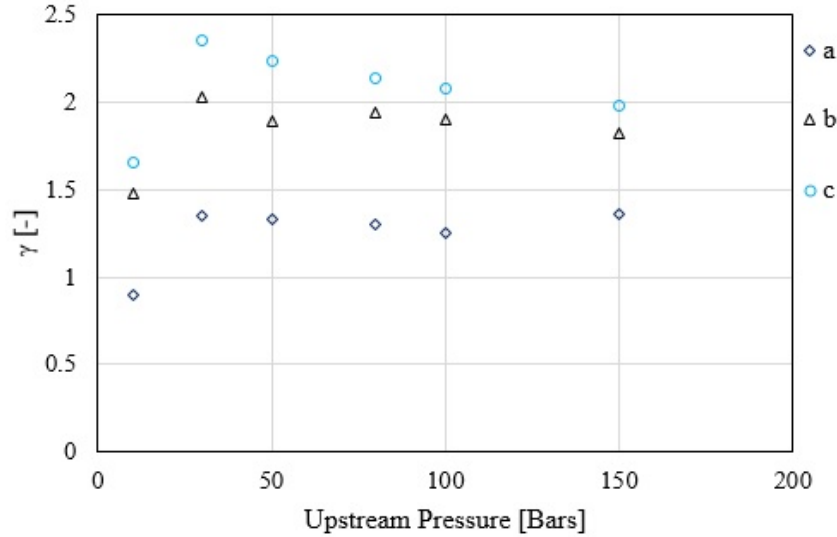


Figure 3.8: The ratio of TKE for different upstream pressures. (a, b, c) the ratio of TKE of the micro-channel with the diameter of $152 \mu\text{m}$ to the micro-channels with diameter of $254 \mu\text{m}$, $504 \mu\text{m}$, and $762 \mu\text{m}$, respectively

In this regard, Figure 3.8 shows the ratio of the TKE of micro-channel with the diameter of $152 \mu\text{m}$ to the micro-channel of the diameter of $254 \mu\text{m}$ (a), to the mini-channel of the diameter of $504 \mu\text{m}$ (b), and to the mini-channel of the diameter $762 \mu\text{m}$ (c), respectively. TKE of the micro-channel with the diameter of $152 \mu\text{m}$ is two times bigger than the mini-channels for the most of the upstream pressures (b and c), while the ratio between the micro-channels of two different sizes is less than 1.5 for all the cases (a). Since Reynolds number is not very high at the upstream pressure of 10 bar , turbulence does not have any significant impact on fluid flow. Thus, the ratios of TKE in all the cases are low at this pressure. Beyond this pressure, the ratio of TKE has a sharp increase for all the cases, which suggests the growing effect of turbulence and cavitation inception beyond this pressure. Meanwhile, wall shear stress values displayed in Table 3.3 show the significance of this parameter in the channels with small diameters. A decrease in the diameter of the channel leads to an increase in shear stress, which is one of the indicators of the effect of turbulence. Furthermore, static pressure along the channel, velocity and vapor volume fraction are significant parameters that needs to be considered in

cavitating flows in micro/mini scale for capturing the physics of cavitating flows in small scale.

Table 3.3: Wall shear stress (Pa) for different channels at low and high upstream pressures

Upstream Pressure (<i>bar</i>)	$152\ \mu\text{m}$	$254\ \mu\text{m}$	$504\ \mu\text{m}$	$762\ \mu\text{m}$
10	6593	4368	2388	1996
150	7926	6797	3048	2935

Normalized cavitation length, which is defined as the ratio of the length of cavitation region inside the channel to the length of the channel, is presented in Figure 3.9 for different orifice diameters. The results illustrate the same trend as the study of Henry and Collicott [13]. With an increase in channel diameter, the cavitation length becomes longer. The cavitation bubbles can extend to the exit of the channel at lower pressure drops for channels with larger diameters. The results in Figure 3.9 emphasize on the importance of the thickness ratio (L/D) presented in Table 1.1. While the thickness ratio of the channels in Henry and Collicott [13] was between 1.96 and 10.71, it is between 3.93 and 17.73 in this study. Therefore, the cavitation bubbles fill more space at the same pressure drop. The effect of the thickness ratio was widely studied in Cioncolini et al. [14] and Chisholm [144]. The cavitation length is affected by this ratio, which controls the multiphase flows inside the channel. The results exhibit major differences in cavitating flows between micro and mini-channels. The cavitation inception occurs at lower upstream pressures in mini-channels, while longer cavitation lengths are observed in mini-channels at the same upstream pressure compared to micro-channels.

3.3.3 The Pressure Variations Inside Micro-channels with Different Diameters

In Figure 3.10 to Figure 3.13, the pressure variation for different orifice diameters and upstream pressures are displayed. The pressure data was extracted from the simulation results for separate horizontal locations (lines) along the micro-channel/orifice to compare various cases among each other. For the location corresponding to the line 1, the pressure has the highest value for all cases prior to the inception of cavitation phenomenon and dramatically decreases near the wall of the micro-channel due

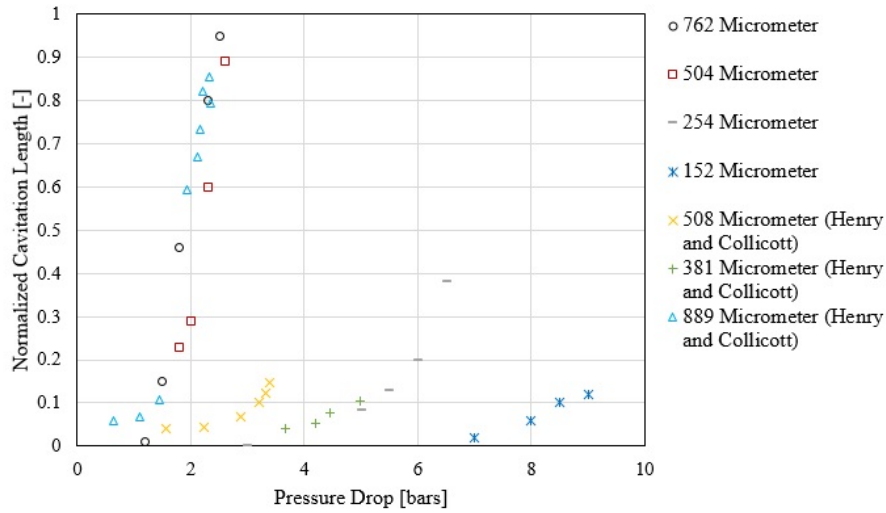


Figure 3.9: Normalized Cavitation length for different channel diameters and pressure drops

to inception of the cavitation. The pressure decreases at the locations corresponding to the lines 2 and 3 due to intensification of generation of cavitation bubbles, and has the lowest value near the wall for all cases (Figure 3.10 to Figure 3.13). The pressure recovery is observed between the lines 4 and 5 for all cases, where the pressure falls below the vapor saturation pressure at the location corresponding to the line 4 for almost all cases and then it increases to the atmospheric pressure at the location corresponding to the line 5.

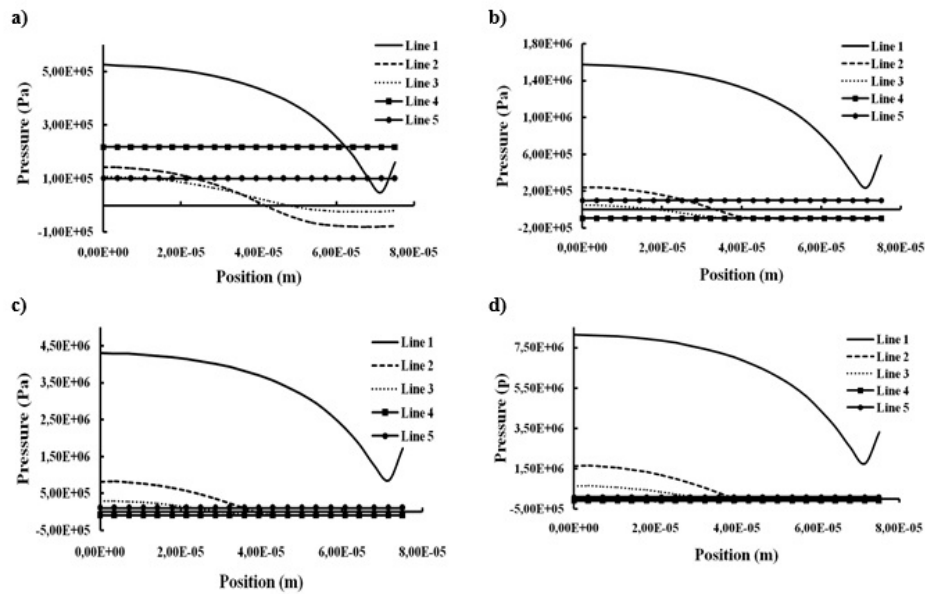


Figure 3.10: Pressure variation for different upstream pressures on different lines ($D_m = 152 \mu\text{m}$) (a) $p_i = 10 \text{ bar}$ (b) $p_i = 30 \text{ bar}$ (c) $p_i = 80 \text{ bar}$ (d) $p_i = 150 \text{ bar}$

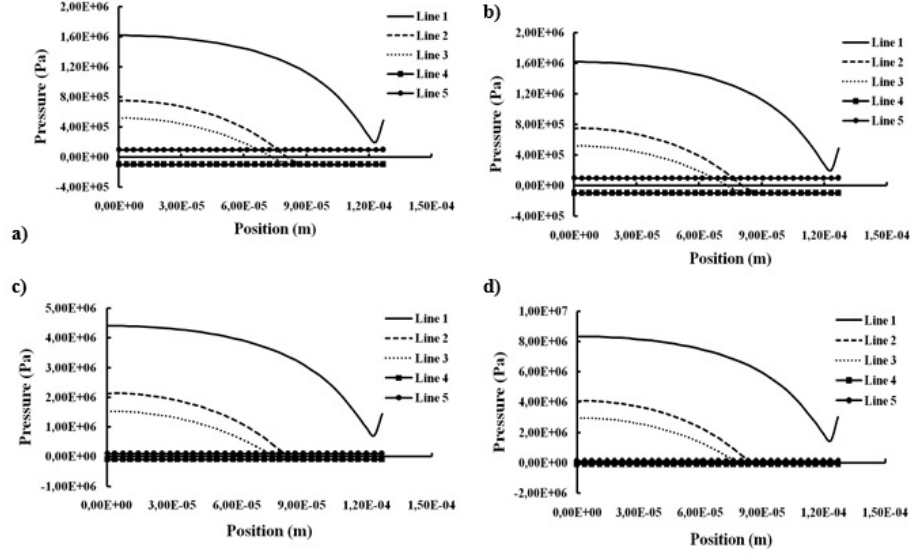


Figure 3.11: Pressure variation for different upstream pressures on different lines ($D_m = 254 \mu\text{m}$) (a) $p_i = 10 \text{ bar}$ (b) $p_i = 30 \text{ bar}$ (c) $p_i = 80 \text{ bar}$ (d) $p_i = 150 \text{ bar}$

One may note from the relevant Figures (refer to Figure 3.10 to Figure 3.13) that there exists a significant pressure profile difference between micro and mini/macro-channels. For micro scale channels with the inner diameters of 152 and 254 μm , as seen from Figure 3.10 and Figure 3.11, the pressure incurs negative values near the wall on the lines 2 and 3 for all upstream pressures whereby these regions have the highest possibility of cavitation inception and extensions of the cavitation bubbles. Except the case given in Figure 3.10 (a), tensile stresses are present on all the points of line 4 for all the cases, which indicate the presence of cavitation bubbles over the whole cross section corresponding to this line. The test case with $p_i = 10 \text{ bar}$ and $D_m = 152 \mu\text{m}$ corresponds to a rather low upstream pressure incapable of generating a large amount of cavitation bubbles inside the micro-channel, and therefore, the small amount of cavitation bubbles generated at the inlet of the micro-channel could not extend over the rest of the channel. On the other hand, the lowest pressure value obtained for the mini-channel (having an inner diameter of 504 and 762 μm) is nearly in the range of the vapor saturation pressure at the location corresponding to the line 4. The findings presented in Figure 3.10 to Figure 3.13 indicate that the effect and the extension of the cavitation phenomenon in micro-channels, especially downstream the channel, is more severe in comparison to the mini/macro-channels. Furthermore, the reduction in the pressure from the line 1 to the lines 2 and 3 is very

high in the micro-channels especially with the one of $D_m = 152 \mu\text{m}$ in comparison to the mini-channels, which implies that the cavitation bubbles are generated at a close distance to the inlet of the micro-channel.

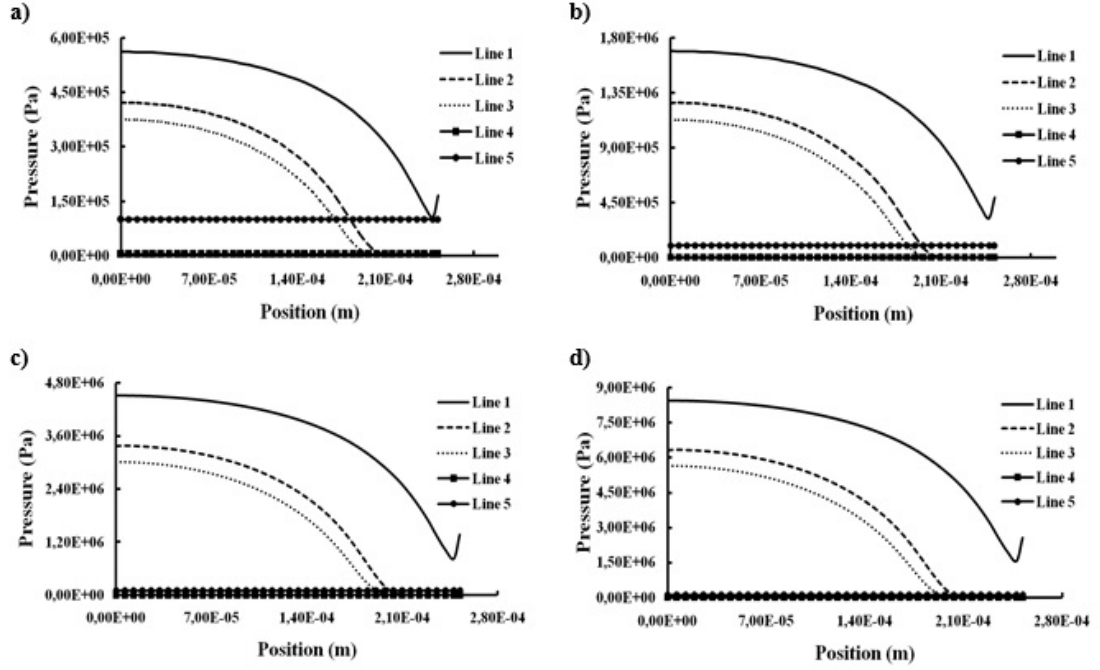


Figure 3.12: Pressure variation for different upstream pressures on different lines ($D_m = 504 \mu\text{m}$)(a) $p_i = 10 \text{ bar}$ (b) $p_i = 30 \text{ bar}$ (c) $p_i = 80 \text{ bar}$ (d) $p_i = 150 \text{ bar}$

The pressure variation for all cases corresponding to the lines 1 and 3 is demonstrated in Figure 3.14 and Figure 3.15 in order to shed light on the difference in the pressure distribution between micro and mini/macro-channels. At a given upstream pressure, the micro-channels have lower pressures for all the cases on the line 1 than mini-channels (Figure 3.14).

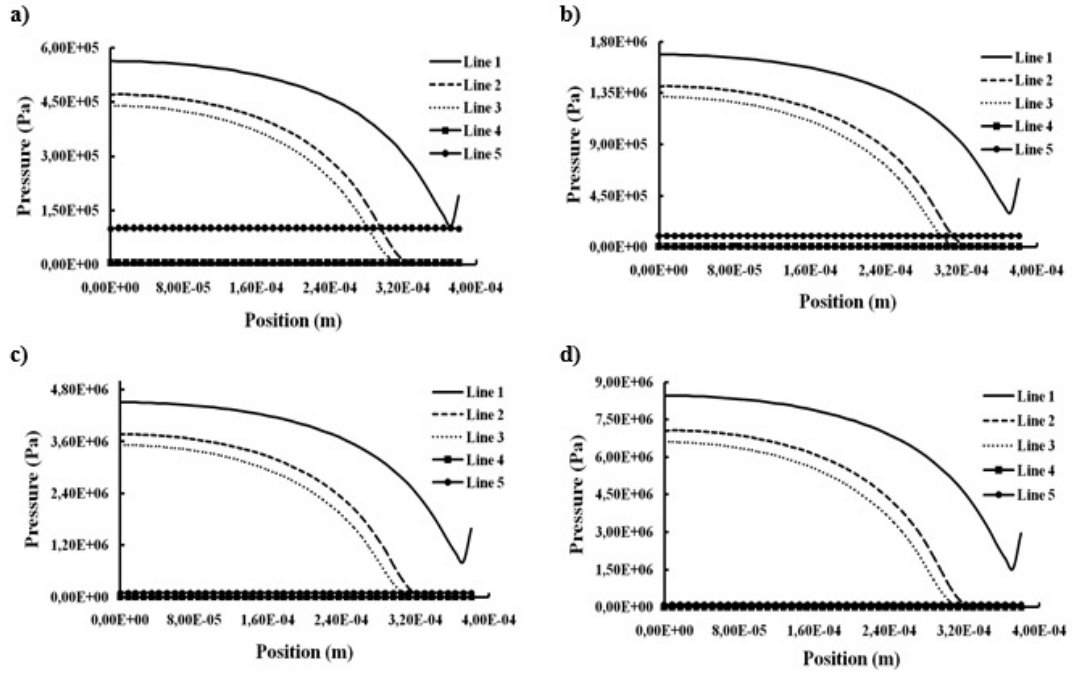


Figure 3.13: Pressure variation for different upstream pressures on different lines ($D_m = 762 \mu\text{m}$) (a) $p_i = 10 \text{ bar}$ (b) $p_i = 30 \text{ bar}$ (c) $p_i = 80 \text{ bar}$ (d) $p_i = 150 \text{ bar}$

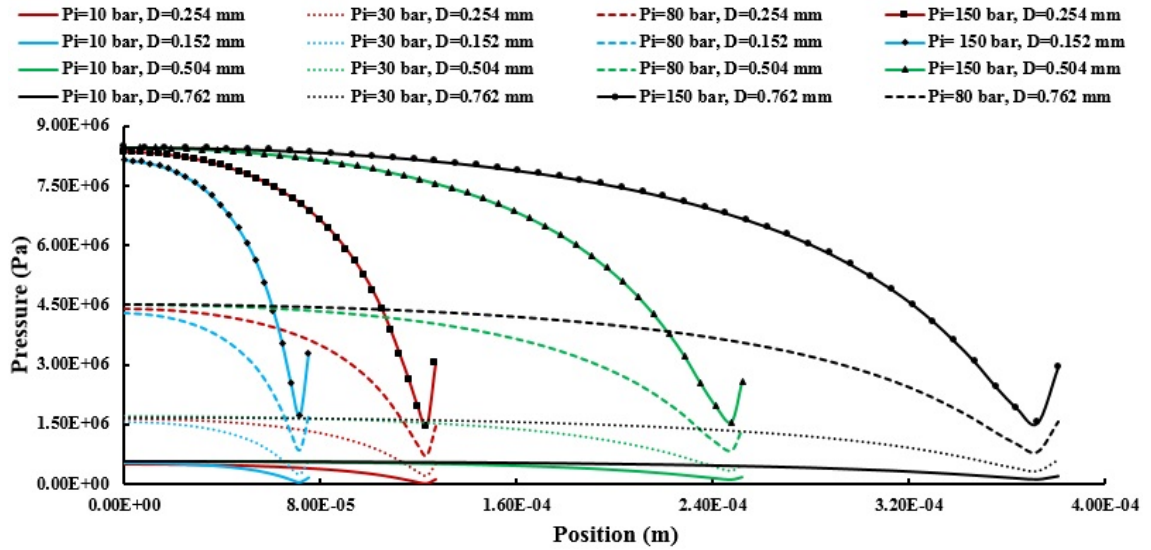


Figure 3.14: Pressure variation for different upstream pressures and inner diameters on Line-1

The comparison between Figure 3.14 and Figure 3.15 shows that the pressure difference between the micro/mini-channels is larger on the line 3 than on the line 1 for a given inlet pressure. For all cases of micro-channels, the pressure has negative values (tensile stress) on the line 1, which clearly suggests that the cavitation inception occurs near the inlet. However, as the diameter of the channel increases,

cavitation inception takes place at a downstream location of the channel.

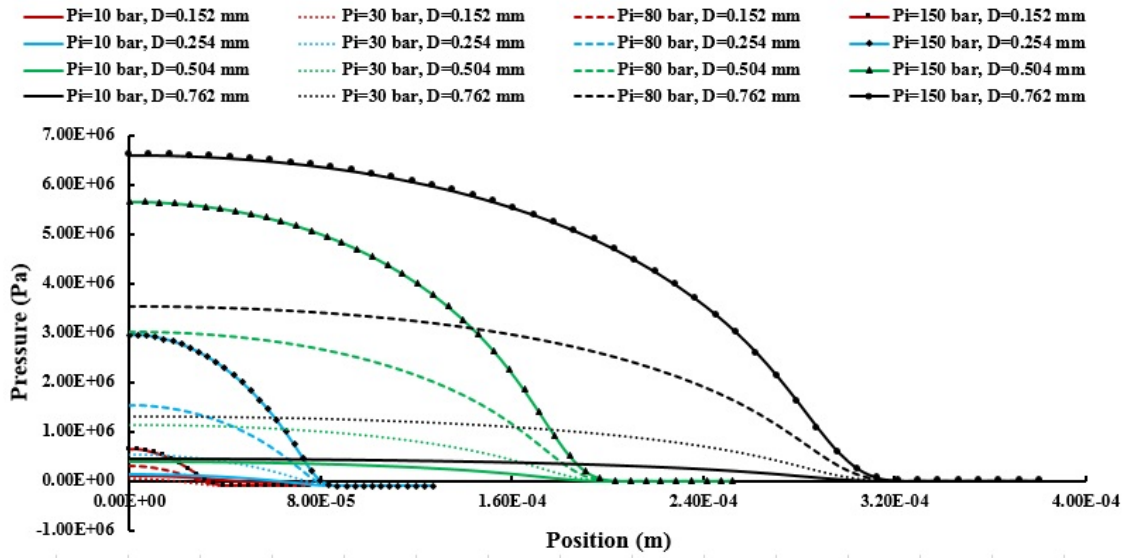


Figure 3.15: Pressure variation for different upstream pressures and inner diameter on Line-3

The pressure contours of the channels with different inner diameters are shown in Figure 3.16 for the upstream pressure of 150 *bar*. As can be seen, the pressure has the lowest value near the inlet of the channel for all the cases, and starts to decrease considerably as the diameter of the channel decreases. The results show that the cavitation number has a different distribution for different diameters. Referring to Table 3.4, the cavitation number has a lower value for the upstream of the micro-channels, illustrating the presence of high density of cavitation bubbles. The cavitation number-which is considered as an important parameter in the cavitating flow- is tabulated in Table 3.4 for the first three lines across the channels. The cavitation number for the line 1 for the micro-channel with the inner diameter of 152 μm is 0.71, while it is 0.85 for the mini-channel with the inner diameter of 762 μm . Similarly, the cavitation numbers for the micro-channel and mini-channel with the inner diameters of 152 and 762 μm for the line 3 are 0.008 and 0.52, respectively, which implies the formation of higher density of cavitation bubbles upstream the channel in the micro-channel. The increase in the diameter of mini-channels leads to the rise in the cavitation number, suggesting that as the channel diameter increases, the density of cavitation bubbles gets lower.

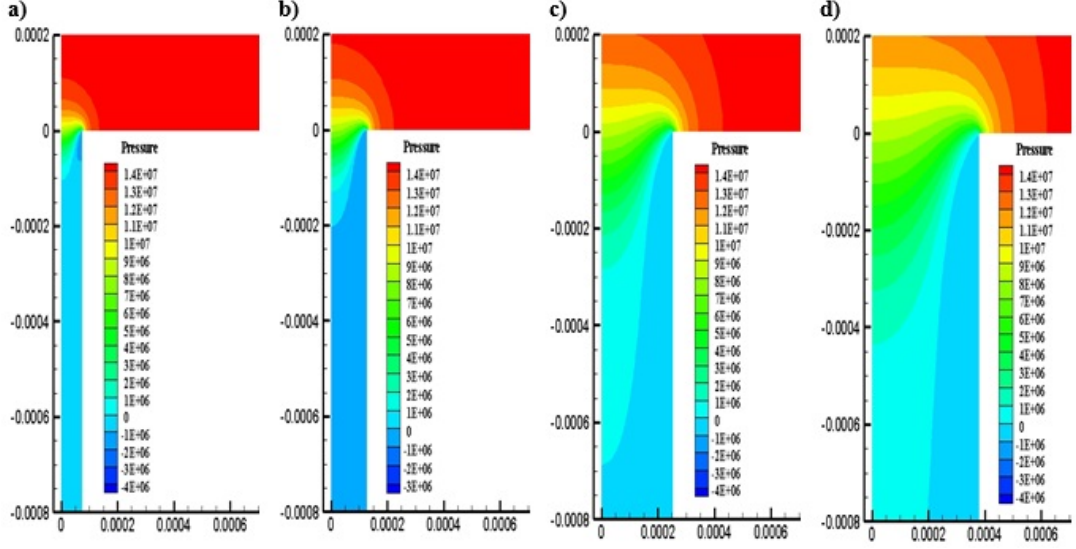


Figure 3.16: Pressure profile inside the channels at an upstream pressure of 150 *bar* for (a) 152 μm (b) 254 μm (c) 504 μm (d) 762 μm

Table 3.4: The cavitation number for the first three lines across different micro/mini-channels

	Line 1	Line 2	Line 3
$D_m = 152 \mu\text{m}$	0.71	0.078	0.008
$D_m = 254 \mu\text{m}$	0.78	0.35	0.13
$D_m = 504 \mu\text{m}$	0.83	0.47	0.39
$D_m = 762 \mu\text{m}$	0.85	0.57	0.52

3.3.4 The Variation of the Vapor Volume Fraction Inside Channels with Different Diameters

Figure 3.17 shows vapor volume fractions along Line 1, Line 2, Line 3, Line 4, and Line 5 across micro-channels and mini-channels. The results demonstrate that the amount of the vapor phase is the highest on the lines 2 and 3 for all the cases, where the cavitation bubbles start to form. It should be noted that vapor phase covers a larger section across the diameter of mini-channels than the micro-channels, while the vapor phase can reach the outlet of the channel at both low and high upstream pressures. Under these conditions, fully developed cavitating flows exist along an important part of the channel. The flow is not able to generate enough bubbles in order to form cavitating flows along the micro-channel. The micro-channel with an inner diameter of 254 μm is more suitable for the applications related to the cavitation generation and collapse of the bubbles, which occurs at

the outlet of the channel, compared to the micro-channel with an inner diameter of $152 \mu\text{m}$. The bubbles could extend to the outlet of the mini-channels, and the vapor volume fraction at the locations corresponding to the lines 2 and 3 is about unity close to the wall, whereas the vapor fraction at the locations corresponding to the lines 4 and 5 is approximately 0.8 close to the wall. These values are high in comparison to the micro-channel results. However, the vapor volume fraction near the symmetry plane of the channel is higher for the micro-channels than mini-channels. These features prove that the cavitation bubbles occupy larger area in micro scale. Further examination of the results shows that the velocity magnitude has the highest value in the micro-channels. Being more pronounced in micro scale, the velocity of the cavitating jet and the interactions between bubbles and liquid considerably influence the effectiveness of cavitating flows on the target located downstream the channel/orifice.

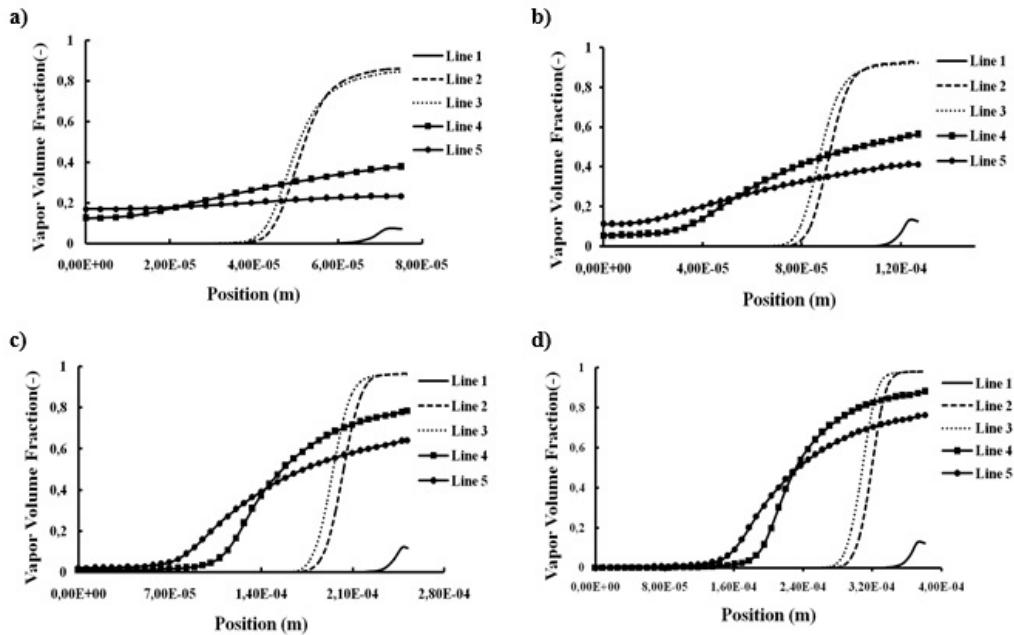


Figure 3.17: Vapor volume fraction for channels with different inner diameters at upstream pressure of (a) $p_i = 10 \text{ bar}$ (b) $p_i = 30 \text{ bar}$ (c) $p_i = 80 \text{ bar}$ (d) $p_i = 150 \text{ bar}$

3.3.5 Numerical Analysis of Bubble Number Density (BND)

In this section, after model validation, the effect of bubble number density (BND), i.e. number of cavitation bubbles per unit volume, on cavitating flows inside a micro-channel with a diameter of $152 \mu\text{m}$ was investigated to compare the results with the

experimental results to see which value of the BND agreed with the experimental results. Then, further analysis on cavitation characteristics was performed based on the chosen BND value. It should be noted that the bubble number density (BND), vapor volume fraction and bubble radius are related to each other with the expression $n = \alpha / (4\pi R_B^3/3)$, where α , and R_B are vapor volume fraction, bubble number density (BND), and bubble radius, respectively.

Model Validation

The computational domain is shown in Figure 3.18. The total number of mesh elements in the computational domain was about 1.5×10^5 , while the normal growth rate of the mesh refinement towards the wall boundaries in the mesh generation process was chosen as 1.1.

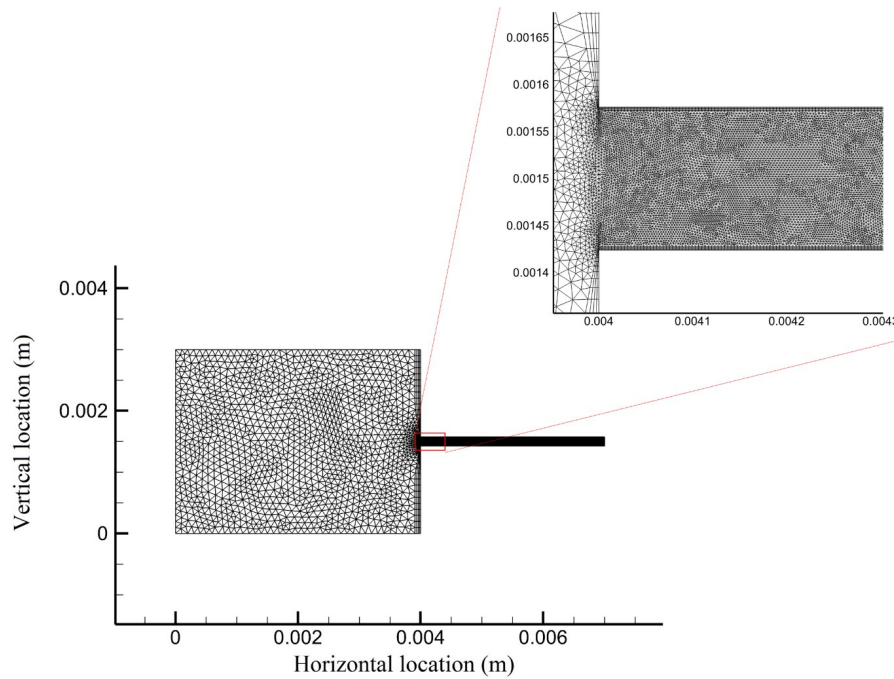


Figure 3.18: Computational domain of the study

The grid independency of the solution was investigated for the case with $p_i = 120$ bar, by increasing the minimum grid size by the factor of 1.2. The maximum changes in the velocity and phase fraction profiles at the exit of the micro-channel were less than 0.7% and 1%, respectively. Furthermore, in order to evaluate the mesh quality, Zeta ($\xi = \frac{\#ofelements}{\#ofnodes}$) parameter is used and the calculated value is obtained as 3.26. Also, the calculated y-plus value (to capture the boundary layer near wall in

turbulent flows, $y^+ = \frac{u_* y}{\nu}$) was 120. The calculated y^+ and Zeta parameters are in good agreement with the available data in the literature [47]. In order to validate the numerical model, calculated results were compared with the available results [64, 145]. As the first validation (Figure 3.19), the obtained discharge coefficients for cavitating flows inside a cylindrical nozzle (injector) are presented as a function of flow Reynolds number (which is a function of upstream pressure as stated in this reference). The discharge coefficient is the ratio of the effective mass flow rate (the mass flux over the orifice exit plane) to the theoretical mass flow rate through the nozzle and is calculated as:

$$C_D = \frac{\dot{m}_{effective}}{\dot{m}_{ideal}} = \frac{\dot{m}_{effective}}{A\sqrt{2\rho_l(p_i - p_o)}} \quad (3.22)$$

Here, A is the orifice cross section and ρ_l is fluid velocity. The Cavitation number considered in this section is equation 1.1 defined in Chapter 1. Accordingly, a good agreement between calculated numerical and experimental results is obtained with a Mean Absolute Error of 2%.

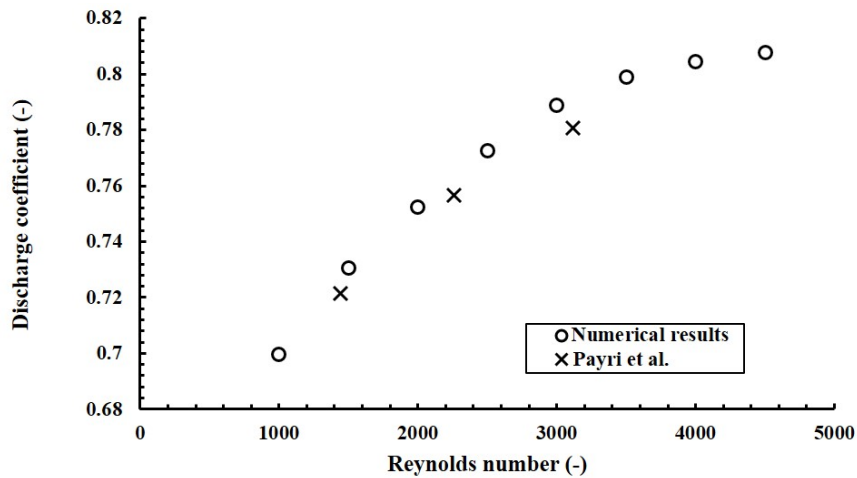


Figure 3.19: Validation of the present numerical model against the results of Payri et al. 2004

Also, the calculated discharge coefficients of the numerical model were compared with the experimental results conducted by Nurick [145]. As seen, a very good agreement is attained for low cavitation numbers, while an acceptable agreement with a Mean Absolute Error of 8% is achieved for higher values of cavitation number (Figure 3.20).

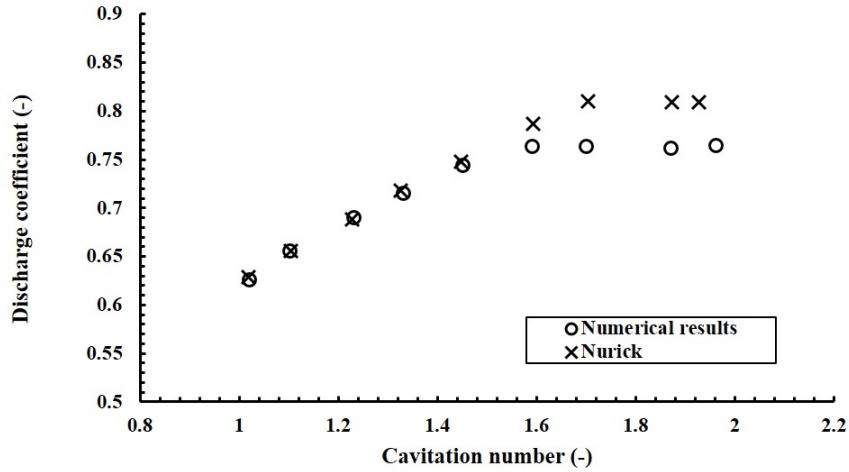


Figure 3.20: Validation of the present numerical model against the results of Nurick 1976

3.3.6 The Effect of Bubble Number Density on Cavitation

In the literature, three different values of bubble number densities (BND) (e.g. 1.0×10^9 , 1.0×10^{12} , 1.0×10^{14}) were considered for cavitation inside a micro-channel [146]. It is obvious that vapor phase increases with number density of bubbles inside the two phase domain and the conditions inside the cavitating flow change with bubble number density. One key parameter that can be considered is the discharge coefficient. The variation of discharge coefficient for three bubble site densities at the upstream pressure of 100 *bar* is shown in Figure 3.21. As can be seen, BND has a considerable effect on discharge coefficient. The variation of the discharge coefficient with respect to time is more pronounced for larger values of BND. The obtained discharge coefficients for cavitation model with 1.0×10^{13} BND also matches with the obtained experimental results.

The total vapor volume fraction inside the domain is more for the higher BND case. To clarify the role of site density on generated vapor volume fraction, the total transferred mass inside the numerical domain is divided by the number of the sites. Figure 3.22 shows the calculated mass transfer rate per bubble site densities for three BNDs of 1.0×10^9 , 1.0×10^{11} and 1.0×10^{13} , at time scales of 1, 10 and 50 μs . Although BND raises the amount of generated vapor mass, the mass transfer rate per bubble site density is much lower for cavitating flows with a higher bubble number density.

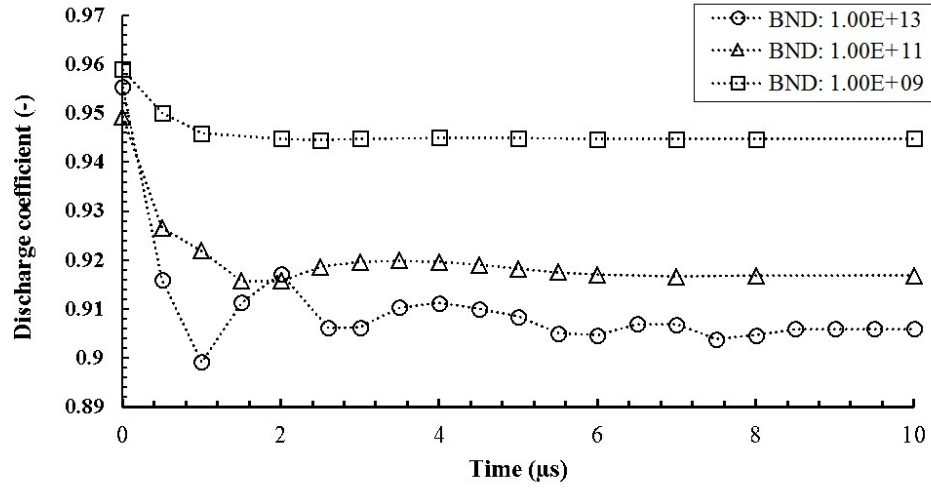


Figure 3.21: Discharge coefficient for three bubble number density (BND) values as a function of time step

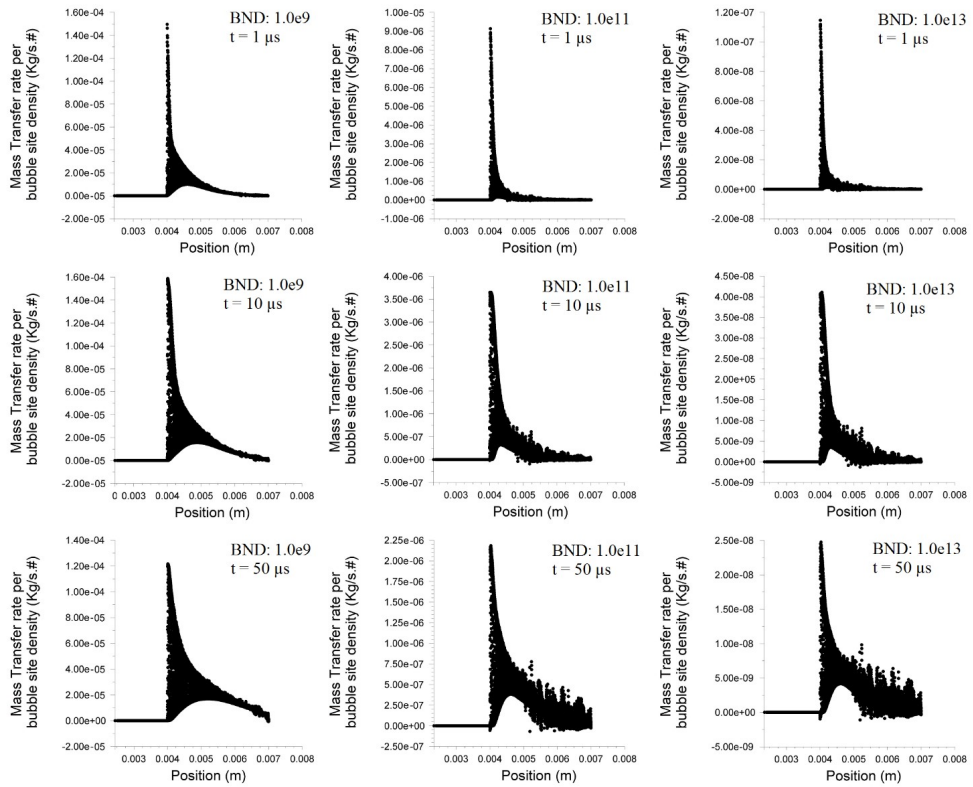


Figure 3.22: Transferred mass per bubble number density (BND) for different time steps

Figure 3.23 shows the vapor volume fraction contours for BND values of 1.0e9, 1.0e11 and 1.0e13 at four time steps at $p_i = 100 \text{ bar}$. As can be seen, bubble number density has a considerable effect on phase distribution inside the two-phase domain. As expected, vapor volume fraction increases with number density, where this effect

is more pronounced at lower BND. Comparing the obtained results of $1.0e11$ with those of $1.0e13$, it can be concluded that the vapor volume fraction values throughout the micro-channel are similar with some variation at the middle and outlet of the micro-channel, which affects the structure of the exiting spray. The obtained results indicate that generated vapor volume fraction increases with BND.

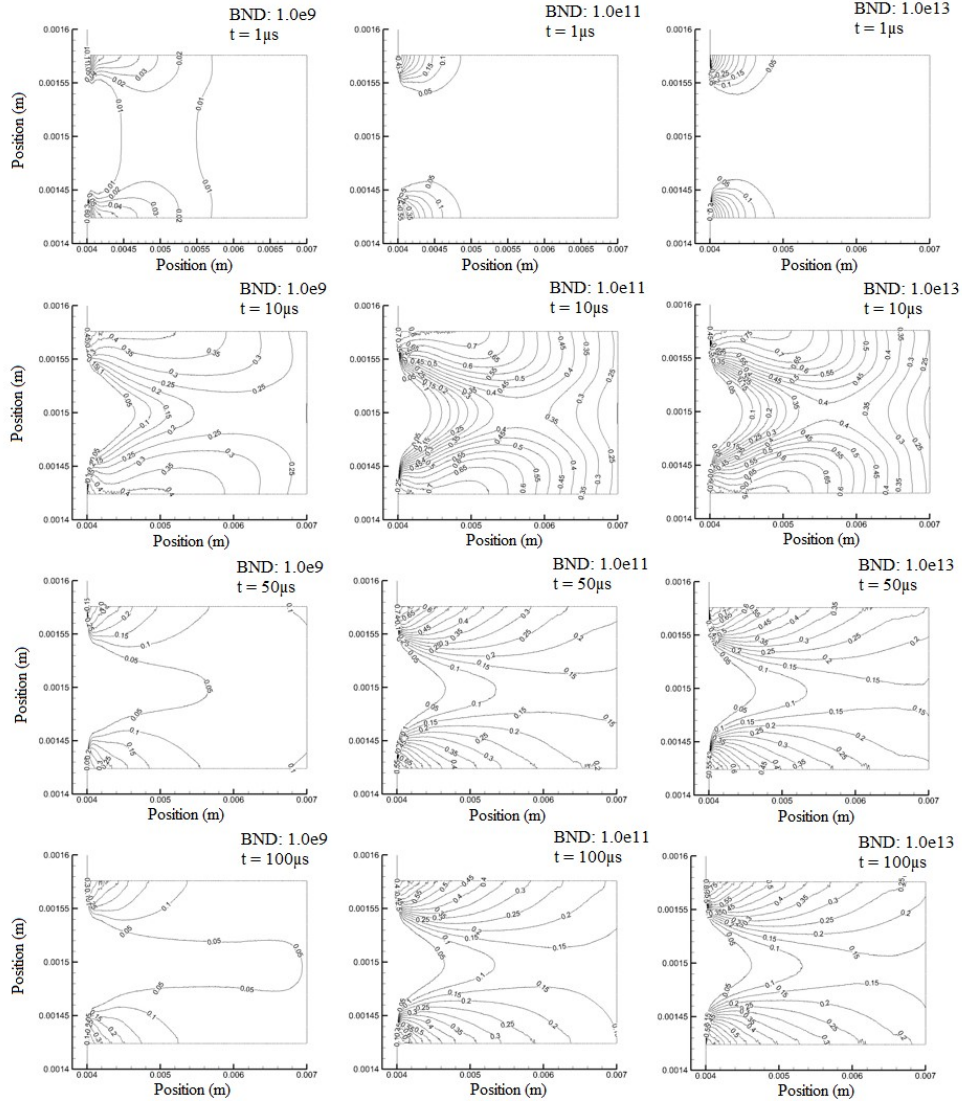


Figure 3.23: Vapor volume fraction contours for bubble number densities (BNDs) of $1.0e9$, $1.0e11$ and $1.0e13$ at different time steps

3.3.7 Hydraulic Characteristics of Cavitating Flows with the Bubble Number Density of $1.0e13$

The presence of vortices in the cavitating flow for BND of $1.0e13$ at the upstream pressure of 100 bar , and magnified orifice area are shown in Figure 3.24. Reentrant

jet motion is shown in Figure 3.24 (a), which results in local recirculation regions as shown in Figure 3.24 (b). During the transient cavitation, multiple vortices form and have interactions within the cavitating flow. The separation and collision of the cavitation induced vortices are shown in Figure 3.24 (b) and Figure 3.24 (c). Furthermore, the flow velocity in the vicinity of the cavitating regions strongly affects the vapor fraction distribution and their expansion, which can be seen in Figure 3.25.

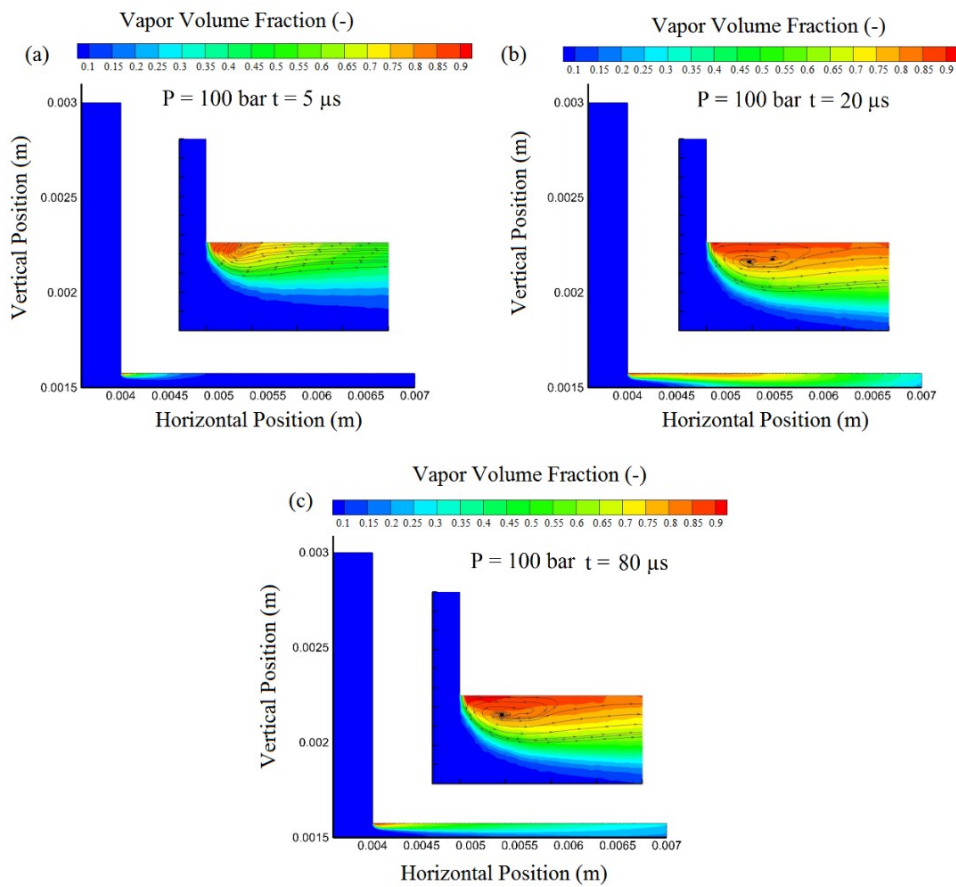


Figure 3.24: Vortices in the cavitating flow for bubble number density (BND) = 1.0×10^{13} at the upstream pressure of 100 bar

Figure 3.25 shows the vapor volume fraction and velocity contours (m/s) at the outlet of the micro-channel for 0, 1, 2 and 3 ms time intervals at three inlet pressures (80, 100 and 120 bar). The obtained results indicate that as the inlet pressure increases, the exit vapor volume fraction variation with respect to time increases. Accordingly, at a higher upstream pressure, vapor phase exists in the micro-channel with higher velocities near the wall boundaries. The time variable

velocity and vapor phase change the exiting spray shape and affect the collapse.

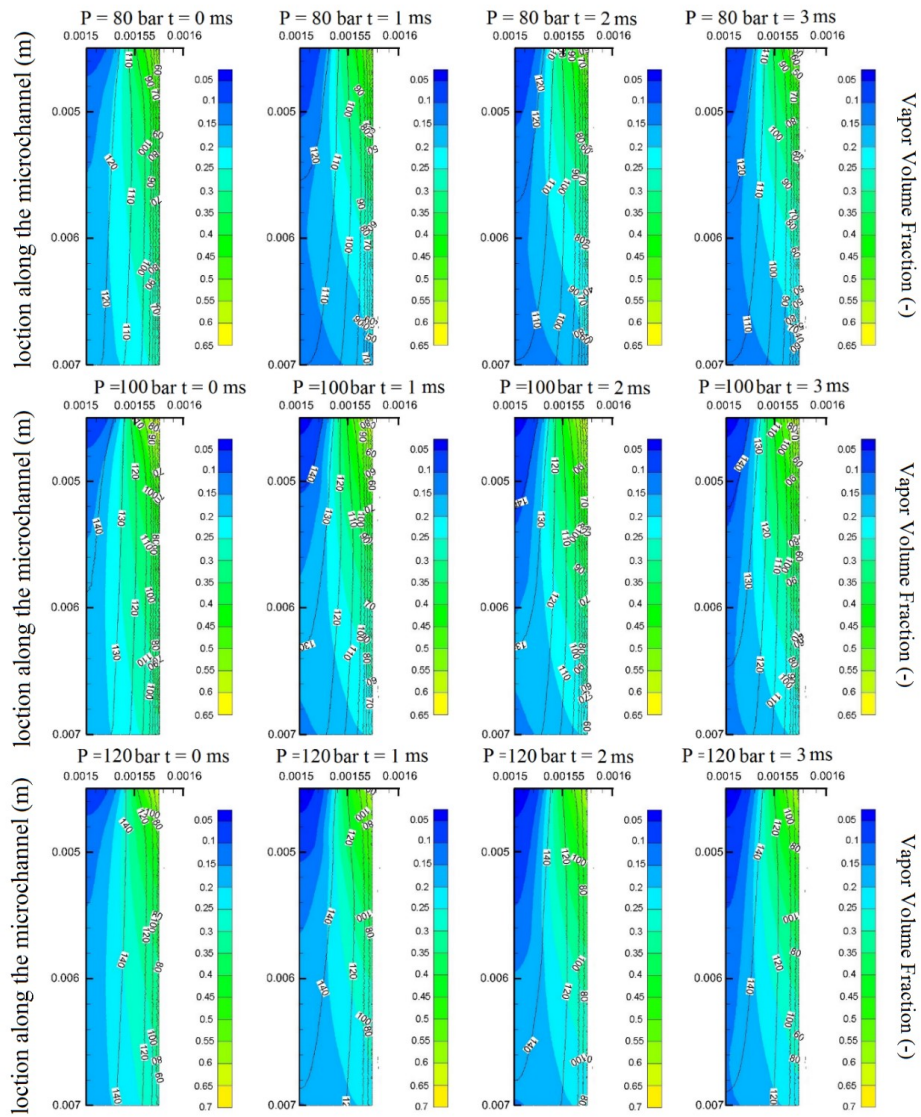


Figure 3.25: Velocity profiles and vapor phase distributions near the outlet of the micro-channel

Chapter 4

Spray at the Outlet of the Micro-Channel under the Effect of the Cavitation Phenomenon

4.1 Introduction

Spray formation downstream of micro flow restrictive elements strongly depends on the flow regimes inside them. Although it is possible to simulate the sprays details including primary and secondary break-ups, spray and break-up visualization are vital and challenging in micro scale studies, where the dimensions are very small, and the process occurs within a very short period of time. Recently, high velocity jets along the spray, bubble evolution, collapse of the bubbles, and droplet segmentation in the spray have become popular due to their exploitation in engineering and biomedical applications. It is crucial to identify the appearance of the spray and to concentrate on the whole shape of the spray in such a way that the spray length and energy released from the collapse of resulting bubbles could be applied on a possible target at the optimum distance for such applications. For this, rigorous studies are necessary to assess flow characteristics downstream of the micro flow restrictive elements, and experimental investigations are required to gain insight into cavitating flow physics with visualization as well as with numerical approaches.

In this chapter, spray formation and atomization, bubble and droplet evolutions, break-up, and corresponding cavitating flows at the outlet of a short micro-channel

with an inner diameter of $152\ \mu\text{m}$ were experimentally studied at different injection pressures with the use of a high speed visualization system. High speed visualization was performed at five different segments to cover a $27.5\ \text{mm}$ distance beginning from the micro-channel outlet (Five segments, at distances of 0-5.5, 5.5-11, 11-16.5, 16.5-22 and 22-27.5 mm from the micro-channel outlet) to assess the spray formation mechanism. It was observed that cavitating bubbly flow was strongly affected by the injection pressure. High speed visualization revealed that droplet evolution is initiated from the second segment at low upstream pressures (5-30 bar), whereas droplets are discretized from the liquid jet in the fourth and fifth segments at medium and high upstream pressures (40-100 bar). Bigger size droplets formed at the outlet up to an injection pressure of 40 bar , while cavitation effect of intensified cavitating flows became dominant beyond this injection pressure, leading to smaller droplet sizes and a more conical spray. Image based analysis of bubbly cavitating flows revealed that the more pressure drop occurred along the micro-channel, the smaller droplet formation was evident. The droplet/bubble evolution can be exploited in biomedical and engineering applications, where destructive effects of bubbly cavitating flows are needed. Furthermore, classification of fluid flow regimes and morphological characteristics of the spray structure were outlined based on the Cavitation number.

4.2 Experimental Procedure and Setup

Experiments were conducted by applying different inlet pressures. Inlet pressures were varied from 5 to 100 bar , while outlet pressure at the micro-channel was fixed to 1 atm . Volumetric flow rate was increased with the change in the inlet pressure. At a certain pressure level, cavitation incepted, which was recorded using the high speed camera. Cavitating flow generated in micro-channel was recorded at different regions (five segments, at distances of 0-5.5, 5.5-11, 11-16.5, 16.5-22 and 22-27.5 mm from the micro-channel outlet) downstream the micro-channel outlet. The liquid jet, break up mechanism, spray cloud, bubble emergence at the exit of the micro-channel, and spray formation was captured by the camera and images were processed using the Active Contour Method. The experiments were repeated for several times

at different pressures to ensure repeatability.

The proposed experimental setup consists of two main sections: 1) Hydrodynamic cavitation setup, which is used to generate cavitating micro bubbles emerging from a micro-probe, and 2) high speed imaging setup, which is used to visualize the bubbles emerging from short micro-channel (micro-probe) at different distances and to characterize the bubble size, shape and cone angle of the resulting jet.

4.2.1 Hydrodynamic Cavitation

A schematic of the experimental setup is shown in Figure 4.1. The experimental setup consists of a high pressure pure nitrogen tank (Linde Gas, Gebze, Kocaeli), a liquid container (Swagelok, Erbusco BS, Italy), pressure sensors (Omega, USA.), fine control valves (Swagelok) at different locations, a micro-filter (Swagelok), a turbinemeter (Omega, USA), a Phantom high speed camera (Phantom V320 high speed camera) with appropriate lenses, a workstation with visualization software (Phantom PCC 2.0 software), fittings (Swagelok), and a short micro-channel (Small Parts, USA.), which serves for generation of cavitation and is connected to the setup with appropriate fittings.

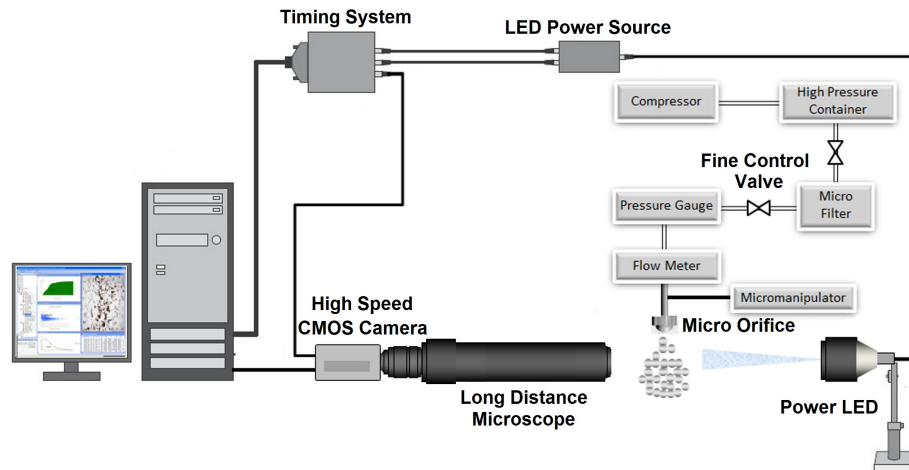


Figure 4.1: Experimental setup with the orifice throat and exit area

The tank was used as a container for de ionized water and high pressure nitrogen tank was connected to the liquid container in order to maintain high input pressure and to propel the working fluid to the micro-probe. The micro-filter was employed to prevent the flow of any particles larger than 0.015 mm to the system. Pressure

sensors were located at several parts of the experimental setup to measure the pressure. The experimental setup was equipped with several valves to start/stop the flow. During the experiments, valves were fully opened and cavitation is generated with sudden pressure drop across a 4.5 *mm* short micro-channel with an inner diameter of 152 μm . At the outlet, micro-channel at the tip was kept as short as possible to visualize bubbly cavitating flows downstream the outlet. The experimental setup was prepared in parallel lines with to the set-up used in the study of [18], with the addition of piping extensions allowing the adjustment of the probe-to-specimen distance and integration of a high speed imaging setup and a micro-manipulator. The uncertainties in experimental parameters are given in Table 4.1. They were provided by the manufacturer’s specification sheets or were obtained using the propagation of uncertainty method presented in Kline and McClintock study ([147]).

Table 4.1: Uncertainties in experimental parameters

Uncertainty parameter	Error
Cavitation number, σ	$\pm 6.7\%$
Flow rate	$\pm 1.4\%$
Inner diameter, D_i	$\pm 0.002\text{mm}$
Outer diameter, D_o	$\pm 0.001\text{mm}$
Pressure drop, Δp	$\pm 0.3\%$

4.2.2 High Speed Imaging System

The images of cavitating flows were collected by a double shutter CMOS camera (Phantom v310, a trademark of Vision RESEARCH) which allowed two successive images to be acquired with a resolution of 1280 by 800 *pixel* (0.02 *mm* pixel size) within a very short time delay. CMOS camera was equipped with a macro camera lens (type K2 DistaMax with focal length: $f_l = 50\text{ mm}$ and f-number: $f = 1.2$) and was mounted at a distance of 342 *mm* from the imaging plane, yielding a magnification of $M = 0.137$. This optical arrangement ensured that only the central region of the lens was used where aberration can be neglected. The images were exposed in a background illumination mode using a pulsed LED array consisting of 551 high performance LEDs with a total area of 160 *mm* \times 100 *mm*. In front of the LED array, an opaque plate was installed in order to produce diffuse illumination.

The typical duration of the light pulses was 0.05 to 0.07 *ms*, while the time delay between the two successive images was adjusted to the local flow velocity in a range from 1 to 3 *ms*.

4.3 Results and Discussion

4.3.1 Spray Characteristics under the Effect of the Cavitation Phenomenon

The flow rate profile is shown as a function of the inlet pressure in Figure 4.2. The flow rates in this study match well with those of previous studies under similar experimental conditions [17–20]. The pressure head loss of the flow is manifested in terms of turbulent fluctuations, which mitigate bubble growth and collapse. The flow modeled inside a micro-channel with the diameter of 152 μm in our previous work, demonstrates that the Reynolds number of the cavitating flow along the micro-channel is between 4,534 and 77,041 presenting turbulence inside the micro-channel for all the cases. The bubble/bubble and bubble/flow interactions also contribute to this phenomenon. Under a certain combination of operating parameters, the flow may actually flash. At higher upstream pressures, where the intensity of the cavitation bubbles is considerable, the cavitating flow experiences flashing, which affect the discharge coefficient especially at upstream pressures higher than 80 *bar*. Furthermore, very low Cavitation numbers in these pressures lead to the cavitating flows to produce bright sparks and increase the discharge coefficient to some extent. Moreover, in the case of excess of the dissolved gas content, flashing is also expected to occur. Another important factor is the vapor pressure of the liquid. Transport of solvent vapor across the bubble interface during the radial motion of bubbles and its entrapment during collapse also affect the intensity of collapse and the spray formation.

During the experiments, it was observed that cavitation incepted at a pressure of 10 *bar*. This corresponds to a Cavitation number of 1.37, which is lower than inception Cavitation numbers in the literature for conventional scale. However, it is in agreement with micro scale cavitation studies [17–20], which suggests a major difference between conventional scale and micro scale cavitation. Beyond this

Cavitation number, more distinct bubbles and droplets and spray formation are present.

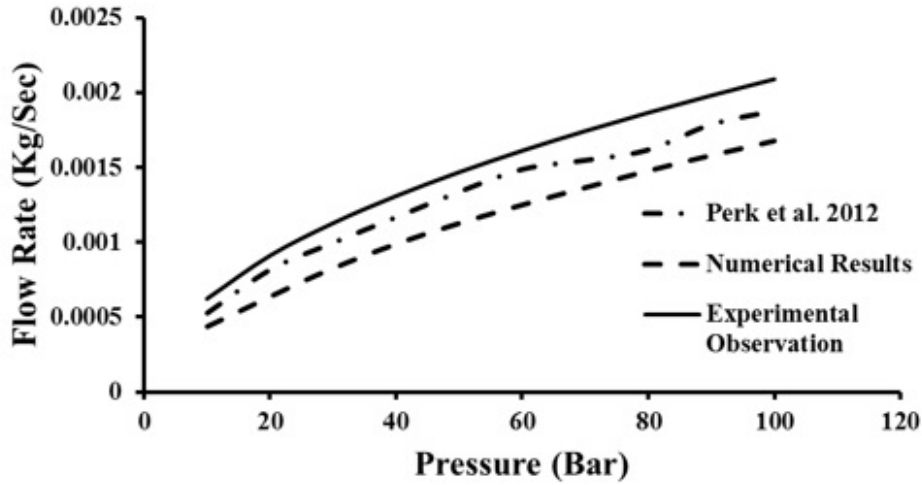


Figure 4.2: The variation of the flow rate with respect to the upstream pressure

The spray formation at different injection pressures is recorded during the experiments. As a result of a contraction in micro-channel cross-sectional area, different flow regimes can be seen at different injection pressures. It was observed that, the spray does not have a conical shape at the pressure of 5 *bar*, and the flow looks like a jet flow with a constant cross-sectional area at the outlet of the micro-channel. However, the spray starts to become conical at the pressure of 20 *bar*. The change in cone angle of the spray visualized from the pressure of 20 to the pressure of 50 *bar*, and a denser cavitation cloud is apparent with pressure. The spray shape in these figures shows intensified cavitating jet effects. Accordingly, as the upstream pressure is increased, the spray shape shows a more cavitating jet profile with increased cone angle, and the impact of the spray on a targeted area would also have a more destructive effect. The length of the cavitation cloud of the cavitation bubbles also increases with pressure. More cavitation bubbles could extend to the end of the micro-channel and the collapse of more bubbles occurs downstream. The variation in Cavitation number is shown in Figure 4.3, which presents the effect of the upstream pressure on the generation of the cavitation bubbles. Cavitation number at a lower injection pressure starts from 1.37 and decreases down to 0.1108 at $p_i=100$ *bar*. The intensity of the cavitating jet increases with decreasing Cavitation number. The Cavitation number indicated in Figure 4.3 illustrates that there is almost no

visible cavitation bubbles at the tip of the micro-channel at a very low upstream pressure, and numerical results in our previous study that the cavitation bubbles do not extend to the end of the micro-channel. As the upstream pressure increases, the Cavitation number dramatically decreases up to a very low number at the upstream pressure of 100 *bar*. Our results apparently shows that the cavitation bubbles fill the entire micro-channel and significant space in the micro-channel is filled with the vapor phase. Therefore, as it is expected, vaporous flow conditions are present at the end of the micro-channel at higher upstream pressures. Moreover, the experimental visualization for low and high upstream pressures demonstrates that the fluid flow regime at low upstream pressures is laminar with a small amount of tiny vapor bubbles, however the spray formed at the outlet of the micro-channel at high pressures is highly vaporous such that the generated bubbles inside the micro-channel due to the aggregation of the bubbles and also intensity of the fluid flow exit to the outlet and constitute a mixed vaporous region around the tip of the micro-channel.

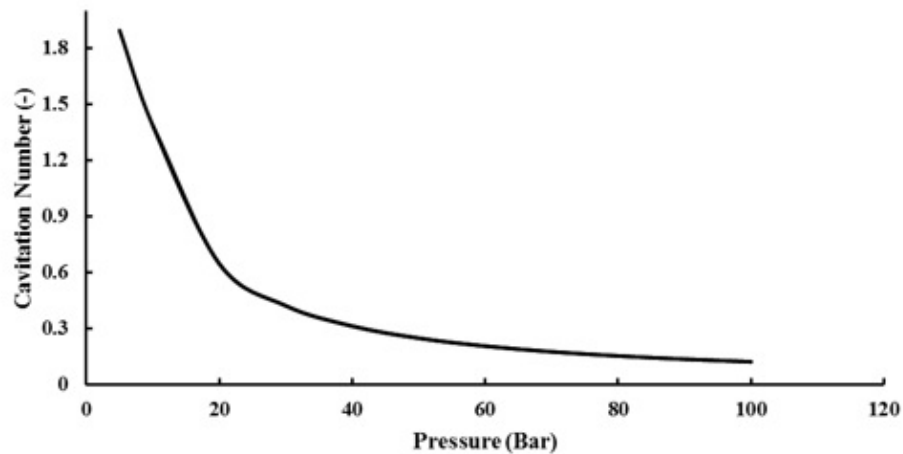


Figure 4.3: The variation of the Cavitation number with respect to upstream cavitation

The spray cloud diameter is shown in Figure 4.4 as a function of the upstream pressure for different segments. As can be seen from this figure, at low pressures, spray diameter can be measured even 15 mm downstream the micro-channel outlet. The collapse pressure of the individual bubbles is considered as a significant parameter in increasing the cloud diameter. The collapse pressure is more appreciable at higher upstream pressures, where the cloud diameter is large compared to the lower injection pressures. The dissolved gas content of the liquid is also another important

parameter especially at lower upstream pressures affecting the cloud diameter of the spray. Dissolved gases excite the spray structure due to the cavitation inception and make the spray cloud diameter larger. Moreover, the interaction among bubbles has a significant impact on the fluid flow regime inside the micro-channel and thus on the spray formation at the outlet of the micro-channel, which considerably affects the spray diameter. It can be observed that the spray diameter increases beyond a certain pressure value for all the segments and covers a wide distance, which is much larger than the micro-channel dimensions.

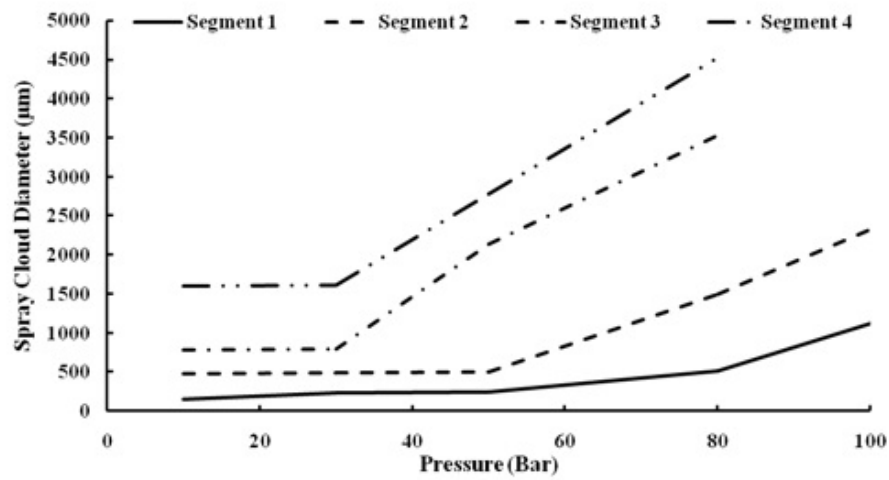


Figure 4.4: Spray cloud diameter at different segments for various upstream pressures

4.3.2 Structure of the Spray for Various Pressures at Different Segments

The structure of the liquid jet spray in five different segments are visualized and studied in this section. These five consecutive segments start exactly at the exit of the jet nozzle and are examined at 11 different inlet imposed pressures, which are 5, 10, 20, 30 up to 100 *bar* with increments of 10 *bar* between each two of the rest.

Moholkar et al. [148] and Kumar et al. [149] mathematically modeled a single bubble to investigate its motion under turbulence and non-turbulence conditions. They used several parameters to change the turbulence intensity such as the pressure recovery (which is dependent on the exit pressure), pipe diameter downstream of the orifice, pipe to orifice diameter ratio and initial bubble diameter. Both studies were based on the continuum mixture model proposed by Van Wijngaarden [150], where it was coupled with a diffusion model. In the first study, Rayleigh-Plesset [151] diffusion model was implemented, while the set of equations proposed by Toegel et al. [152] were utilized in the second one. In the first study, they concluded that as the pressure recovery increased, the maximum cavity size before its collapse as well as the lifetime of the bubble increased. This conclusion was depicted in our results at higher upstream pressures, where cavitation bubbles extend to the outlet of the micro-channel and tolerate the atmospheric pressure downstream the micro-channel. Also, their conclusion, which showed an increase in the maximum cavity radius in the case of bigger pipe, can also be drawn for a micro-channel with a bigger inlet diameter. The main reason for such a change was reported to be the increased scale of the turbulence, which reduces its frequency and therefore allows the cavity to grow more.

It is observed in our experimental tests that the elongation of the bubble lifetime dramatically increases when the fluid flow is passed from smaller constrictions, and Moholkar et al. [148] proved that an increase in the pipe to orifice diameter ratio results in an elongation of the bubble lifetime. They also reported that as the initial bubble diameter (R_{in}) reduces, the R/R_{in} ratio increases, where R is the instantaneous radius of the bubble.

Kumar et al. [149] conducted a similar study and discussed the results using four different categories for the bubble motion, which are flashing, moderately transient,

strongly transient and oscillatory. They also mentioned that in the case of a Cavitation number equal to unity, as the pressure recovery increased, the droplets motion intensified. This behavior can also be observed in the cloud diameter variation and in lower segments of the spray with low upstream pressures presented in Figure 4.5. The spray cone angle and cloud diameter increase beyond a certain pressure indicating an increase in the intensity of the spray structure particularly in the lower segments. The discretized bubbles in the segments 3, 4 and 5 have more oscillating feature at higher upstream pressures (Figure 4.7), and higher pressure recovery at low Cavitation numbers and high pressures generate fluctuating droplets and bubbles and hence a wider spray with bigger cone angle and spray cloud diameter.

As can be seen in Figure 4.5 to Figure 4.7, which display the five segments of each one of the imposed 11 conditions, the flow seems to be fully continuous in the first segment. However, as the imposed pressure increases, the water jet splashes more vigorously when exiting the flow restrictive element. This is due to the higher amount of energy, which appears in terms of higher velocity. The fluid flow at the outlet of the micro-channel at 5 *bar* does not have any conical shape, where the Cavitation number is 1.85. At the first segment, the flow has a constant velocity of 14.86 *m/s*. However, droplet evolution is observed at the second segment at a distance of 8.4 *mm* from the micro-channel tip. The droplets are separated from the fluid flow at the third segment, and the smallest droplets have a length of 0.114 *mm* at an upstream pressure of 10 *bar*. The droplets are dispersed for a wider range at the fourth segment, and the population of the droplets is increased. Although the spray forms a conical shape between 30 and 50 *bar*, the generated cavitation bubbles inside the micro-channel do not dramatically induce intensified spray formation. The velocity of the spray is increased to 64.84 and 84.44 *m/s* at 30 and 50 *bar*, respectively. The droplets become denser at 50 *bar*, and the minimum lengths of the droplets are 0.096 and 0.065 *mm* for 30 and 50 *bar*, respectively. The droplets become thinner at higher upstream pressures and surface tension is more dominant in the formation of the droplets.

In the second segment, first points of discontinuity in the liquid jet can be observed. Even in the first case when the imposed pressure is only 5 *bar*, it can be seen that the jet is not continuous anymore. As mentioned before, an increase in

the inlet pressure beside the nonlinear behavior of the flow in the vicinity of the evolution change the structure of the exiting fluid flow. Perturbations existed in the long liquid jet induce the droplets to get minimum surface area and thus surface tension as an important source of instability plays significant role in the formation of the droplets. It is clearly observable that the number of splashed droplets increases when the inlet pressure increases. The third segment continues showing this pattern more obviously. The number of flow discontinuities increases compared to the previous section, the jet is more deviated in some instances from its original path. This pattern continues to flourish even more in the following fourth and fifth segments. For example, it can be observed that at the imposed pressure of 5 *bar*, the flow is completely separated into droplets in the fourth and fifth section. Increasing the pressure would increase the droplet population in these areas, which become more and more scattered, while the pressure is increased. Another important observation is related to the cone angle of the exiting flow jet in this spray structure. It can be seen that while the pressure is maintained at 5 *bar*, the emerging jet exits the channel uniformly. However, as the pressure increases, the jet starts to exit the nozzle in a way that the both sides of the out coming jet seem to form an angle, which is regarded as the cone angle.

The cavitation cloud and jet cavitation are presented for upstream pressures of 80 to 100 *bar* in Figure 4.7. The jet velocities for the first segment are 99.42 and 111.46 *m/s* for 80 and 100 *bar*, respectively. More bubbles exit from the micro-channel as shown in Figure 4.7, and an intensified bubble cloud emerges even at the first segment at the upstream pressure of 80 *bar*. The spray cone angle increases from 80 to 100 *bar*, where more cavitation bubbles exit the outlet of the micro-channel. The spray has a wider form in the second segments at these pressures, and the bubbles occupy a larger space with upstream pressure.

The separation of the droplet break-up from the jet capillary was studied in a broad range in this study. The transition from the liquid jet to the separated droplets is a very complicated task, and most of the studies in this topic are performed in the macro scale and are rather numerical and theoretical. The experimental studies in the micro scale such as the study of Xing et al. [153] on a jet flow with a diameter of 20 μm reported non-dimensional Ohnesorge number ($Oh = \mu/\sqrt{\rho}$, where μ is the

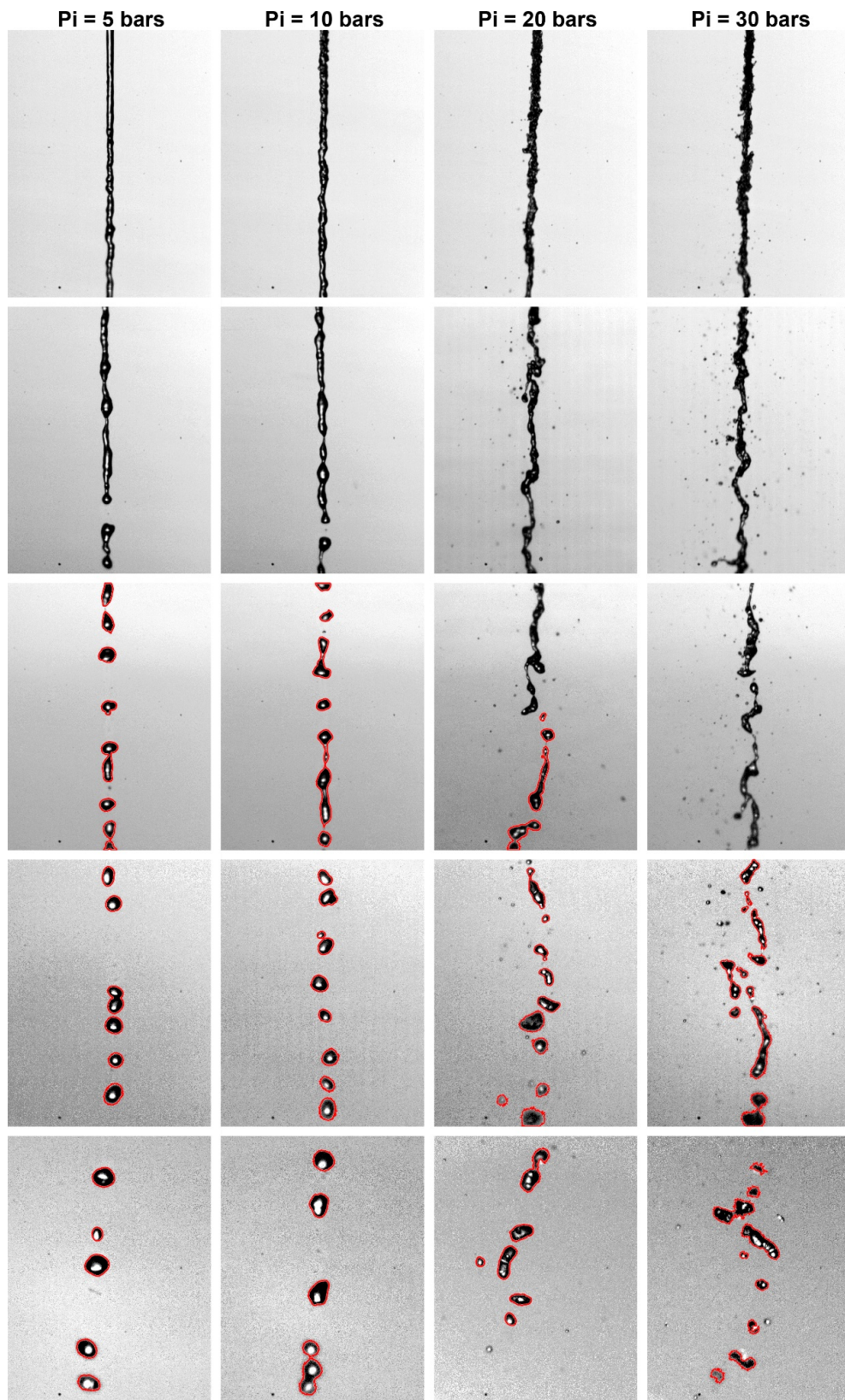


Figure 4.5: Detection of bubble/droplet contours under low inlet pressures

viscosity, ρ is density and R is the droplet/bubble radius) of 0.24 for the initial separation and Wave number of 0.64, while the Ohnesorge number is our study is

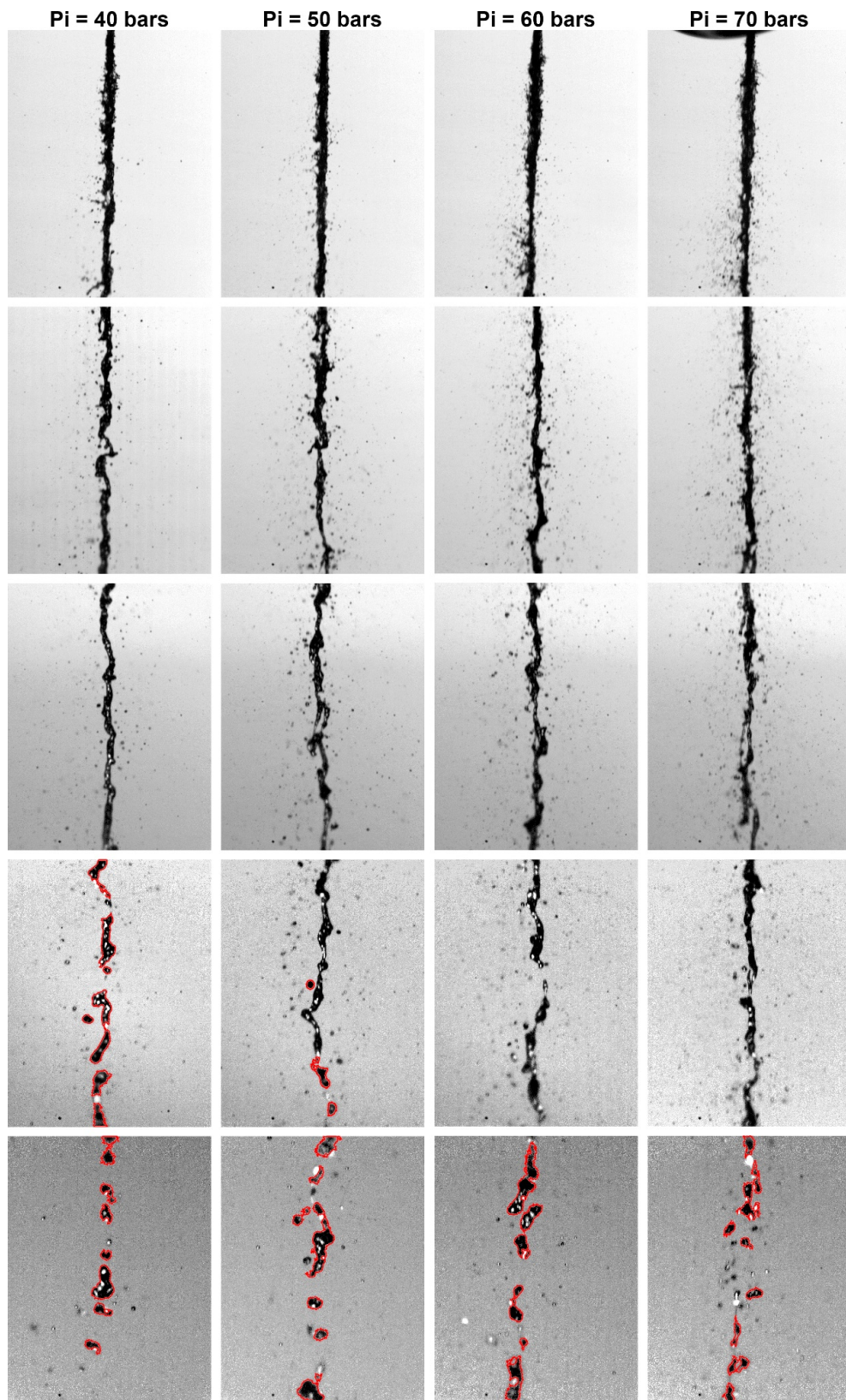


Figure 4.6: Detection of bubble/droplet contours under medium inlet pressures

0.013. The Ohnesorge number extracted from a linear analysis [154] for a mini-jet flow with a radius of 1 *mm* was reported as approximately 1 where deformation of

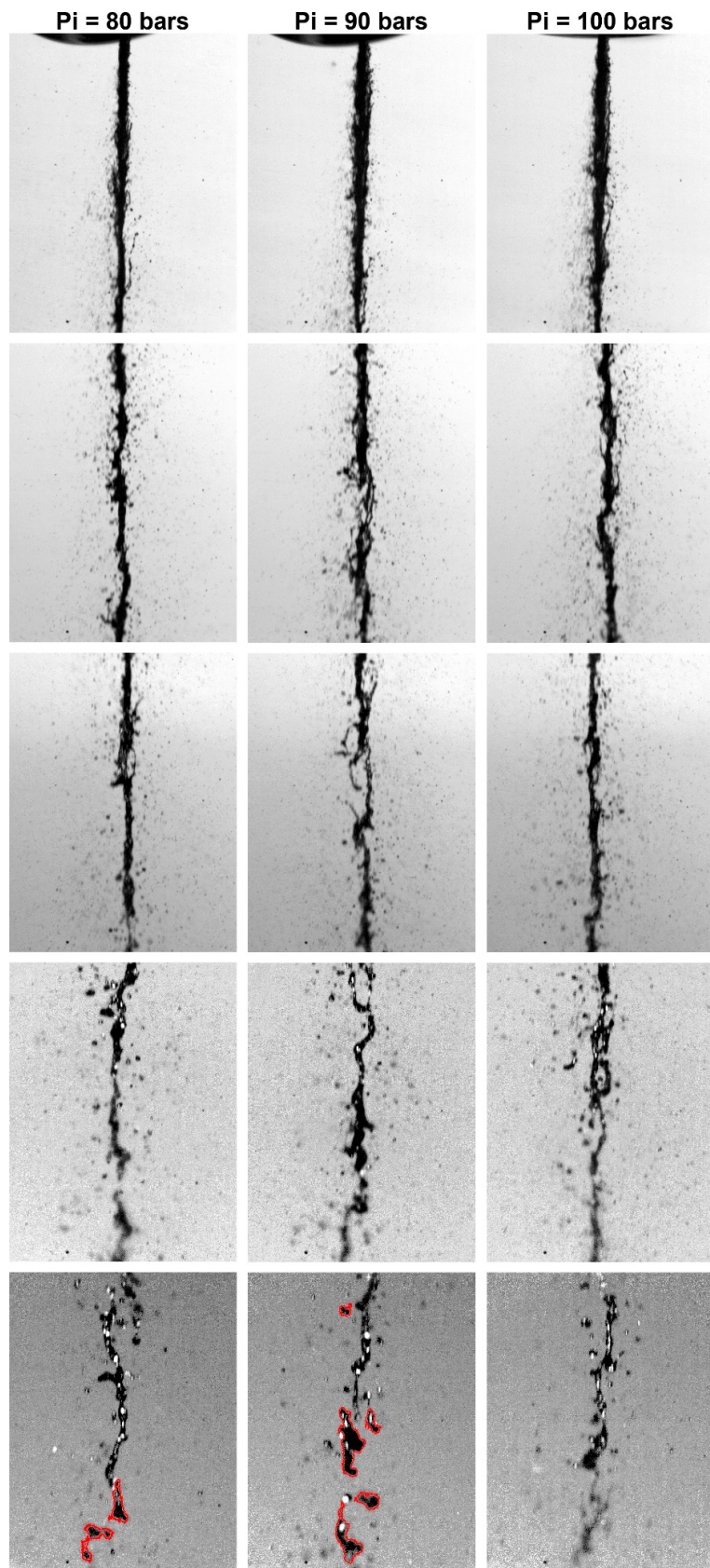


Figure 4.7: Detection of bubble/droplet contours under high inlet pressures

the separated droplets was presented as the initial condition. Saroka et al. [155] in a computational nonlinear three-dimensional study showed a slow growth of the droplets. The maximum Reynolds number was 100 and the reported Ohnesorge number was 0.1, while the minimum Reynolds number in our work is 4,534. There are some other studies related to the initiation of the droplet separation in both micro and macro scales, which illustrate the dominant effect of the surface tension and viscous force. The study of Suryo et al. [156] suggested a vast range for Ohnesorge number from 0.01 to 1, where the initial condition of the deformation was determined from a nonlinear three-dimensional computational investigation. Most of studies in this field considered the instability behavior of the jet flow from a numerical point of view, and the detailed characteristics of the discretized droplets such as their shape, size and eccentricity still need to be addressed experimentally in order to utilize the droplets/bubbles collapse and collision in an efficient way.

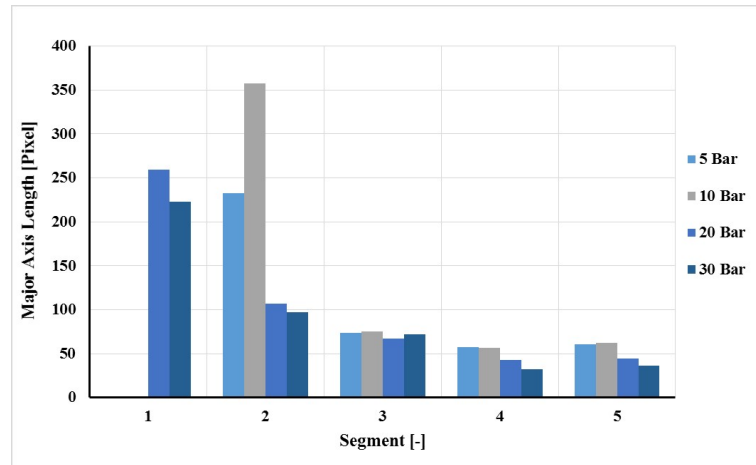


Figure 4.8: Droplet size distribution at different segments of the liquid jet processed using active contour method for mean major axis length

Elliptical axes lengths of the segmented droplets are shown in Figure 4.8 and Figure 4.9. It is observed that for each pressure level, the mean of the major axis lengths decreases from the initial segment to the final segment, whereas the mean of the minor axis lengths increases. Since splitting from the main jet starts in initial segments, separated droplets tend to have elongated shapes initially. For example, when the pressure is 5 *bar*, the ratio of the mean major and minor axes lengths is around 8.5 in the second segment, which corresponds to almost a vertical line segment that can be verified from the mean eccentricity value (0.9) given in the

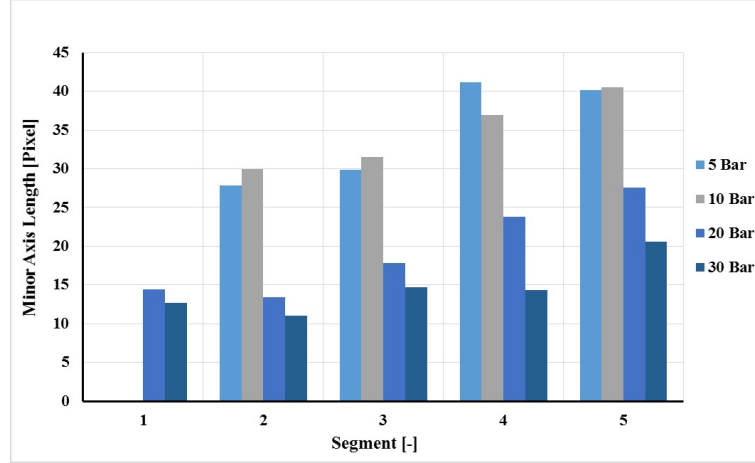


Figure 4.9: Droplet size distribution at different segments of the liquid jet processed using active contour method for mean minor axis length

third column of the Table 4.2. The instability of liquid to breakup into droplets is associated with the Plateau-Rayleigh instability. The liquid column at the outlet of the micro-channel breaks to droplets as a result of the perturbations and the effect of the surface tension, and the separated droplets tend to form a geometry at the minimal energy condition. As shown in Figure 4.8, the major axis length at the first segment for different upstream pressure cases has higher value, which indicates the separation of the mother droplets. These droplets at the second segments have higher standard deviations since the size of the droplets differs dramatically and the generation of the daughter droplets from the mother droplets does not occur. By falling down to the lower segments and creation of the tiny droplets from the bigger droplets, the major axis length decreases significantly, and moreover, the standard deviation values decrease since the generated droplets have approximately the same sizes (Table 4.2). The eccentricity value for different segments presented at Table 4.2 indicates a more vertical column in most of the cases. This fact reveals that the variation in the minor axis length would not be very critical. As illustrated in Figure 4.9, though the minor axis length increases while the liquid jet flows downstream for all the cases, the variations are not high compared to the major axis length. Therefore, the standard deviation gathered in Table 4.2 for the minor axis length only slightly differs for different cases.

Likewise, area and circumference of the segmented droplets are tabulated in Table 4.3, where horizontal position and orientation of the segmented droplets are also

Table 4.2: Standard deviation and eccentricity of the processed droplets using active contour method at different segments for various upstream pressures

Inlet Pressure <i>bar</i>	Segment	Standard Deviation for Major Axis Length [<i>pixel</i>]	Standard Deviation for Minor Axis Length [<i>pixel</i>]	Eccentricity [0-1]	
				Mean	Std. Dev.
5 bar	Seg. 1	-	-	-	-
	Seg. 2	248.1	10.0	0.9	0.2
	Seg. 3	73.0	12.1	0.8	0.2
	Seg. 4	24.8	13.9	0.6	0.2
	Seg. 5	26.6	16.3	0.7	0.2
10 bar	Seg. 1	-	-	-	-
	Seg. 2	316.0	8.2	0.9	0.1
	Seg. 3	71.0	12.0	0.8	0.2
	Seg. 4	25	12.8	0.7	0.2
	Seg. 5	26.8	16.0	0.7	0.2
20 bar	Seg. 1	406.3	15.4	0.7	0.2
	Seg. 2	258.9	17.4	0.7	0.2
	Seg. 3	126.9	18.0	0.7	0.2
	Seg. 4	40.6	16.7	0.7	0.2
	Seg. 5	30.8	17.5	0.7	0.2
30 bar	Seg. 1	386.3	14.7	0.8	0.2
	Seg. 2	257.1	14.9	0.7	0.2
	Seg. 3	161.6	17.3	0.8	0.2
	Seg. 4	52.0	14.4	0.8	0.2
	Seg. 5	34.9	17.1	0.8	0.1

provided to locate the droplets with respect to the main jet. Mean of the area values shows that in downward segments, droplets get much smaller, and increasing pressure level results in more separated droplets. Standard deviations of the horizontal positions of the segmented droplets show that scattering from the main jet increases with subsequent segments and increasing pressure levels. It should also be noted that while the orientations of the droplets at lower pressure values are close to 90 degree (almost vertical), they are more tilted with increasing pressure values. The discretized droplets/bubbles in the segments 3, 4 and 5 have a more oscillating feature at higher upstream pressures according to the data presented in Table 4.3, and higher pressure recovery at low Cavitation numbers and high pressures generate fluctuating droplets and bubbles and hence a wider spray with bigger cone angle and spray cloud diameter. The small variations in the orientation values indicate that the separated droplets from the liquid jet have slight oscillations, and rotation along the flow direction has only a minimal effect on the dramatic change of the major axis length.

Table 4.3: Droplet characteristics processed using active contour method at different segments for various upstream pressures

Inlet Pressure <i>bar</i>	Segment	Area [<i>pixel</i>]		Circumference [<i>pixel</i>]		Horizontal Position [<i>pixel</i>]		Orientation [0-180 degree]	
		Mean	St. Dev.	Mean	St. Dev.	Mean	St. Dev.	Mean	St. Dev.
5 <i>bar</i>	Seg. 1	-	-	-	-	-	-	-	-
	Seg. 2	4406.1	4463.0	454.2	447.4	297.9	4.1	88.3	38.4
	Seg. 3	1673.6	1463.8	174.4	138.6	302.0	15.8	89.0	51.7
	Seg. 4	1972.8	1136.1	164.1	66.5	314.8	30.2	96.2	51.4
	Seg. 5	1933.4	1312.0	180.6	80.8	272.8	26.2	95.0	54.6
10 <i>bar</i>	Seg. 1	-	-	-	-	-	-	-	-
	Seg. 2	6883.8	5894.4	682.5	572.5	305.2	4.8	92.4	31.7
	Seg. 3	1763.7	1451.9	180.1	136.6	309.5	8.3	95.3	51.1
	Seg. 4	1716.0	945.7	159.8	65.0	311.9	10.8	93.7	52.8
	Seg. 5	1988.4	1254.6	184.8	81.5	284.6	25.3	92.9	54.9
20 <i>bar</i>	Seg. 1	5729.3	9188.5	556.0	869.7	279.3	34.8	93.3	52.1
	Seg. 2	2012.2	5159.9	232.1	554.5	278.9	60.5	96.4	60.0
	Seg. 3	1270.6	2503.7	153.3	269.8	282.2	74.7	100.7	53.4
	Seg. 4	1007.7	3139.2	123.3	156.0	306.3	79.9	101.3	54.8
	Seg. 5	1115.4	1180.6	137.6	98.5	270.7	77.5	108.4	56.0
30 <i>bar</i>	Seg. 1	4965.7	8866.0	487.3	844.2	276.0	30.4	89.4	54.1
	Seg. 2	1819.2	5165.1	217.6	570.8	258.6	54.3	93.1	62.5
	Seg. 3	1229.1	3012.0	165.2	356.3	282.0	68.0	103.4	57.2
	Seg. 4	560.4	1198.8	88.3	134.4	246.5	126.1	96.0	53.1
	Seg. 5	788.9	2466.8	117.0	137.9	289.1	100.1	103.9	55.9

4.3.3 A Correlation; Pressure Drop in the Presence of Cavitation Phenomenon

Pressure drop for single phase flows through a sudden contraction is characterized by a non-dimensional parameter defined as:

$$K = \frac{2\Delta p}{\rho \bar{V}^2} \quad (4.1)$$

Here, \bar{V} is the average velocity in the micro-channel. The dimensionless pressure drop (K) for liquid flow is generally a function of orifice geometric characteristics such as thickness ratio (l/D_m) and diameter ratio (D_m/D), and flow Reynolds number (Re). It was shown that for low diameter ratios ($D_m/D < 0.2$), its influence on non-dimensional pressure drop number vanishes [14], and it can be expressed as $K = K(Re, l/D)$. Cioncolini et al. [14] proposed the following simple correlation for the non-dimensional pressure drop (K) for $10^3 < Re < 2.5 \times 10^4$:

$$K = 3.137Re^{-0.0737} \quad (4.2)$$

A comparison between the single-phase experimental results (low Reynolds num-

ber data) and the correlation is shown in Figure 4.10. As seen, the single-phase experimental results match well with the predictions of the correlation.

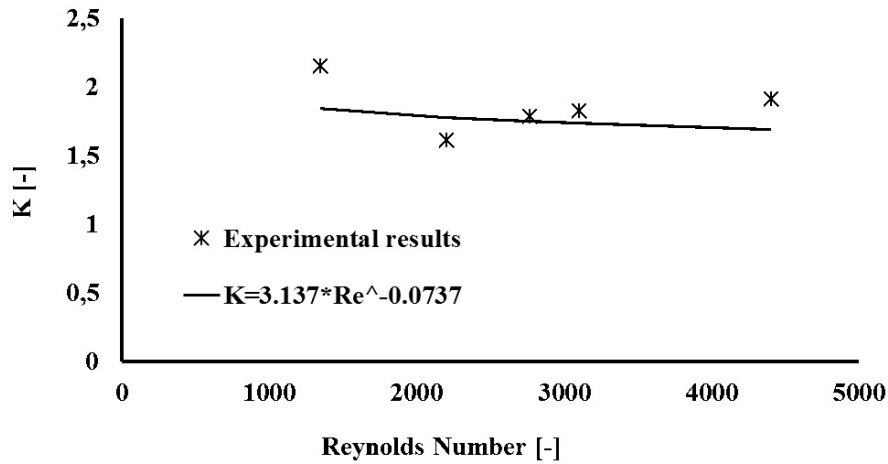


Figure 4.10: Non-dimensional pressure drop with respect to Reynolds number for single phase flow along with the predictions of the correlation of Cioncolini et al. 2015

In order to adjust the non-dimensional pressure drop parameter for two phase flows, a modified two-phase pressure drop parameter is utilized. It is well known that two-phase pressure drop is the sum of three components as accelerational, gravitational, and frictional pressure drops ($\Delta p_{TP} = \Delta p_A + \Delta p_g + \Delta p_{FR}$) for two-phase flows. Due to adiabatic conditions, the accelerational pressure drop is not taken into account, while gravitational pressure drop is negligible due to small scale. Therefore, frictional pressure drop is only considered in the two-phase pressure drop prediction.

There are two approaches used to predict two-phase pressure drop, namely homogeneous (zero slip model) and separate flow models. In the homogeneous model, it is assumed that both liquid and vapor phases move at the same velocity (slip ratio = 1), while the separate flow model considers slip between the phases (different velocities for liquid and vapor phases). Since vapor and liquid phases have different velocities in cavitating flows, the modified separate flow model and most popular Martinelli parameter [157] are used for the pressure drop prediction in the short micro-channel. Accordingly, the following two-phase dimensionless pressure parameter correlation was developed for predicting the experimental data based on

both the single phase dimensionless parameter $K = 3.137Re^{-0.0737}$ and Martinelli parameter corresponding to turbulent flows of both phases for $10^3 < Re < 2.5 \times 10^4$:

$$K_{TP} = 313.75 \left(\frac{1-x}{x} \right)^{1.75} \left(\frac{\rho_g}{\rho_l} \right) \left(\frac{\mu_l}{\mu_g} \right)^{0.25} Re^{-0.0737} \quad (4.3)$$

Here, x is the local vapor quality and calculated using the $x = \frac{\mathbf{H} - \mathbf{H}_{l,sat}}{\mathbf{H}_{lg}}$. Here, \mathbf{H} is liquids enthalpy, where $\mathbf{H}_{l,sat}$ and \mathbf{H}_{lg} are the saturated liquid enthalpy at a given temperature (e.g. room temperature), and the enthalpy of vaporization (liquid to vapor) at the saturated pressure (e.g. 3 kPa), respectively. The comparison between the experimental data and predictions of the correlation is shown in Figure 4.11. As can be seen, a very good agreement exists.

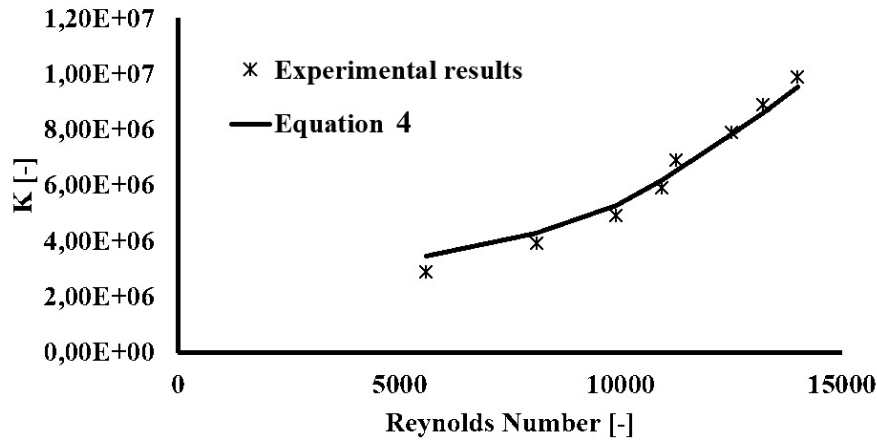


Figure 4.11: Non-dimensional pressure drop with respect to Reynolds number for two phase flow data along with the predictions of the developed correlation

4.3.4 Flow Pattern Classification at the Outlet of The Micro-Channel

Emerging flow patterns are displayed in Figure 4.12. From these figures, it is obvious that different inlet pressures result in different flow patterns. At low pressure, liquid jet can be captured downstream the micro-channel exit, while droplet flow can be observed far from the exit. At higher pressures, jet cavitation and bubbly flow profiles appear. With further increase in pressure, high vaporous bubbly flow pattern is apparent.

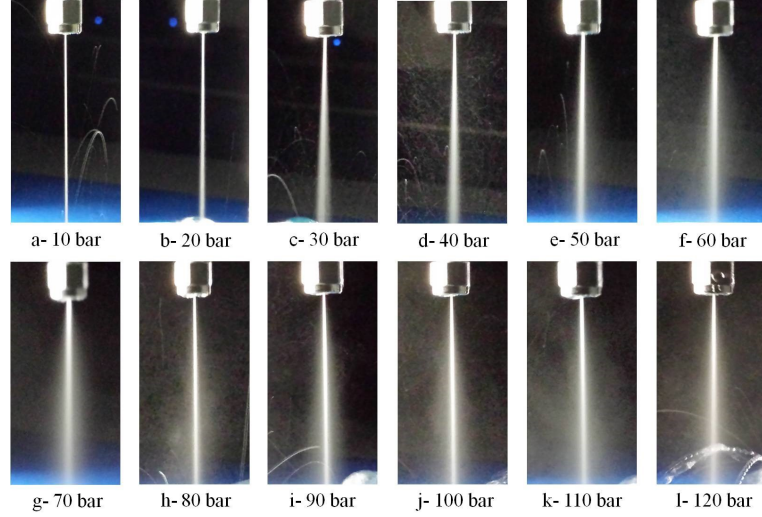


Figure 4.12: Emerging jets from the probe exit at different cavitation intensities

A flow map based on visualized flow pattern is shown in Figure 4.13 and presents boundaries between flow patterns. Cavitation number defined as $K = \frac{p_{ref} - p_v}{0.5\rho v_{jet}^2}$ (where p_{ref} is the reference pressure, p_v is the vapor pressure, ρ is the fluid density, and v_{jet} is the flow mean velocity at different segments of the spray) and the dimensionless position, the ratio X/D_m of the distance from the micro-channel exit to the inner diameter, are utilized as parameters. Cavitation number at lower injection pressure starts from 1.37 and decreases down to 0.1108 at $p_i = 110 \text{ bar}$ for segment 1, where highly vaporous bubbly cavitation patterns exist. As shown in Figure 4.13, highly vaporous bubbly flow exists for Cavitation numbers below 0.4, which correspond to upstream pressures more than 80 *bar* in all segments and in the first segment of the upstream pressure of 50 *bar*. Bubbly flow is visualized for Cavitation numbers between 0.8 and 0.4. Upstream pressures of 50 *bar* for all the segments and the first segment of 30 *bar* result in bubbly flow at the outlet of the micro-orifice. At these injection pressures, bubbles start to move to the outside of the micro-channel and fill the tip of the channel which causes a significant increasing effect on the cone angle of the spray. Jet cavitation is observed below the Cavitation number of 1, which indicates the effect of the generated cavitation bubbles inside the micro-channel on the structure of the spray. Above this number, the spray contains just a single phase, which is affected by the throat velocity. Under these conditions, cavitation bubbles generated inside the micro-channel do not extend to the outside, and the collapse takes place inside the channel. Above the Cavitation number of 2

corresponding to non-cavitating flow conditions, the droplets begin to emerge and continuous flow shifts to discrete droplet flow, which is observed in the third and fourth segments for upstream pressures below 20 *bar*.

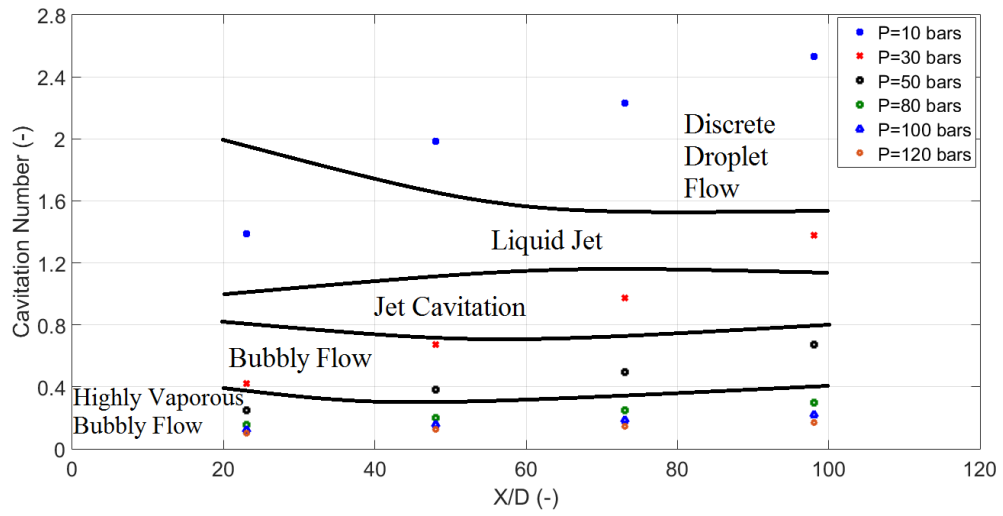


Figure 4.13: Flow patterns in various locations at different Cavitation numbers

Chapter 5

Spray Collapse at the Outlet of the Micro-Channel

5.1 Introduction

Flow regime changes due to the physical and thermodynamical properties inside the channels. The super-cavitation regime is considered as the most suitable regime for spray atomization [158–161], while the hydraulic flip is the least desirable flow regime for spray atomization [10, 162]. Gopalan et al. [163] proved that the main reason of the vorticity in the closure region was the collapse of the cavitation bubbles and the variations in the bubbles size lead to an important change in the turbulence intensity along the study domain.

Kim et al. [164] in their visualization study focused on the oscillation of the bubbles and illustrated pattern damage due to high acoustic pressure as a result of the bubble instability. It was proven [165, 166] that the cavitation bubbles collapse near the wall at the end of a liquid jet in the absence of an ultrasonic source. Kim et al. [164] tried to introduce a dual-transducer in order to increase the population of bubbles. The high density of the bubbles prevents the separation of nano particles and raises the efficiency of the cleaning systems.

Hydrodynamic cavitation was proposed by Arrojo et al. [167] as a considerable alternative to ultrasound cavitation due to its high efficiency and widespread applications in large scale domains. They showed that the pressure pulse was totally different in HC since both flow rate and cavitation phenomenon affected the pres-

sure field, and the inlet pressure was mostly used in HC. Their results revealed that upstream history and pressure recovery are two significant parameters affecting the cavitation collapse. Therefore, pressure recovery and flow distribution along the channel should be extensively evaluated.

5.2 Methods and Materials

The effect of the cavitation phenomenon on the erosion of the kidney stone was previously addressed and it was shown that the energy released from the collapse of the cavitation bubbles and the high velocity of the core liquid jet along the spray were destructive on the targeted area [18]. The previous studies were concentrated on the application of the cavitation phenomenon in biomedical engineering. Hence, the morphology of the spray emerging from the outlet of the micro-channel and the behavior of the spray at different segments for various injection pressures are considered in this study. It is observed that the spray shape is very sensitive to the injection pressure. At lower values of the pressures, the spray does not have a conical shape, and the flow is not continuous at the end of the spray. On the other hand, the spray's conical shape obviously appears at higher injection pressures (Figure 5.1).

Moreover, the dissolved gas contents in the liquids play an important role in the creation of cavitation bubbles when the upstream pressure changes and the fluid flow experiences different regimes inside the micro-channel [168]. The dissolved gases exist in the liquid at the room temperature and pressure and affect the inception of the cavitation due to rectified diffusion. Therefore, besides the increasing pressure and pressure drops, dissolved gas contents in the liquid impact the flow pattern inside the orifice and consequently influence the spray structure. However, when the oscillation of the pressure gets higher and the cavitation bubbles are generated in a large portion, the phase change from liquid to vapor occurs within a very short period of time and the existence of the dissolved gas content is not very possible [63]. Note that to show the spray cone angle at the outlet of the micro-channel, the exposure time was adjusted to $45 \mu s$, while the frame rate for the each segment was 6100 fps with a shutter speed of $10,000 \text{ s}^{-1}$. The maximum resolution of the recorded images was 608800 pixels for the mentioned frame rate. Two LED lights with a supply

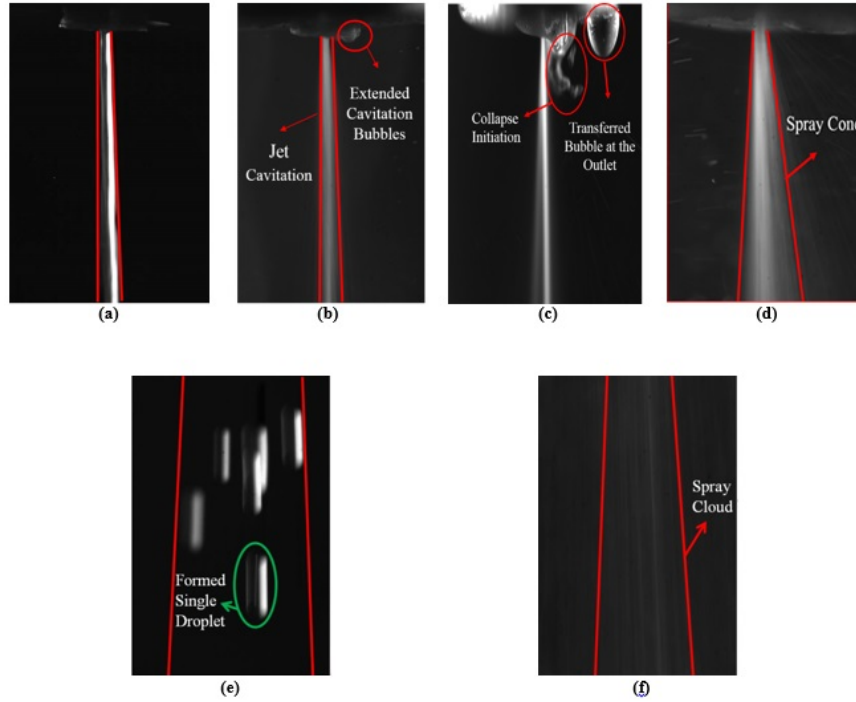


Figure 5.1: The evidence which shows the sensitivity of the spray cone angle with respect to the upstream pressure. First segments of the spray at the outlet of micro-channel were shown at upstream pressure of a) 10 *bar*, b) 50 *bar*, c) 80 *bar*, d) 100 *bar* and, the end of spray was shown at upstream pressure of e) 10 *bar* and f) 100 *bar*.

power of DC 5.5-12 *V* and power of 13 *W* were used in the experiments to study the spray formation including liquid jet, spray cloud and collapse at the outlet of the micro-channel.

The experimental setup and procedure to record the collapse process is as same as the one elaborating in section . A schematic of the experimental setup and micro-orifice configuration, and spray structure are shown in Figure 5.2. Experiments were conducted by applying different inlet pressures ranging from 10 to 120 *bar*, while the outlet pressure at the micro-channel was fixed to 1 *atm*. Cavitating flow generated in the micro-channel was recorded at the micro-channel outlet. The liquid jet and spray cloud were captured at the outlet of the micro-channel for different upstream pressures. The experiments were repeated for several times at different pressures to en-sure repeatability.

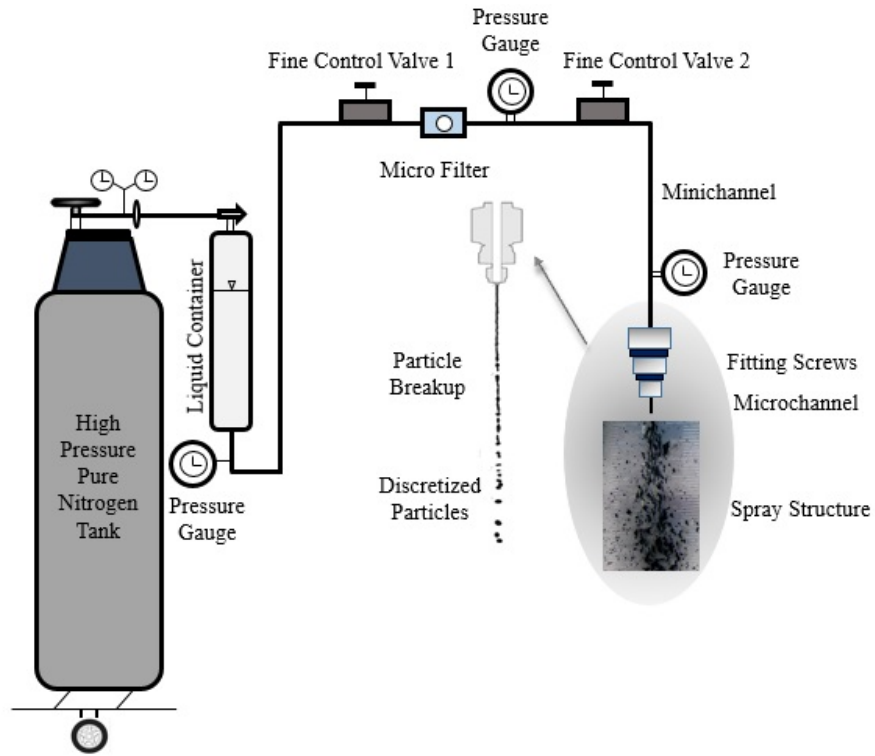


Figure 5.2: Schematic of the experimental setup, the micro-channel configuration, and the spray structure at the outlet

5.3 Results and Discussion

5.3.1 Spray Structure at the Outlet of the Micro-channel at Different Upstream Pressures

The resulting spray at the outlet of the micro-channel is presented at different upstream pressures in Figure 4.12. The liquid jet at the outlet of the micro-channel has almost a uniform structure at a distance of 4.5 mm from the tip of the micro-channel until the upstream pressure is increased to higher than 50 bar . The liquid jet starts to become cloudy at the upstream pressure of 80 bar , and the spray does not conserve any solid shape cylinder at the outlet of the micro-channel, which is due to the high velocity of the departed bubbles and existence of the higher bubble density at the tip of the micro-channel. At this pressure, the extended bubbles are observed at the outlet, and the spray structure is affected by the bubbles existence and their collapse. The interactions among bubbles as well as between bubble and flow increase when the upstream pressure increases. The spray cone angle is shown in Figure 5.3. The figure illustrates that the spray takes a wider shape beyond an

upstream pressure of 70 *bar*, while the change in the cone angle is around 2 *degree* up to this pressure. The cone angle dramatically increases beyond this pressure to approximately 7 *degree*. The recorded images were processed in a pixel-wise manner. Therefore, a measurement conversion from *pixels* to *mm* was identified to study the spray cone angle. The discharge coefficient profile presented in Figure 5.4 indicates that the discharge coefficient is almost constant at higher upstream pressures. Similar findings were also reported in previous studies on micro scale cavitation [18]. The discharge coefficient is dramatically affected by the intensity of the generated cavitation bubbles at higher upstream pressure, and under a special condition of the operating conditions, the flow may flash leading to a slight increase in the discharge coefficient.

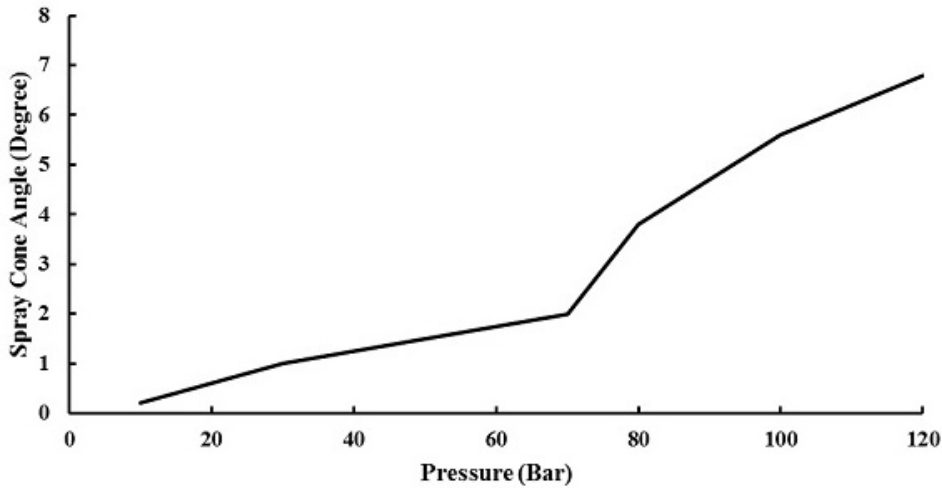


Figure 5.3: Spray cone angle for different upstream pressures

As discussed in the previous sections, the experiments were carried out in a different way to show the cone angle of the spray in a visible manner. Moreover, The spray structure including droplet break up, extended cavitation bubbles and collapse process were captured in this way. The position of the camera needs to be changed to study the segments downstream the micro-channel. Hence, a measurement conversion from pixels to millimeter was identified to study the spray cloud diameter and spray cone angle. New conversion from pixels to millimeter was measured for each segment, since the position of the camera was going to be changed. The exposure time for the second configuration is 45 μs in order to observe the spray deformation due to the collapse process and extended cavitation bubbles. The other parameters

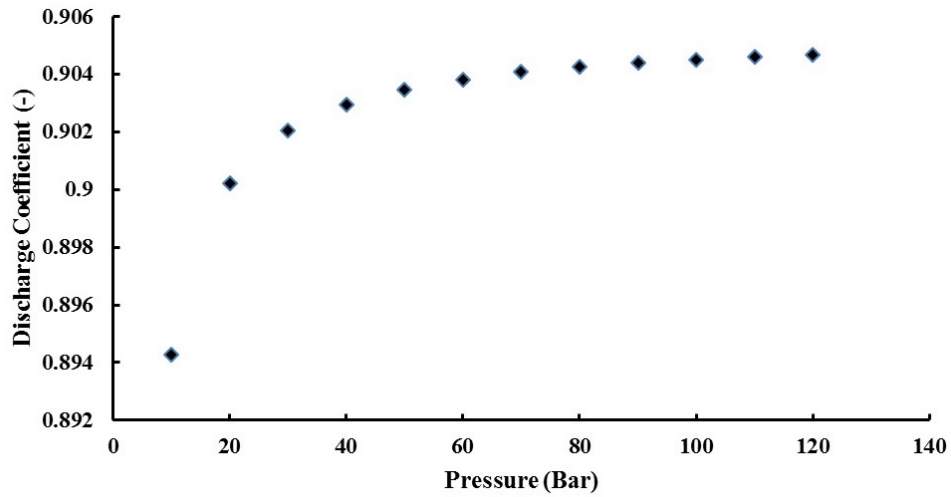


Figure 5.4: Discharge coefficient for different upstream pressures

related to the high speed camera and the experimental setup stay the same and the visualizations for second experiments were carried out for the first four segments at upstream pressure of 10 to 120 *bar*. As it is shown in Figure 5.5 to Figure 5.10, the spray cone angle, droplet breakup and evolution and spray cloud were shown in the different segments of the spray for upstream pressures of 10, 30, 50, 80, 100 and 120 *bar*.

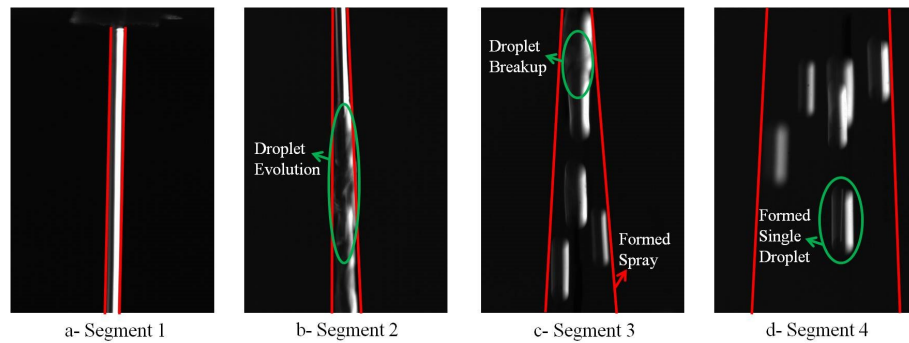


Figure 5.5: Spray at the outlet of the micro-channel for different segments ($p_i= 10$ *bar*)

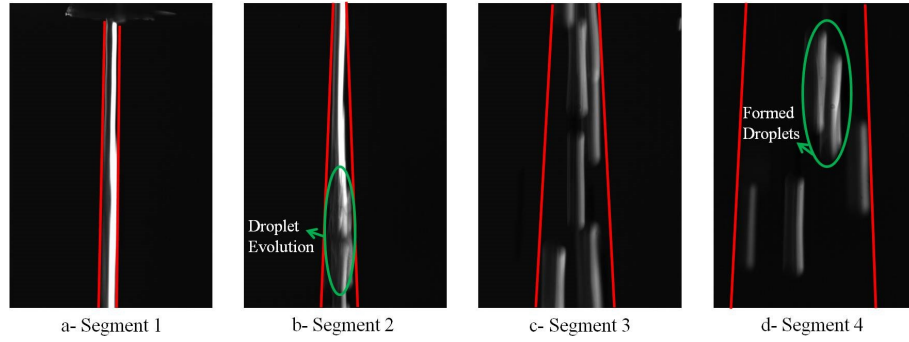


Figure 5.6: Spray at the outlet of the micro-channel for different segments ($p_i = 30$ bar)

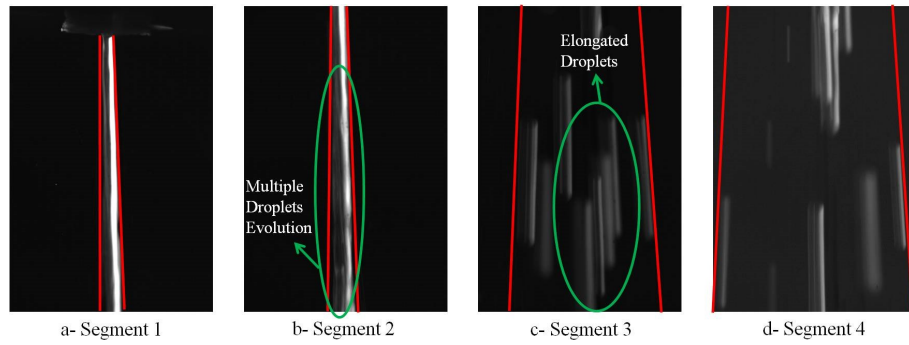


Figure 5.7: Spray at the outlet of the micro-channel for different segments ($p_i = 50$ bar)

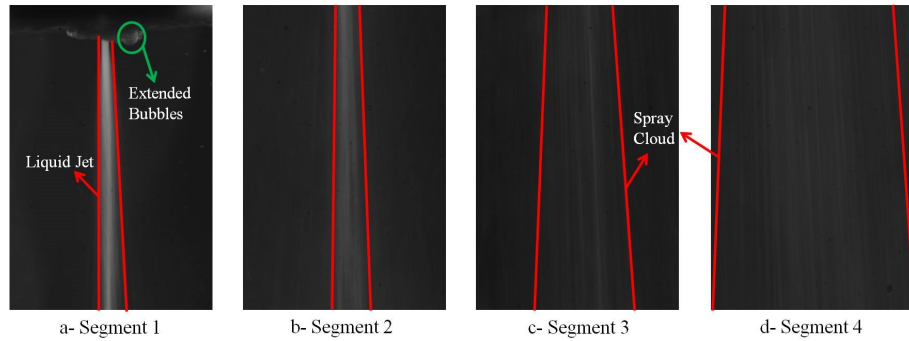


Figure 5.8: Spray at the outlet of the micro-channel for different segments ($p_i = 80$ bar)

5.3.2 Collapse of the Cavitation Bubbles

The cavitation bubbles form and collapse in millisecond and affect the flow pattern inside the channel. The flow characteristics at the outlet of the channel determine the behavior of the spray. It is expected that the shear force becomes more effective at the exit area of the micro-channel especially at higher pressures, and therefore, the spray can be influenced dramatically by the sudden change in the state of the

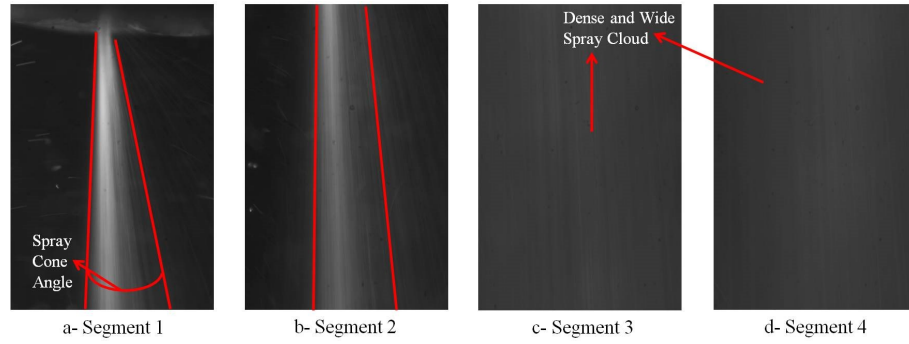


Figure 5.9: Spray at the outlet of the micro-channel for different segments ($p_i = 100 \text{ bar}$)

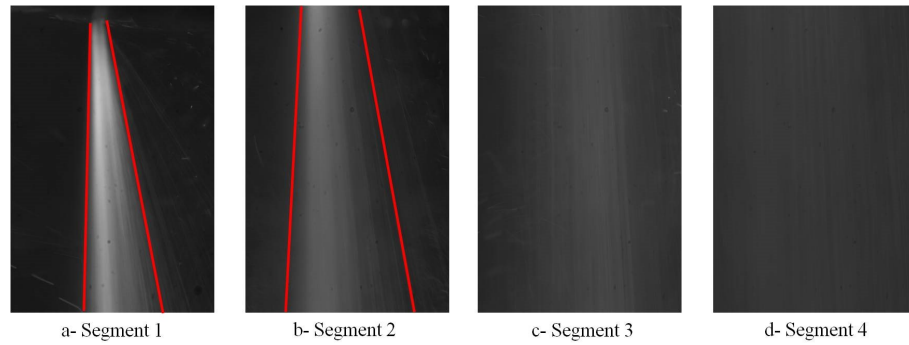


Figure 5.10: Spray at the outlet of the micro-channel for different segments ($p_i = 120 \text{ bar}$)

fluid flow. Hydrodynamic interaction among bubbles in the liquid-bubble system creates oscillations in the fluid flow, which is of great importance due to the theory of viscous suspension. Therefore, besides the high injection pressure, the interaction among bubbles causes considerable fluctuations in the pressure and velocity of flow field. It was reported that the effect of the bubble-bubble interactions influences the natural resonance frequency of the average size bubble, which is appreciable when the fluctuations of the fluid flow are significant at high upstream pressure. It is crucial to carefully study the flow at the outlet of the micro-channel and focus exactly on the outlet of the micro-channel to capture the collapse of the cavitation bubbles. The fluid flow at the outlet of the micro-channel is visualized starting from lower upstream pressures. The shape of the spray is strongly influenced by the occurrence of the collapse, and more bubbles disperse within the spray length. The spray in the main stage of the collapse process is more conical downstream of the spray, and at this point, both liquid jet and energy released from the collapse of the cavitation bubbles are counted as two significant mechanisms in the possible

erosion of the targeted area addressed in our previous study [18]. The population of big and small bubbles increases at higher pressures, and therefore, the spray is considerably affected by the collapse process. It is seen that at such pressures the jet spray is more conical compared to the previous cases, and the liquid jet intensity is higher due to the collapse of the bubbles. Also, it can be seen in Figure 5.11 that a stationary cavity is formed at high pressure, which creates inchoate bubbles. Similar flow patterns were also recorded in previous studies on micro scale cavitation [18] and were associated with choked flow conditions. The collapse process of these bubbles is shown in Figure 5.11 at an upstream pressure of 100 *bar*.

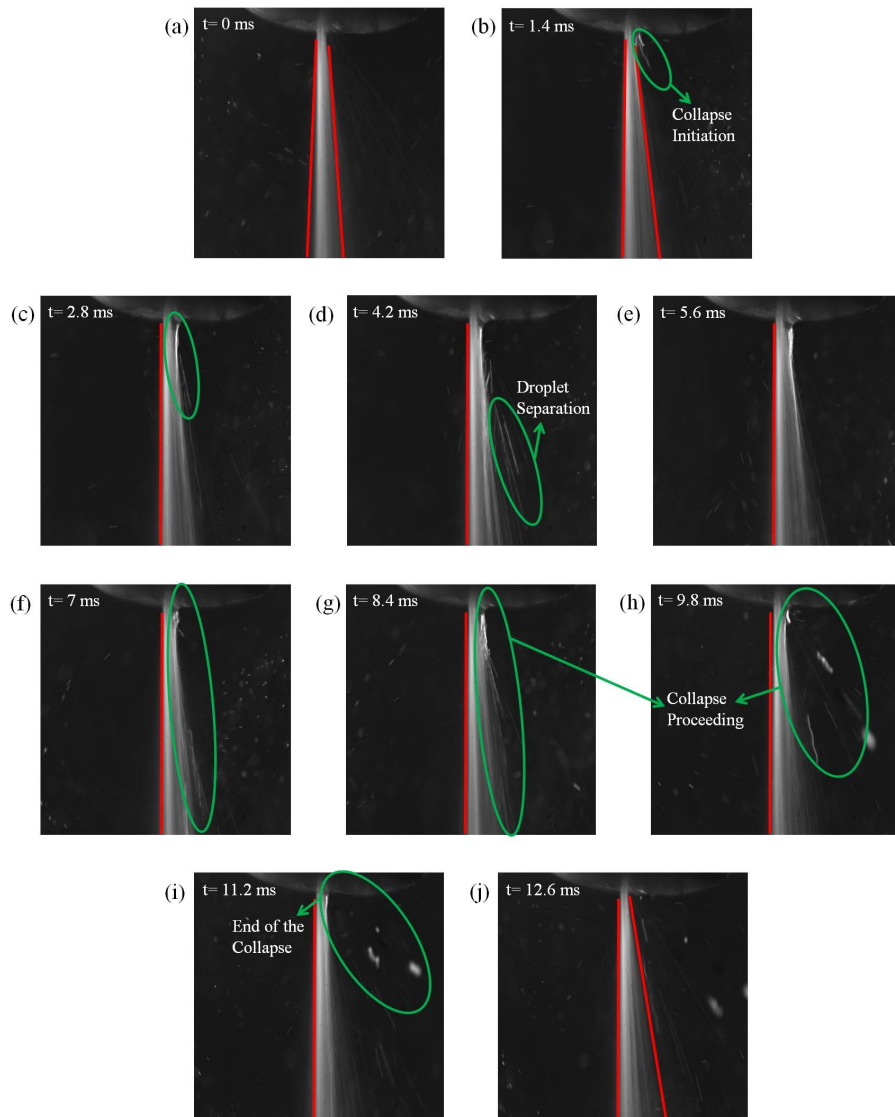


Figure 5.11: The collapse process along the spray length at the outlet of the micro-channel ($p_i=100 \text{ bar}$)

The collapse process of these bubbles occurs within 12.6 and 3 *ms* and highlighted

in Figure 5.11 and Figure 5.12, respectively. The collapse of the bubbles is also shown in Figure 5.12 at an upstream pressure of 120 *bar*. The results of the collapse process were visualized at a high exposure time (45 μs) in order to illustrate the structure of the spray due to the cavitation generation inside the micro-channel and collapse process inside and outside of the micro-channel.

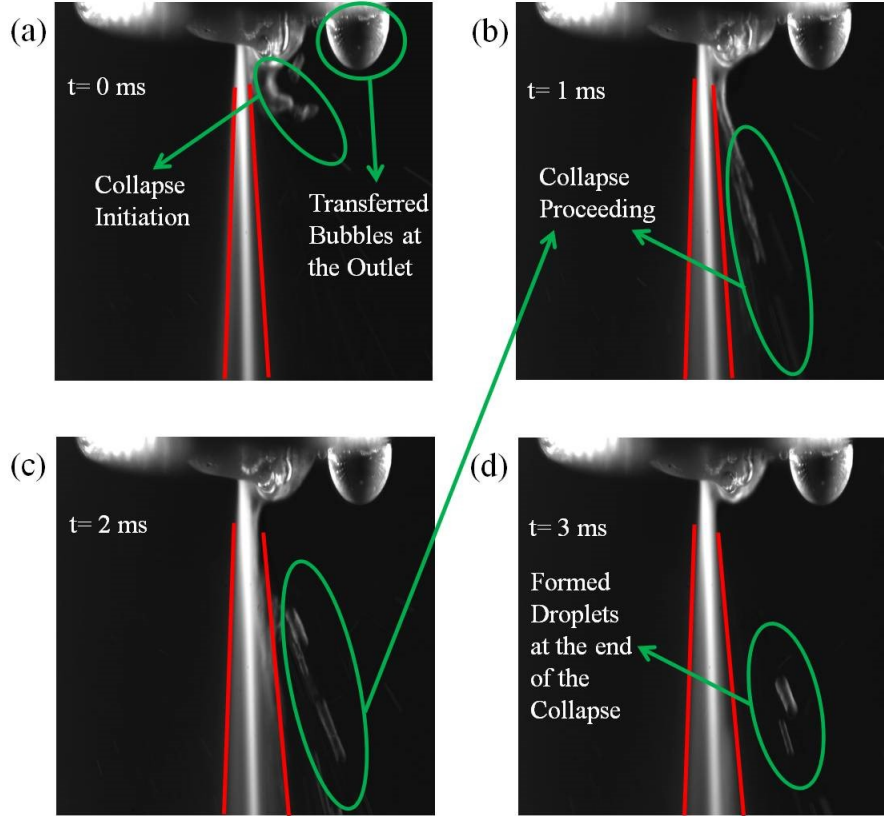


Figure 5.12: The collapse process along the spray length at the outlet of the micro-channel ($p_i=120$ *bar*)

5.3.3 Collapse of Cavitation Bubbles: An Application Case Study

In this study, we propose a technique to maintain the performance and stability of nanofluids with the use of cavitating flows through micro-orifices to prevent agglomeration and sedimentation of nanoparticles, which will increase the durability of the nanofluids. Gamma-alumina nanoparticles with a mean diameter of 20 *nm* suspended in water were utilized. In the current approach, a flow restrictive element induces sudden pressure, which leads to cavitation bubbles downstream from the orifice. The emerging bubbles interact with the agglomerated structure of nanopar-

ticles and decrease its size through hitting or shock waves generated by their collapse, thereby increasing the stability and reusability of nanofluids.

The cavitation phenomenon has a significant effect on jet flows in flow restrictive elements. The cavitation bubbles improve the efficiency of the microfluidic systems, enhance the combustion process, and increase the fragmentation ratio of the targeted areas by generating dispersed and discretized spray structures. The pressure reduction at the element leads to cavitation bubbles with different sizes and distributions depending on the fluid flow characteristics. Pioneering studies on hydrodynamic cavitation in micro scale revealed different characteristics of cavitating flow in the micro scale compared to cavitating flows in the macroscale. The cavitation phenomenon also has a significant effect on the cone angle of the spray, penetration, and spray breakup. The sudden drop in pressure and subsequent generation of cavitation bubbles result in better spray atomization and efficient spray primary and secondary breakup in the micro flow restrictive elements. The schematic of the proposed technique, which is based on a recent patent application by the authors, is shown in Figure 5.13. The nanofluid having nanoparticle clusters is guided to a short micro flow restrictive element such as an orifice or a venturi. This flow restrictive element induces a sudden drop in pressure due to low pressure; small bubbles from the flow restrictive element emerge due to cavitation. The emerging bubbles interact with the agglomerated structure of nanoparticles and decrease its size through hitting and/or shock waves and liquid jets, which are generated by their collapse. As a result, the resulting average nanoparticle size decreases at the exit of the flow restrictive element, and the stability of nanofluids is promoted.

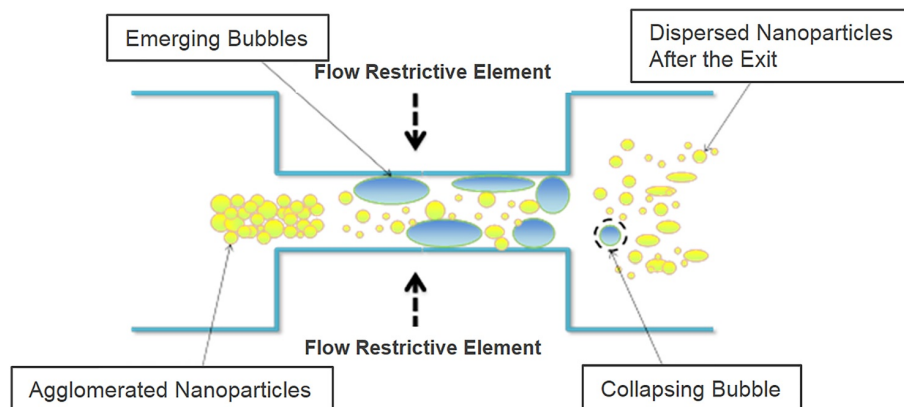


Figure 5.13: Schematic of the proposed technique

Cavitating flows were generated with a sudden drop in pressure across a 4.5 *mm* short micro-channel with an inner diameter of 152 μm . The experimental conditions, channel geometry, and dimensions were selected based on our previous studies for ensuring cavitation bubbles at the exit to validate the proposed method. According to the results provided in our previous study, there are few cavitation bubbles downstream of the channel at an upstream pressure of 10 *bar* when long channels are employed. More generated cavitation bubbles can extend to the outlet of the micro-channel at higher pressures. For a short micro-channel, the possibility of occurrence of bubble collapse downstream of the micro-channel is higher compared to a long micro-channel so that the energy released from the collapse of the cavitation bubbles can be further exploited in the proposed technique, and erosion due to the collapse of bubbles inside the channel can be avoided. As a result, the micro-channel length was kept as short as possible.

In the micro scale, cavitation typically incepts toward the inlet of the flow restrictive element due to the potential low pressure zones and more pronounced surface effects in the small scale. As a result, surface nuclei are the key parameter for the inception of hydrodynamic cavitation. In this study, the length of the micro-orifice was kept as short as possible so that the emerging bubbles would collapse downstream of the orifice. Their collapse generates shock waves as well as jet flows, which exert very high stress on the exposed surfaces/structures [169]. This results in a destructive effect on the agglomerated structures of nanoparticles and recovers the stability of nanofluids at the same time. The Cavitation number is the most influential parameter indicating the intensity of the cavitation. The Cavitation number is highly dependent on the reference pressure and the reference velocity. An increase in the inlet pressure results in higher flow velocities and intensifies cavitation. Therefore, as illustrated in Figure 5.14, a decrease in the Cavitation number (intensifying cavitation) results in the increase in the reduction ratio of the nanoparticle size after exposure to the cavitating flow. When nanoparticles are added to the working fluid, a triple line of gas-liquid-solid nanoparticles forms, which affects the inception and growth of the bubbles.

It was reported that the size of the bubbles decreases in the presence of nanoparticles and the population of the generated bubbles increases [170]. Thus, the existence

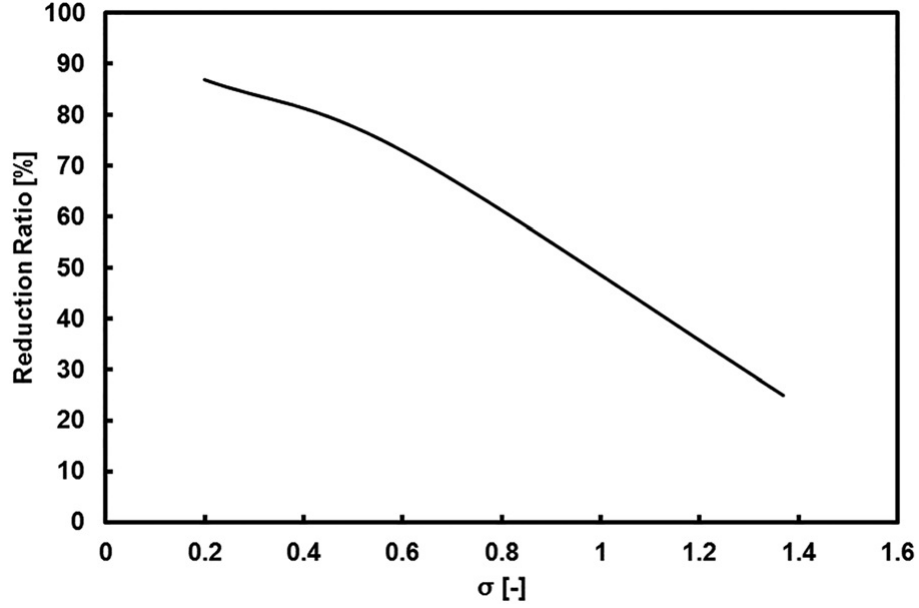


Figure 5.14: Reduction ratio of nanoparticles size as a function of the Cavitation number

of nanoparticles affects the collapse process and more small cavitation bubbles will emerge with the presence of nanoparticles, which further facilitates the deagglomeration of the nanoparticle clusters. During the collapse process of emerging bubbles, a liquid jet is generated in addition to the shock wave. On the other hand, a significant amount of the energy is transferred with the shock wave to cause erosion on the surface of the nanoparticles. The impact pressure as a result of the interaction between the shockwave/liquid jet and the solid interface is expressed using the conservation of mass and momentum as follows:

$$p_{imp} = \frac{\rho_l a_l v_{jet}}{1 + (\rho_l c_l) / \rho_s a_s} \quad (5.1)$$

where ρ_l and ρ_s are density for liquid and solid, respectively. a_l and a_s are the speed of sound for liquid and solid, respectively, and v_{jet} is the jet velocity.

The Youngs modulus, E_s , is very large for the solid phase; therefore, $a_s = \sqrt{E_s / \rho_s}$ also becomes very large. As a result, the impact pressure can be simplified as:

$$p_{imp} = \rho_l c_l v_{jet} \quad (5.2)$$

Accordingly, the impact pressures at upstream pressures of 10, 60, and 90 *bar*

are found as 45.47, 112.4, and 159.94 *MPa*, respectively. These values are in the range of the flexural/compressive strength of Alumina ceramics which proves the effectiveness of the proposed method.

Chapter 6

Energy Harvesting in Micro Scale with Cavitating Flow

6.1 Introduction

Power reclamation from user-friendly energies and affordable devices has been commonly exploited during the last decades. With the increasing risk of termination of the natural energy sources, the renewable and sustainable energies, and new energy generation receives much attention in the energy sectors and markets. Hydrodynamic cavitation as a feature of a phase change from liquid to vapor at low static pressure is a source of short-period heat generation at the phase of the collapse of the created bubbles. Here, we are showing that with the aid of the hydrodynamic cavitation in a low-cost and clean system, the spray jet has the capability of heat generation in contrast to the common use of spray jet in the cooling applications. The emerged spray is under the effect of the micro scale cavitating flow inside the micro/min-channels which is much more intense in comparison to its correspondence at macro scale. The temperature measurements on a black-covered aluminum plate subjected to the spray interestingly present a temperature increase of $5.2\text{ }^{\circ}\text{C}$ for a specific micro-channel configuration. This temperature rise would be potentially utilized as a power source in miniature electric appliances with a simple energy conversion device. The complementary study for the visualization of the spray structure is also carried out for all the cases at different conditions. The observation of the spray at various successive segments illustrates an interesting trend in the flow

regime change from micro to macro scale cavitating flow.

6.2 Experimental Procedure and Characterization

The cavitation bubbles generator in this study is structured as a hydrodynamic cavitation generation device with the use of high upstream pressure supplier as shown in Figure 6.1. The experimental setup consists of simple equipment which are using in the hydraulic industries. A high pressure pure nitrogen tank (Linde Gas, Gebze, Kocaeli) supplies the required upstream pressure for the system. This tank is connected to a 1 *Gallon* fluid reservoir (Swagelok, Erbusco BS, Italy) which is filled with de-ionized (DI) water as working fluid. The reservoir is connected to two tubes (stainless steel and PEEK tubes) and several gaugeable tube and adaptor fittings. Two pressure sensors (Omega, USA) at the entrance and end of the tubing system are mounted on the device to measure the pressure and two fine control valves (Swagelok) are connected to the system to control the flowing fluid at different locations. A micro Tee-Type filter (Swagelok) with 15 μm nominal pore size is used to prevent the flow of any particle larger than 15 μm to the system. An aluminum plate with the surface of 11 cm^2 is employed at an optimum distance from the tip of the micro/mini-channels to act as a surface body in the process of the collision of the emerged spray. This plate is connected to the system via sustainable clamps in order to be hold without vibration. A thermal camera (Flir Systems, USA) and a workstation with post-processing software are utilized to capture the thermal variation on the surface of the aluminum plate as a results of the spray collision. Moreover, a Phantom high speed camera (Phantom V320 high speed camera) with appropriate lenses and a visualization software (Phantom PCC 2.0 software) are used to record the spray structure at the outlet of the micro/mini-channels. To illuminate the flow background during the visualization tests, two LED lights are employed exactly at the same height with the high speed camera.

6.2.1 Device Characterization

The main part of the system is the bubble generation section where the cavitation bubbles are created. This section has the location where a stainless steel tube with

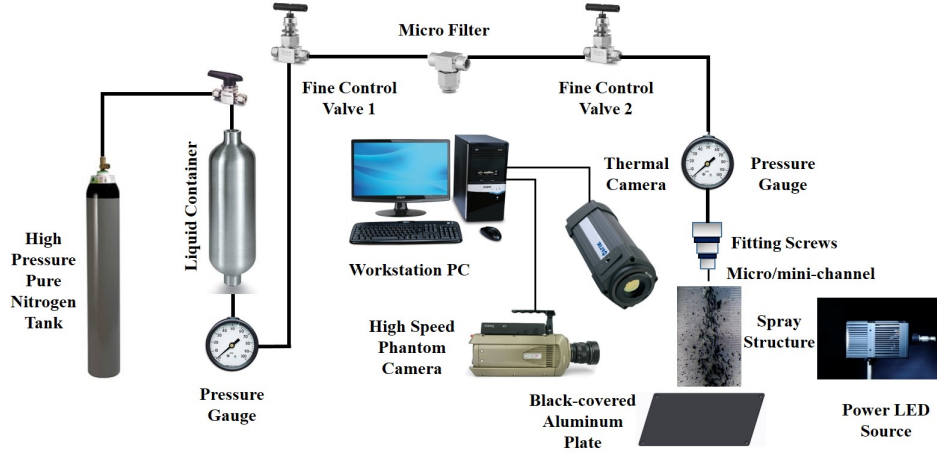


Figure 6.1: A schematic of the proposed system for generating the cavitation bubbles and spray emergence under the effect of the cavitation

the diameter of 3 mm is connected to a PEEK micro/mini-channels with diameters of 152, 256, 504 and 762 μm . Therefore, the connection point between the tubes are fitted properly in order to have a sudden reduction in the diameter of the channels and hence, obtain the appropriate condition for the reduction of the static pressure leading to the generation of the cavitation bubbles. Furthermore, the length of the PEEK channels are selected in a way that the created cavitation bubbles can easily reach to the end of the channel. Thus, the micro/mini-channels are kept as short as possible (4.5 mm) in order to utilize the energy released from the rupture of the cavitation bubbles. Using the thermal camera required great attention in terms of reflection, observation angle effect and also emissivity to record precise temperature measurement. Therefore, besides the camera calibration, aluminum plate is colored in black to avoid any reflection and increase the emissivity.

6.2.2 Experimental Procedure

The experiments are carried out in two steps. Firstly, the temperature variations are measured with the aid of the thermal camera on the black colored aluminum plate, then the spray structure is visualized utilizing the high speed camera. In the first section, the aluminum plate is held at a distance of 1.8 cm from the tip of the channel with appropriate clamps and the temperature is measured with the

use of thermal camera for different upstream pressures. Upstream pressures are selected as 10, 40 and 60 *bar* while the spray discharges to the atmosphere at the pressure of 1 *bar*. Four micro/mini-channels with inner diameters of 152, 256, 504 and 762 μm are mounted on the system and the temperature is measured at three different time steps for each channel and each upstream pressure namely; at the time of the collision, 30 and 120 *seconds* after the spray collision on the aluminum plate.

In the second phase, the spray structure is observed for the aforementioned channels at different segments and injection pressures. To do so, the spray structure is divided into six identical segments from the emergence of the spray at the outlet of the channel up to location where spray interacts with the aluminum plate. Each segment has a length of 3 *mm* while the visualization is performed at several upstream pressures from 5 to 60 *bar*. The maximum resolution of the recorded images is 608×800 *pixels*. A power LED is used at 1 μs exposure time to study the spray structure at the outlet of the micro/mini-channels.

6.2.3 Flow Characterization

The spray is characterized with non-dimensional numbers including cavitation, Mach and Reynolds numbers and, mass flow rate is obtained from measuring the fluid mass passing from the outlet cross-sectional area at the given time period. The experiments are carried out at a vast range of upstream pressures and all the temperature measurements and visualization tests are repeated several times to watch out the reliability of the obtained results. Using the manufacturers specification sheets and also the propagation of uncertainty method the important uncertainties including cavitation number ($\pm 6.7\%$), flow rate ($\pm 1.4\%$), inner diameter ($\pm 0.002\text{mm}$) and pressure drop ($\pm 0.3\%$) are calculated and presented.

6.3 Results and Discussion

The bubble dynamics is predominantly studied from the simplest point of view in order to eliminate the sophisticated unknown parameters. Therefore, one can use momentum equation to make a relation among bubble radius and pressure differ-

ence between bubble and ambient far from the bubble in the simplest way. The next step to make the bubble dynamic study more complex is to focus on the dynamic boundary condition. In this case, viscous and surface effects are added to the cluster of parameters and constitute the famous Rayleigh-Plesset equation in the common form. Up to this point, the only terms which play the role on the behavior of the bubble radius are pressure difference, surface and viscous effects (inertial effect) which are arduous themselves to be investigate particularly when size scale is diminishing.

The problem of the bubble dynamics gets intricate when the bubble content is taken into account. Under this condition, the bubble pressure includes vapor pressure and partial pressure of the gas content inside the bubble. Partial pressure of the gas depends upon the temperature and the bubble size ratios. Therefore, the temperature effect becomes crucial when the dissolved gas content or contaminant existed in the bubble are considered. To be fairly general, it is almost impossible to neglect the bubble contents in the experimental and practical investigations where it takes long time to reduce the concentration of these contents with the aid of expensive wind tunnel and other equipment.

The thermal effects become momentous at two stages during the collapse process. First, in the early step while the bubble is growing and second, in the last step of the collapse when the bubble contents are dramatically compressed and affect the temperature variation. Although it is proven that the pressure and temperature rise occurs in very short time period, the temperature gradient is still high enough. Besides, short distance between the center of the bubble-where the highest temperature is recorded during the collapse-and the boundaries makes the theory strong that there must be a platform to utilize the temperature gradient from the collapse of the cavitation bubbles. It was demonstrated before that the cavitation phenomenon gets more serious when the size scale shrinks to the micro scale. The cavitating flow regime, cavitation inception, destruction ratio, turbulence effect, cavitation hysteresis and surface effects are amongst the parameters which show a different behavior in micro scale in comparison to macro and conventional scales. After understanding the cavitating flow physics in the micro domain, we proceed with new idea about energy harvesting from the collapse of the cavitation bubbles which has not been

addressed in literature to the best of our knowledge.

6.3.1 Temperature Variation on a Solid Body under the Effect of Cavitating Flow

The effect of the cavitating flow on the solid surface at a distance of 1.8 cm is shown in Figures 6.2 and 6.3 for different channels and at various times steps in terms of pressure and temperature. The temperature contours recorded via thermal camera in Figure 6.2 are supported with analysis shown in Figure 6.3. Four different channels used in this study are classified as micro/mini-channels with diameters of 152, 256, 504 and 762 μm . The flow regime at the outlet of the channels is recorded using high speed visualization system and laser shadow probe to observe the flow regimes. The recorded images of the emerged spray show that the last channel with a diameter of 762 μm illustrates totally different behavior with the other channels. This behavior is also seen in the thermal effect on the solid boundaries and gives an idea that we are encountering with two distinct thermal energy features related to two different scales.

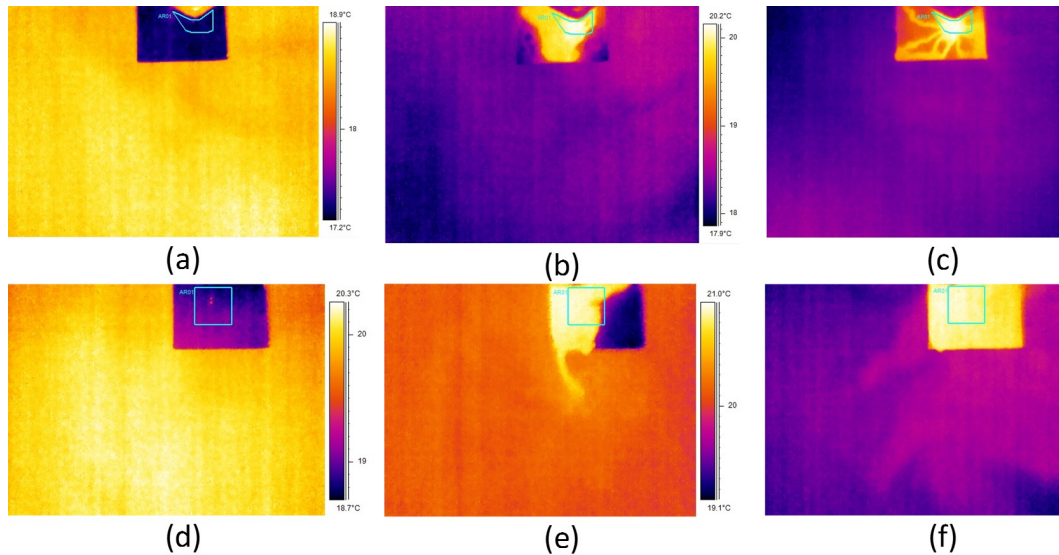


Figure 6.2: Thermal counters captured by thermal camera on the solid surface for (a) without spray apply (152 μm) (b) At the time of first collision (152 μm), (c) 30 seconds after the collision (152 μm), (d) without spray apply (504 μm), (e) At the time of first collision (504 μm), (f) 30 seconds after the collision (504 μm)

Emerging spray is frequently used as a cooling system in various applications,

while most of these studies are carrying out in macro scale. Here, we are trying to show that there is a possibility to provide an adverse effect with the use of same system. The cavitation is the phenomenon which is responsible for this inversion with nucleation, bubble growth and collapse process. The idea arises from the fact that there are considerable generated cavitation bubbles which travel along the channel and collapse at the end of the channel length or may discharge from the channel in the special boundary condition. Moreover, our recent studies illustrate that much more cavitation bubbles are generated in the channels with inner diameter of 256 and 504 μm . It is indicated that cavitation bubbles are generated in large magnitude and the cavitating flow is extended to the outlet of the channel at higher upstream pressure in the micro scale. It is also observed in the previous experimental investigations that there are plenty of generated cavitation bubbles which move to the outlet of the micro-channels at higher upstream pressure and increase the possibility of occurrence of collapse process at the outlet of the microchannel. These findings make the system reliable to perform further studies on it to utilize the collapse of created cavitation bubbles in an affordable manner.

The experiments are carried out for several times at different conditions to make sure of the repeatability and reproducibility of the results. The experiments exhibit temperature rise for all the cases and it is inevitable that cavitation occurs in all of them according to the previous findings. Figure 6.2 shows the selected contours of the temperature variation on the solid surface with a box on the interface to measure the mean temperature on the area where the cavitating spray is applied. The box on the solid boundary is drawn according to the spray diameter and the location where the spray interacts with the surface. The first contour on each row of the Figure 6.2 shows the temperature at rest when there is no any applied spray on the solid body and the figure is recorded to make the comparison between the successive flow conditions. The subsequent contours show the temperature variation for different conditions when the spray strikes the surface. The detailed analysis on the temperature rise is displayed in Figure 6.3 where the temperature variation is shown at three different time periods. The temperature is measured exactly at the time of collision for all the cases as shown in Figure 6.3(a). The second and third temperature measurements are recorded 30 and 120 seconds after the spray

applying as shown in Figure 6.2(b) and (c), respectively. The reason to measure the temperature at three different times is to follow the stability and steadiness of the temperature rise in order to harvest the reliable heat transfer magnitude.

The room temperatures for the selected experiment sets are 17.3, 19.3, 19 and 19.6 °C for micro-channels of diameters of 152, 256, 762 μm, respectively. Figure 6.3(a) shows that there is a harmonic temperature rise for all the channels from upstream pressure of 10 to 60 bar at the time of spray apply. The highest temperature rise is recorded as 2.6 °C for the micro-channel with diameter of 152 μm and at upstream pressure of 40 bar. The micro-channels with diameter of 256 and 504 μm also show a temperature increase of 2.5 °C for upstream pressure of 40 bar. The mini-channel with diameter of 762 μm experiences its highest temperature at upstream pressure of 40 bar with the temperature rise of 1.7 °C. The temperatures for all the channels at upstream pressure of 60 bar are more and less consistent and change slightly few tenth of degree relative to the corresponding temperature rise at the injection pressure of 40 bar. This would be due to the movement of the cavitation bubbles to the end of the channels at both 40 and 60 bar for all the cases. Moreover, the collision of the spray with the solid body gets intense at the higher upstream pressure leading to much more heat dissipation and loss at the outlet of the channels.

The temperature is measured 30 seconds after the first collision of the emerging spray on the solid body for all the case as shown in Figure 6.3(b). As expected, there are increases in the temperature and therefore, enhancements in the heat transfer. The spray at the outlet of the channels experiences decomposition along the penetration length leading to an enhancing effect of the created cavitation bubbles on the disintegrated droplets and bubbles during the primary and secondary break-ups. The primary break-up leads to creation of big droplets/bubbles which makes the region close to the nozzle dense and thick. The next stage in the spray structure is secondary break-up where smaller droplets/bubbles are generated from the big droplets/bubbles. The secondary break-up occurs due to the aerodynamic forces existing on the relative velocity between droplets/bubbles and the surrounding's gas. Aerodynamic forces decrease the droplets velocity and droplets at the tip of the spray tolerate much more drag forces. Therefore, the droplets at the tip of the

nozzle change to new ones consistently and the spray penetration increases. Hence, more and faster droplets/bubbles interact with the solid body as the time passes. It is also expected that the temperature rise becomes steady after a certain duration and gives us the optimum temperature augmentation for the studied cases. It is shown in Figure 6.3(c) that the temperature does not change sensitively at the time step of 120 *seconds* compared to the time step of 30 *seconds* after the spray emergence.

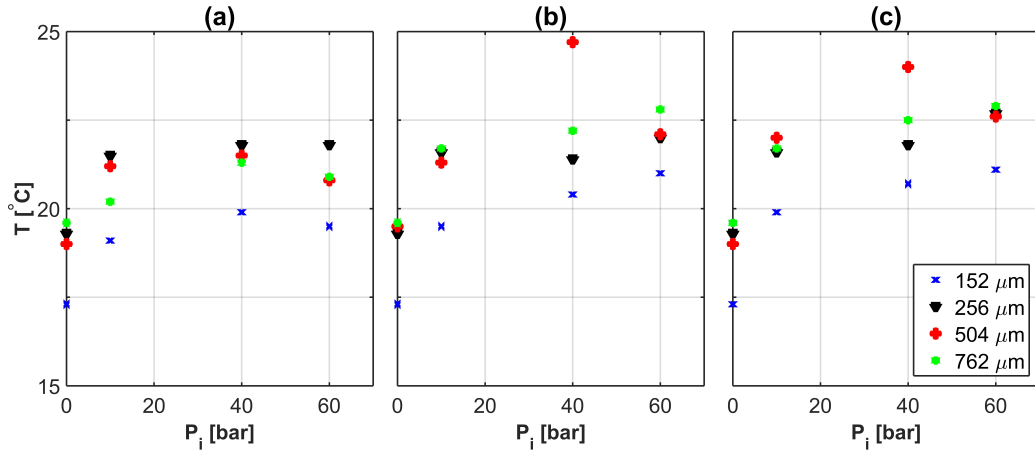


Figure 6.3: The temperature variation on the solid surface with respect to the upstream pressure for (a) just on the time of spray collision on the surface, (b) 30 *seconds* after the collision, (c) 120 *seconds* after the collision

The highest temperature rise after 30 *seconds* of the interaction is recorded as 5.2 $^{\circ}\text{C}$ for micro-channel with inner diameter of 504 μm at the upstream pressure of 40 *bar*. It is emphasized that this value is recorded for several times for the mentioned channel to make the results more reliable. This finding is getting much more interesting when we take a look at the flow regime change for channels with diameters of 504 and 762 μm as illustrated in Figure 6.4. It was already mentioned that the cavitation phenomenon shows a different feature when the size scale reduces to micro scale and the experimental thermal measurements and spray visualization supports these observations. Therefore, we show here that with the aid of hydrodynamic cavitation created inside the micro/min-channels and optimizing the distance between the tip of the nozzle and the solid surface, there is a possibility to reach a temperature rise of approximately 5 $^{\circ}\text{C}$. There is an increase in the temperature of the solid body for the mini-channel with diameter of 762 μm as 3.2 $^{\circ}\text{C}$, but this value is still

below the temperature rise for the micro-channel with diameter of $152\ \mu\text{m}$ ($4.3\ ^\circ\text{C}$).

The same trend of temperature rise is recorded for the time step of $120\ \text{seconds}$ where highest temperature rise is recorded for micro-channel with diameters of 504 and $152\ \mu\text{m}$ as approximately $4\ ^\circ\text{C}$. Overall, the extracted results from Figure 6.3 show a temperature rise between 2 and $5\ ^\circ\text{C}$ for all the channels at different upstream pressures. The temperature rise is captured in all the cases and also a second temperature rise is seen $30\ \text{seconds}$ after the spray collision with solid body for all the channels. Furthermore, the temperature shows a consistent trend after $30\ \text{seconds}$ of the interaction closing to the time step of $120\ \text{seconds}$ for all the cases. This fact supports the use of thermal energy for a long time period of the cavitation creation and spray emergence under the effect of the generated cavitation bubbles.

6.3.2 Flow Regimes Hysteresis from Micro to Macro Scale Cavitating Flow

To study the flow regime, a depth observation with the aid of high speed visualization system is done for the mentioned channels at the different locations of the spray length. The visualization of the spray shown in Figure 6.4 is carried out at six segments in a way that the first one is at the exit of the channels and the last one is prior to the spray collision on the solid body. The aim is to capture the flow regime difference between the channels and also to record the primary/secondary break-ups. The recorded images exhibit an interesting regime evolution along the channels from smaller to the larger one. Firstly and foremost, the flow pattern in most of the segments for the channels with inner diameters of 152 , 256 and $504\ \mu\text{m}$ shows a monotonic trend.

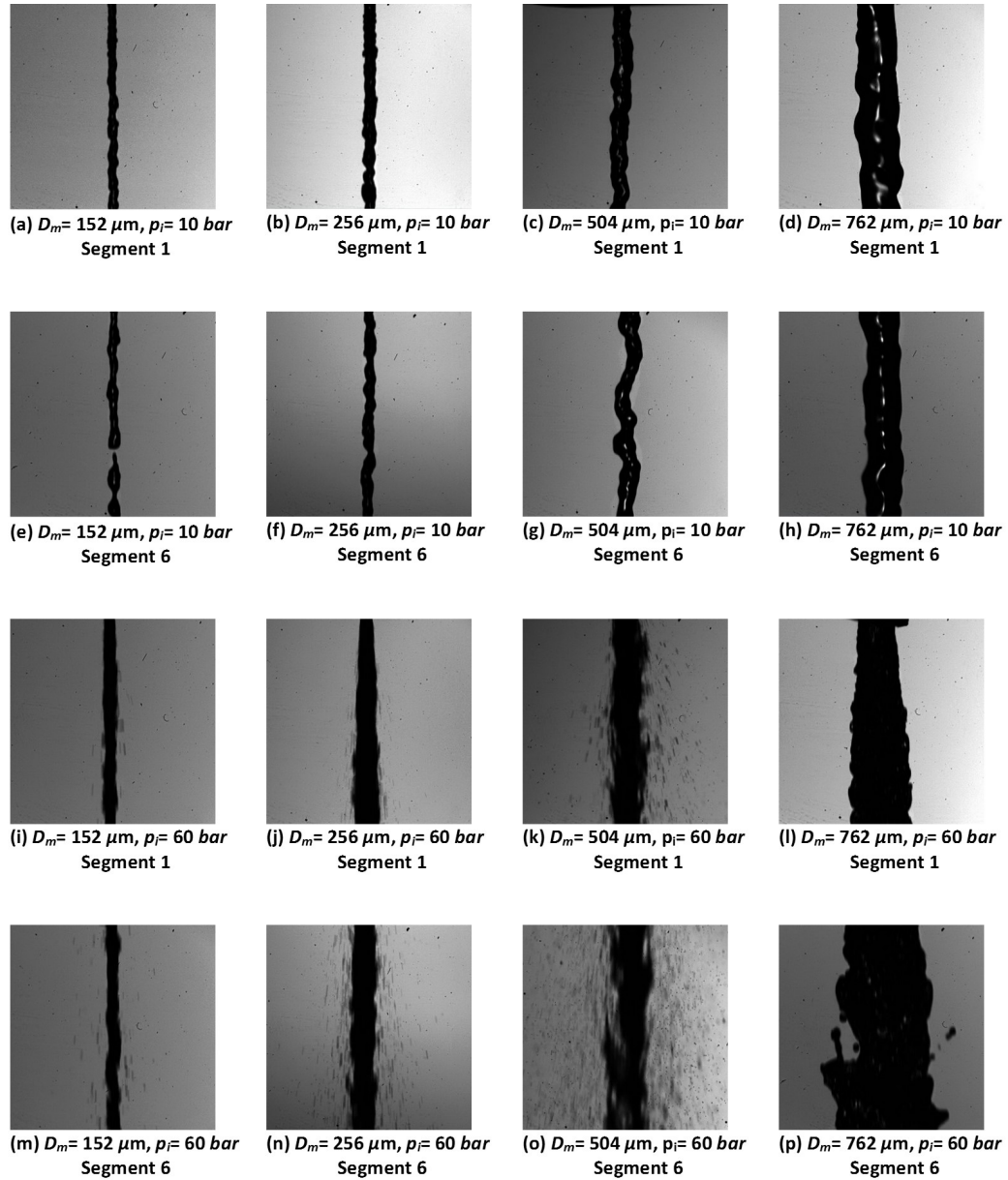


Figure 6.4: The spray flow regime at the outlet of the micro/mini-channels for different upstream pressures and at first and last segments of the spray structure

To be clear, the spray gets a conical shape in almost all of the channels except $762\ \mu\text{m}$, however the flow regime changes totally when the diameter of the channel varies from 504 to $762\ \mu\text{m}$. This variation reminds us the difference between micro and macro scale cavitation phenomena. Therefore, cavitation number which indicates an index for the cavitation occurrence is considered among the channels. Prior to studying this non-dimensional number, the compressibility of the fluid is taken into account employing Mach number, $Ma = \bar{V}/a$, where a is the speed of sound in the liquid and \bar{V} is the mean velocity computed with use of volume flow

rate measurement of the fluid at the outlet of the channels. The Mach number for all the cases is between 0.019 and 0.1 implying incompressible flow.

The intensity of cavitation along the channel is characterized by cavitation number, $\sigma = (p_{ref} - p_v)/0.5\rho v_{ref}^2$, where p_{ref} is reference pressure which is upstream pressure in this work, p_v is vapor saturation pressure (vapor saturation pressure for the working fluid is approximately 3500 Pa), and v_{ref} is reference velocity which is selected as the mean velocity. Accordingly, the calculated cavitation number for the channels with diameters of 152 and 762 μm are obtained as 0.078 and 0.52 for the upstream pressure of 40 bar, respectively. These numbers imply that the created cavitation bubbles are much more intense in the channels with lower diameters. There is a same trend for the cavitation number in the other injection pressures.

As stated earlier, the spray structure is shown for two most upstream and downstream segments here. The spray structure illustrated in Figure 6.4(a) shows almost the same trend for all of the channels. The presented images in the first row of Figure 6.4 are the first segments of the channels at the upstream pressure of 10 bar. At this pressure, the velocity does not change dramatically once the diameter increases, and also the created cavitation bubbles are not intense for all the channels according to the previous studies. Therefore, the flow regime at this pressure and segment is a liquid jet, but different flow regime is seen when we move further to the downstream of the spray at the last segment. Droplet separation and large perturbation are observed in the last segment of the channel with diameters of 152 μm and, 256 and 504 μm , respectively. Surface tension and, large and small perturbations are observed in the channels with diameters of 256 and 504 μm tends to form the spray jet in the minimal energy condition.

When it comes to the third and fourth row of Figure 6.4 where the upstream pressure increases to 60 bar, we see an entirely different flow regime in the channel with diameter of 762 μm in comparison to other smaller channels for both first and last segments. The most interesting point at this stage is the dramatic spray cloud at the channel with diameter of 504 μm . Here, the droplet/bubble separation is recorded in all the segments exactly from the outlet of the channel to the end of the spray. This fact is getting more interesting when the temperature increases at the higher upstream pressures for the considered channel. Moreover, the calculated

Cavitation numbers for the channels with diameters of 504 and 762 μm are 0.39 and 0.52, respectively for the upstream pressure of 40 *bar*. Therefore, according to the observed flow regime at the outlet of the channels and the measured temperature rise, one can conclude that there is a flow regime variation from micro to mini/macro scale between channels with diameters of 504 and 762 μm . The flow patterns for all the segments of the channels with diameters of 152, 256 and 504 μm contains intense break-ups and droplet/bubble separations which suggests a cloudy spray under the effect of the cavitation, but the entirely different regimes for the all segments of channel with diameter of 762 μm indicate a liquid jet shown in the macro/conventional spray in the literature.

6.3.3 Electric Power Output as a Result of the Heat Generation During the Spray Collision

Once it became evident that the cavitation bubbles creation and collapse heat the surface of a solid interacted with the spray, the idea is developed to harvest the thermal energy and power reclamation for miniature electric appliances. The electrical powers are calculated from temperature differences of sort of physical equations. Firstly, the heat transfer is obtained from the heat energy equation, $q = mc\Delta T$ where q is heat transfer, m the mass of the system, c is the heat capacity and T is the temperature. Then, current is calculated from the Joules Law, $I = \sqrt{q/Res.t}$, where I is the current, Res is the resistance of the solid body, and t is the time step. The current is found for different cases at various upstream pressures. Finally, electric power is acquired from the Ohms Law, $P = Res.I^2$ where P is the electric power, for the mentioned temperature gradients on the solid body.

Figure 6.5 illustrates the calculated electric power for time steps of 30 *seconds*. According to this figure, the maximum reclaimed power is 0.3163 *W* corresponding to the channel with the diameter of 504 μm at the upstream pressure of 40 *bar*, while the minimum power output belongs to the channel with the diameter of 762 μm at the upstream pressure of 10 *bar*. Overall, the highest output electric power is achieved with the channel of the diameter of 504 μm for all of the cases at different conditions. This channel leads to the condition where the severer break-ups and densest spray cloud are seen. The aforementioned power values are in the

range of the required power sources for the miniature electric appliances included in Table 6.1. The reclaimed powers shown in Figure 6.5 are obtained as the preliminary results for the proposed idea and system. It is believed that the outcome of these experiments would help in developing suitable injection conditions and designing an enhanced solid surface according to the predicted research path. The proposed system at this condition is capable of producing the required electric power for approximately three Light-Emitting Diodes and a Digital mini thermometer.

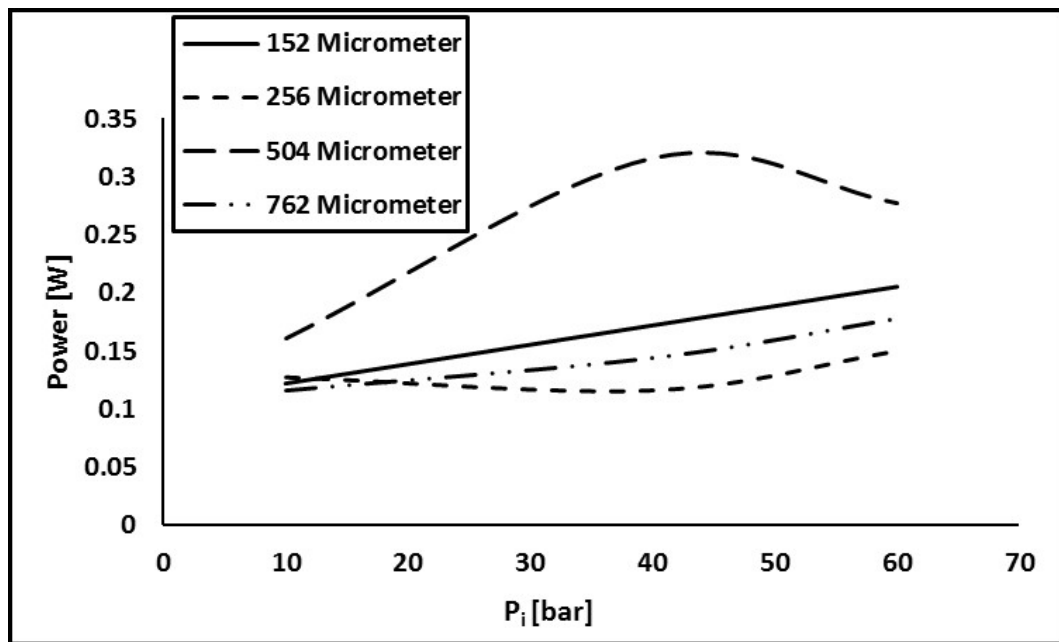


Figure 6.5: The output power produced as a result of the thermal energy creation on a solid surface subjected to the cavitating induced spray

The proposed reclaimed power system offers considerable advantages compared to the energy-harvesting devices in terms of the cost and its easy implementation. The system consists of a reservoir, conventional tubes and micro/mini-channels connecting to each other with suitable fittings available in the local suppliers. A simple solid body is also utilized to gather the thermal energy and convert it to the corresponding electrical power. Therefore, the low-cost of the system preparation and easy manipulation make the system efficient in providing the required power for running the daily-used electric appliances.

Table 6.1: The electrical characteristics of some miniature daily-used energy-harvesting devices

Device Name	Forward Current	Power Dissipation	Plain Water
Light-Emitting Diodes (LEDs)	80 <i>mA</i>	176 <i>mW</i>	16 <i>min</i>
Antenna GPS	12 <i>mA</i>	39.6 <i>mW</i>	4 <i>min</i>
Digital mini thermometer	300 <i>mA</i>	450 <i>mW</i>	40 <i>min</i>
Mini GPS receiver	200 <i>mA</i>	280 <i>mW</i>	30 <i>min</i>
Portable charger for cell phones	1000 <i>mA</i>	1000-5000 <i>mW</i>	100-500 <i>min</i>

Chapter 7

Conclusion

This numerical study emphasizes on significant differences in cavitating flow characteristics between micro-channels and mini-channels. The static pressure drops to negative values in the micro-channels especially in the micro-channel with the inner diameter of $254\ \mu\text{m}$, where tensile stresses are obtained over the whole range of the upstream pressure and extend to the outlet of the channel, whereas there are fewer locations of negative pressures in the mini-channels at a specific upstream pressure. The pressure dramatically decreases near the inlet of the micro-channels implying that the cavitation bubbles form near the inlet of the channel. The vapor phase fills more space at the outlet of the mini-channels. However, the vapor volume fraction has a higher value in the middle of the channel in the micro-channel configurations. The micro-channel with the inner diameter of $254\ \mu\text{m}$ is more appropriate than the micro-channel with the inner diameter of $152\ \mu\text{m}$ from the point of view of the use of cavitation bubbles at the outlet of the micro-channel for the biomedical applications, since vapor phase is present at the outlet across a significant portion of the cross section in the micro-channel with the inner diameter of $254\ \mu\text{m}$. The extensive investigation on the effect of the energy associated with the turbulence shows that the effects of turbulence are significant, and a decrease in the diameter of the channel leads to an increase in shear stress. The cavitation length in micro-channels is different from in mini-channels. Cavitation occurs at lower upstream pressures in mini-channels, and the cavitation length is also longer in mini-channels compared to micro-channels. Furthermore, the velocity profile, particularly near the wall boundaries, affects the vapor phase distribution at the outlet of the micro-

channel. The numerical results show that more cavitation bubbles extended to the outlet of the micro-channel and it increased the possibility of the occurrence of the collapse process.

In this study, spray behavior in cavitating flows downstream of a micro-channel was investigated at different upstream pressures with the use of high speed visualization. Droplet formation at different upstream pressures was studied. Cavitation was generated via sudden pressure drop with the use of a micro-channel with an inner diameter of $152\ \mu\text{m}$. The performed visualization covered a distance of $27.5\ \text{mm}$ from the outlet of the micro-channel. The conical shape of the spray was also visualized via a high speed camera at different regions (Five segments, at distances of 0-5.5, 5.5-11, 11-16.5, 16.5-22 and 22-27.5 mm from the micro-channel outlet) downstream of the micro-channel outlet. The characteristics of resulting droplets were accurately assessed. The observed droplets downstream of the spray were bigger at low upstream pressures. With the increase in the upstream pressure, the droplet size became smaller implying intensified dispersion of bubbles and high energy release of the bubbly cavitating flow at higher pressures. For low pressure values, in the first two segments of the cavitating flows, where the flow has a continuous tube like structure and droplets were not evident, image segmentation was not employed. Starting from the third segment of the flow, accurate segmentation of the droplets was achieved, where droplets had relatively uniform shapes and distributions. With increasing pressure levels, image segmentation could be utilized only in the fourth and fifth segments of the flow, where droplets were more evident. It should be noted that significant oscillations occurred at the start of the first segments of the flow due to the cavitation phenomena. It was also observed that the shape and distribution of the droplets generated at high pressure levels were mostly non-uniform. Cavitation number and flow rate values at various upstream pressures were presented. The flow rates were in a good agreement with previous studies, and Cavitation number had an inverse relationship with pressure. A new correlation for predicting two-phase pressure drop was also developed. Moreover, the fluid flow at the outlet of the micro-channel was classified as discrete droplet flow, liquid jet, jet cavitation, bubbly flow and highly vaporous bubbly flow based on the Cavitation number. The aforementioned flow regimes were observed in different segments for

various upstream pressures. The detailed visualization and analysis of spray structure at the outlet of the micro-channel show that even three different regimes may occur at a constant pressure for some cases.

In this study, the bubble collapse process was captured at high upstream pressures, and this event took place within 12.6 and 3 *ms* for 100 and 120 *bar*, respectively. At high pressures, the spray had a more conical form. The bubble collapse occurred inside the micro-channel at every pressure, but at higher pressures more collapse processes could be captured at the exit. Spray visualization was carried out at a distance of 4.5 *mm* from the tip of the micro-channel using the high speed visualization system. The experimental results showed that the spray cone angle increased with upstream pressure, and beyond the upstream pressure of 50 *bar*, the liquid jet flow changed to the cloudy spray flow. The bubble collapse was recorded at upstream pressures of 100 and 120 *bar*, where the cavitation bubbles extended to the outlet of the micro-channel, and their collapse took place around the spray.

We have revealed that the cavitation phenomenon has the capability to increase the temperature on a surface body with the exposure of the emerging spray at the outlet of the micro/mini-channels. The preliminary results on the collision of the spray on the surface of an aluminum plate shows a temperature rise range between 2.3 and 5.7 °C for all the cases. These temperature variations generate thermal energy of maximum 3.3 *J* and output electric power of 0.3215 *W* at its highest magnitude which is enough for operating miniature electrical appliances. The visual experiments on the spray structure also indicates an interesting trend for the cavitating flow regime from micro to macro scale for the channels. The observations show that the spray has a conical shape with ascending cone angle value for channels with diameter of 152 to 504 μm where the highest temperature increase is recorded. In addition, the cavitating flow parameters and features such as break-ups and bubble/droplet separations are visualized at these channels, while the spray structure at the outlet of the channel with diameter of 762 μm is totally different and presents a non-conical spray jet for all the segments. The overall consideration in the flow pattern and temperature increase suggest thermal energy generation and electrical energy production for all the micro/mini-channels induced by cavitation. We believe that the enhancement in the design of the surface subjected to the spray

exposure could be easily achieved with the optimization of the approach. Moreover, the approach could be converted to a compact micro energy generating device to fullfill individual energy needs.

Chapter 8

Recommendations for Future Research

The data in the literature emphasize on the importance of cavitation phenomenon generated by both ultrasonic and hydrodynamic sources and its potential applications in biomedical sciences. Today, the clinical use and efficacy of ultrasound cavitation are well established, particularly in urinary stones treatment. Alternatively, hydrodynamic cavitation has been recently considered as an emerging research area in biomedical applications, and its efficacy on cell disruption, water disinfection and urinary stones treatment is proven in *In vitro* studies. However, as discussed above, *In vivo* implementation of hydrodynamic cavitation has some limitations, and its clinical use is still not available. Therefore, further investigations are needed to better characterize the physical properties, bubble dynamics and the effects of bubble collapse on tissue or organ system. More precise definition of optimum surgical conditions in hydrodynamic cavitation procedure is required for preventing undesirable consequences. On top of all these, hydrodynamic cavitation should also be tested in other areas such as drug delivery or diagnosis to reveal full potential of this technique. Overall, it is likely that hydrodynamic cavitation offers a substantial promise for biomedical applications.

The assessment of size effects is vital for the design and development of new generation microfluidic devices involving phase change. Additionally, as the length scale reduces, surface nuclei dominate and dictate cavitation events, more cavitation bubbles create, and more rupture occur. Furthermore, surface roughness (hydropho-

bic surfaces) and pressure pulses as a result of nanomechanical oscillations increase the performance of the micro/nanochannels providing higher cavitation bubbles and therefore, more energy from the rupture of the bubbles.

Therefore, a challenging issue is raising when the size scale and roughness matter are taken into account. A complete pack of a recommendation is as follows for defining a comprehensive research project:

(i) fabricate a micro/nano device providing cavitation patterns for different geometries/dimensions/roughness

(ii) demonstrate energy utilization from the collapse process

(iii) boiling effect on the cavitation creation and collapse

(iv) nanomechanical vibration effect on droplet separation/bubbles creation.

A preliminary feature of such a system is shown in Figure 8.1:

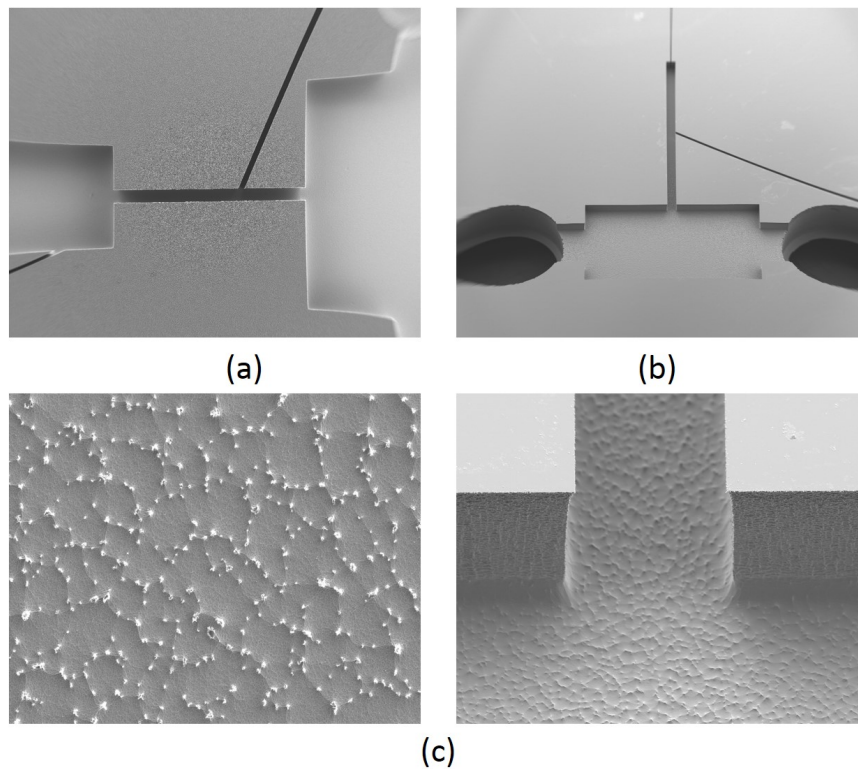


Figure 8.1: Design and surface behavior of the recommended system. (a) Overall structure of the cavitating nozzle vibrator (b) The extended channels to study the collapse and interaction between solid-fluid-bubble (c) Surface roughness indication

Within the scope of this study, novel information about the cavitating flow regimes and spray at the outlet of the micro/mini-channels were gathered. The approach proposed in this study for both internal flow characteristics and spray

behavior could be applied to the field of the interaction between fluid and solid. One can consider the spray emergence as the fluid phase and focus on the interaction between the emerged spray and the targeted area. Preliminary investigations on the interaction between the spray and some targeted surface were carried out during our recent experiments as shown in Figure 8.2. The targeted surface was chosen among the investigated abnormal stones and tissues such as kidney stone and prostate tissue. Figure 8.2 illustrates three different images with specific lenses at different upstream pressures and time steps as indicated in the figure.

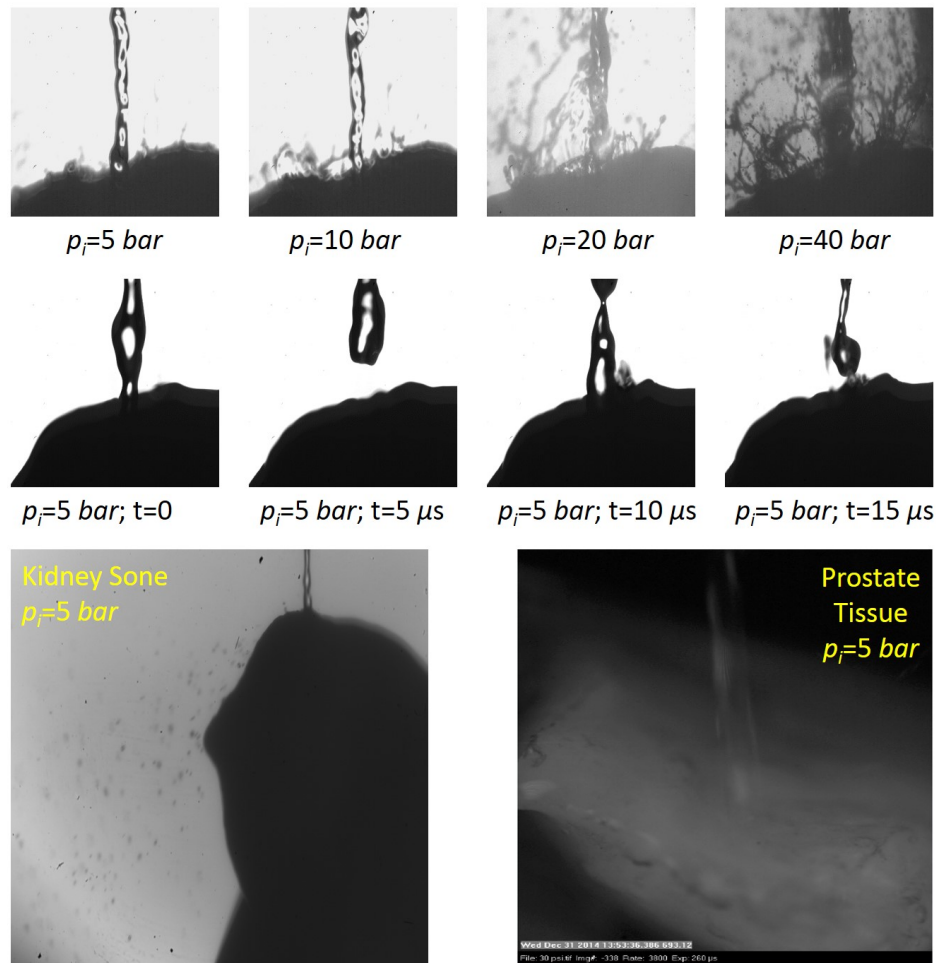


Figure 8.2: The interaction between spray and the targeted areas at different conditions for kidney stone and prostate tissue

The interaction between the solid and liquid is considered as a big issue in the field of fluid dynamics. In addition to the classic problems in conventional scale, two factor namely; Size reduction and material type (abnormal stone and tissue) make the problem complex and worthy to follow it and manifest the complex mechanisms

behind it.

References

- [1] L. Rayleigh, “Viii. on the pressure developed in a liquid during the collapse of a spherical cavity,” *The London, Edinburgh, and Dublin Philosophical Magazine and Journal of Science*, vol. 34, no. 200, pp. 94–98, 1917.
- [2] M. S. Plesset, “The dynamics of cavitation bubbles,” *Journal of Applied Mechanics*, vol. 16, pp. 277–282, 1949.
- [3] R. E. A. Arndt, “Cavitation in fluid machinery and hydraulic structures,” *Annual Review of Fluid Mechanics*, vol. 13, no. 1, pp. 273–326, 1981.
- [4] T. Leighton, “9 the principles of cavitation,” *Ultrasound in Food Processing*, p. 151, 1995.
- [5] W. H. Nurick, “Orifice cavitation and its effect on spray mixing,” *Journal of Fluids Engineering*, vol. 98, no. 4, pp. 681–687, 1976.
- [6] V. S. Moholkar, P. S. Kumar, and A. B. Pandit, “Hydrodynamic cavitation for sonochemical effects,” *Ultrasonics Sonochemistry*, vol. 6, no. 1, pp. 53–65, 1999.
- [7] M. Schlender, A. Spengler, and H. P. Schuchmann, “High-pressure emulsion formation in cylindrical coaxial orifices: Influence of cavitation induced pattern on oil drop size,” *International Journal of Multiphase Flow*, vol. 74, pp. 84–95, 2015.
- [8] F. Payri, R. Payri, F. Salvador, and J. Martinez-Lopez, “A contribution to the understanding of cavitation effects in diesel injector nozzles through a combined experimental and computational investigation,” *Computers Fluids*, vol. 58, pp. 88–101, 2012.

- [9] J. Desantes, R. Payri, F. Salvador, and J. D. la Morena, “Influence of cavitation phenomenon on primary break-up and spray behavior at stationary conditions,” *Fuel*, vol. 89, no. 10, pp. 3033–3041, 2010.
- [10] A. Sou, S. Hosokawa, and A. Tomiyama, “Effects of cavitation in a nozzle on liquid jet atomization,” *International Journal of Heat and Mass Transfer*, vol. 50, no. 17-18, pp. 3575–3582, 2007.
- [11] M. D. Giorgi, A. Ficarella, and M. Tarantino, “Evaluating cavitation regimes in an internal orifice at different temperatures using frequency analysis and visualization,” *International Journal of Heat and Fluid Flow*, vol. 39, pp. 160–172, 2013.
- [12] M. Perpar, E. Polutnik, M. Pecar, and I. Zun, “Bubbly structures in a cavitating slot orifice,” *Experimental Thermal and Fluid Science*, vol. 53, pp. 57–69, 2014.
- [13] M. E. Henry and S. H. Collicott, “Visualization of internal flow in a cavitating slot orifice,” *Atomization and Sprays*, vol. 10, no. 6, 2000.
- [14] A. Cioncolini, F. Scenini, and J. Duff, “Micro-orifice single-phase liquid flow: Pressure drop measurements and prediction,” *Experimental Thermal and Fluid Science*, vol. 65, pp. 33 – 40, 2015.
- [15] J. Rooze, M. A. and G.-J. S. van der Gulik, D. Fernandez-Rivas, J. G. E. Gardeni, E. V. Rebrov, J. C. Schouten, and J. T. F. Keurentjes, “Hydrodynamic cavitation in micro channels with channel sizes of 100 and 750 micrometers,” *Microfluidics and Nanofluidics*, vol. 12, no. 1, pp. 499–508, 2012.
- [16] C. Mishra and Y. Peles, “Cavitation in flow through a micro-orifice inside a silicon microchannel,” *Physics of Fluids (1994-present)*, vol. 17, no. 1, pp. 013601–013615, 2005.
- [17] A. Koşar, O. Oral, Z. Itah, D. Gozuacik *et al.*, “Bubbly cavitating flow generation and investigation of its erosional nature for biomedical applications,” *Biomedical Engineering, IEEE Transactions on*, vol. 58, no. 5, pp. 1337–1346, 2011.

- [18] O. Y. Perk, M. Şeşen, D. Gozuacik, and A. Koşar, “Kidney stone erosion by micro scale hydrodynamic cavitation and consequent kidney stone treatment,” *Annals of biomedical engineering*, vol. 40, no. 9, pp. 1895–1902, 2012.
- [19] Z. Itah, O. Oral, O. Y. Perk, M. Sesen, E. Demir, S. Erbil, A. I. Dogan-Ekici, S. Ekici, A. Kosar, and D. Gozuacik, “Hydrodynamic cavitation kills prostate cells and ablates benign prostatic hyperplasia tissue,” *Experimental Biology and Medicine*, p. 1535370213503273, 2013.
- [20] B. K. Türköz, A. Zakhariouta, M. Sesen, A. Taralp, and A. Koşar, “Reversibility of functional and structural changes of lysozyme subjected to hydrodynamic flow,” *Journal of Nanotechnology in Engineering and Medicine*, vol. 3, no. 1, p. 011006, 2012.
- [21] A. P. Keller, “Cavitation scale effects-empirically found relations and the correlation of cavitation number and hydrodynamic coefficients,” In *CAV 2001 4th International Symposium Cavitation, Pasadena, CA, USA*, 2001.
- [22] G. L. Morini, “Single-phase convective heat transfer in microchannels: A review of experimental results,” *International Journal of Thermal Science*, vol. 43, pp. 631–651.
- [23] G. M. Mala and D. Li, “Flow characteristics of water in microtubes,” *International Journal of Heat and Fluid Flow*, vol. 20, no. 2, pp. 142–148, 1999.
- [24] P. Garstecki, A. M. Ganan-Calvo, and G. M. Whitesides, “Formation of bubbles and droplets in microfluidic systems,” *Bulletin of the Polish Academy of Sciences Technical Sciences*, vol. 53, pp. 361–372, 2005.
- [25] R. Xiong and J. N. Chung, “An experimental study of the size effect on adiabatic gas-liquid two-phase flow patterns and void fraction in microchannels,” *Physics of Fluids*, vol. 19, no. 3, 2007.
- [26] T. Cubaud, M. Tatineni, X. Zhong, and C.-M. Ho, “Bubble dispenser in microfluidic devices,” *Physical Review E*, vol. 72, p. 037302, Sep 2005.

- [27] M. T. Shervani-Tabar, S. Parsa, and M. Ghorbani, “Numerical study on the effect of the cavitation phenomenon on the characteristics of fuel spray,” *Mathematical and Computer Modelling*, vol. 56, no. 56, pp. 105–117, 2012.
- [28] M. T. Shervani-Tabar, M. Sheykhvazayefi, and M. Ghorbani, “Numerical study on the effect of the injection pressure on spray penetration length,” *Applied Mathematical Modelling*, vol. 37, no. 14-15, pp. 7778–7788, 2013.
- [29] M. Ghorbani, M. Yildiz, D. Gozuacik, and A. Kosar, “Cavitating nozzle flows in micro- and minichannels under the effect of turbulence,” *Journal of Mechanical Science and Technology*, vol. 30, no. 6, pp. 2565–2581, 2016.
- [30] X. Wang, G. Zhu, and K. Li, “A phenomenological bubble number density model developed for simulation of cavitating flows inside high-pressure diesel injection nozzles,” *International Journal of Numerical Methods for Heat & Fluid Flow*, vol. 23, no. 8, pp. 1356–1372, 2013.
- [31] A. Sou, B. Bier, and A. Tomiyama, “Numerical simulation of incipient cavitation flow in a nozzle of fuel injector,” *Computers & Fluids*, vol. 103, pp. 42 – 48, 2014.
- [32] N. Dietrich, S. Poncin, N. Midoux, and H. Z. Li, “Bubble formation dynamics in various flow-focusing microdevices,” *Langmuir*, vol. 24, no. 24, pp. 13 904–13 911, 2008.
- [33] M. Jia, M. Xie, H. Liu, W.-H. Lam, and T. Wang, “Numerical simulation of cavitation in the conical-spray nozzle for diesel premixed charge compression ignition engines,” *Fuel*, vol. 90, no. 8, pp. 2652–2661, 2011.
- [34] M. Battistoni and C. N. Grimaldi, “Numerical analysis of injector flow and spray characteristics from diesel injectors using fossil and biodiesel fuels,” *Applied Energy*, vol. 97, pp. 656 – 666, 2012.
- [35] S. Shibata, S. Nishio, A. Sou, D. Akayama, and M. Mashida, “Evaluation of cavitation in injector nozzle and correlation with liquid atomization,” *Journal of Visualization*, vol. 18, no. 3, pp. 481–492, 2015.

- [36] B. Bicer and A. Sou, “Application of the improved cavitation model to turbulent cavitating flow in fuel injector nozzle,” *Applied Mathematical Modelling*, vol. 40, no. 78, pp. 4712–4726, 2016.
- [37] R. Payri, S. Ruiz, J. Gimeno, and P. Marti-Aldarav, “Verification of a new {CFD} compressible segregated and multi-phase solver with different flux updates-equations sequences,” *Applied Mathematical Modelling*, vol. 39, no. 2, pp. 851–861, 2015.
- [38] H. Kanfoudi and R. Zgolli, “Modeling and computation of the cavitating flow in injection nozzle holes,” *International Journal of Modeling, Simulation, and Scientific Computing*, vol. 06, no. 01, p. 1550003, 2015.
- [39] B. Bicer and A. Sou, “Bubble dynamics model for predicting the growth and col-lapse of cavitation bubbles in diesel injector,” *Atomization and Sprays*, vol. 24, no. 10, pp. 915–935, 2014.
- [40] C. Zhu, M. Ertl, and B. Weigand, “Numerical investigation on the primary breakup of an inelastic non-newtonian liquid jet with inflow turbulence,” *Physics of Fluids*, vol. 25, no. 8, 2013.
- [41] L. Postrioti, S. Malaguti, M. Bosi, G. Buitoni, S. Piccinini, and G. Bagli, “Experimental and numerical characterization of a direct solenoid actuation injector for diesel engine applications,” *Fuel*, vol. 118, pp. 316 – 328, 2014.
- [42] M. Gavaises, F. Villa, P. Koukouvinis, M. Marengo, and J.-P. Franc, “Visualisation and les simulation of cavitation cloud formation and collapse in an axisymmetric geometry,” *International Journal of Multiphase Flow*, vol. 68, pp. 14–26, 2015.
- [43] B. Dollet, W. van Hoeve, J.-P. Raven, P. Marmottant, and M. Versluis, “Role of the channel geometry on the bubble pinch-off in flow-focusing devices,” *Physical Review Letters*, vol. 100, p. 034504, 2008.
- [44] Z. Che, N.-T. Nguyen, and T. N. Wong, “Hydrodynamically mediated breakup of droplets in microchannels,” *Applied Physics Letters*, vol. 98, no. 5, 2011.

- [45] A. K. Agarwal, S. Som, P. C. Shukla, H. Goyal, and D. Longman, “In-nozzle flow and spray characteristics for mineral diesel, karanja, and jatropha biodiesels,” *Applied Energy*, vol. 156, pp. 138–148, 2015.
- [46] Z. He, G. Guo, X. Tao, W. Zhong, X. Leng, and Q. Wang, “Study of the effect of nozzle hole shape on internal flow and spray characteristics,” *International Communications in Heat and Mass Transfer*, vol. 71, pp. 1–8, 2016.
- [47] C. Baumgarten, “Mixture formation in internal combustion engines,” *Springer-Verlag Berlin Heidelberg*, 2006.
- [48] R. Payri, F. J. Salvador, J. Gimeno, and J. de la Morena, “Study of cavitation phenomena based on a technique for visualizing bubbles in a liquid pressurized chamber,” *International Journal of Heat and Fluid Flow*, vol. 30, no. 4, pp. 768–777, 2009.
- [49] B. W. Chandra and S. H. Collicott, “Experimental investigation of cavitation frequency in a slot orifice,” *12th Annual Conference of ILASS*, 1999.
- [50] K. Sato and Y. Saito, “Unstable cavitation behavior in a circular cylindrical orifice flow,” *CAV 2001 : Fourth International Symposium on Cavitation, June 20-23, 2001, California Institute of Technology, Pasadena, CA USA 18*, 2001.
- [51] C. Stanley, T. Barber, and G. Rosengarten, “Re-entrant jet mechanism for periodic cavitation shedding in a cylindrical orifice,” *International Journal of Heat and Fluid Flow*, vol. 50, pp. 169–176, 2014.
- [52] A. Cervone, C. Bramanti, E. Rapposelli, and L. d’Agostino, “Thermal cavitation experiments on a naca 0015 hydrofoil,” *ASME Journal of Fluids Engineering*, vol. 128, pp. 326–331, 2005.
- [53] R. Payri, F. Salvador, J. Gimeno, and O. Venegas, “Study of cavitation phenomenon using different fuels in a transparent nozzle by hydraulic characterization and visualization,” *Experimental Thermal and Fluid Science*, vol. 44, pp. 235–244, 2013.

- [54] A. Kravtsova, D. Markovich, K. Pervunin, M. Timoshevskiy, and K. Hanjali, “High-speed visualization and {PIV} measurements of cavitating flows around a semi-circular leading-edge flat plate and {NACA0015} hydrofoil,” *International Journal of Multiphase Flow*, vol. 60, pp. 119–134, 2014.
- [55] T. Naoe and M. Futakawa, “Optically observation of mercury cavitation bubble collapsing,” *Experimental Thermal and Fluid Science*, vol. 44, pp. 550–555, 2013.
- [56] K. S. Suslick and D. J. Flannigan, “Inside a collapsing bubble: Sonoluminescence and the conditions during cavitation,” *Annual Review of Physical Chemistry*, vol. 59, pp. 659–683, 2008.
- [57] H. M. Xiong, D. Shchukin, H. Mohwald, Y. Xu, and Y. Y. Xia, “Sonochemical synthesis of highly luminescent zinc oxide nanoparticles doped with magnesium(ii),” *Angewandte Chemie*, vol. 121, pp. 2765–2769, 2009.
- [58] V. Belova-Magri, A. Brotchie, C. Cairos, R. Mettin, and H. Mohwald, “Micropatterning for the control of surface cavitation: Visualization through high-speed imaging,” *ACS Applied Materials & Interfaces*, vol. 7, no. 7, pp. 4100–4108, 2015.
- [59] J. W. Holl, “Nuclei and cavitation,” *ASME Journal of Basic Engineering*, vol. 92, pp. 681–688, 1970.
- [60] R. T. Knapp, J. W. Daily, and Hammit, “Cavitation,” *McGraw-Hill, New York*, 1970.
- [61] B. Ran and J. Katz, “The response of microscopic bubbles to sudden changes in the ambient pressure,” *Journal of Fluid Mechanics*, vol. 224, pp. 91–115, 1991.
- [62] F. G. Hammit and M. K. De, “Cavitation damage prediction,” *Wear*, vol. 52, pp. 243–262, 1979.
- [63] C. E. Brennen, “Cavitation and bubble dynamics,” *Oxford University Press, Oxford, UK*, 1995.

- [64] F. Payri, V. Bermdez, R. Payri, and F. Salvador, “The influence of cavitation on the internal flow and the spray characteristics in diesel injection nozzles,” *Fuel*, vol. 83, no. 4-5, pp. 419–431, 2004.
- [65] L. Martinez, A. Benkenida, and B. Cuenot, “A model for the injection boundary conditions in the context of 3d simulation of diesel spray: Methodology and validation,” *Fuel*, vol. 89, no. 1, pp. 219–228, 2010.
- [66] K. Komada, N. Kawaharada, D. Sakaguchi, H. Ueki, and M. Ishida, “Evaluation of mass flow rate distribution in diesel fuel spray by l2f,” *Proceedings of the ASME Internal Combustion Engine Division Fall Technical Conference (ICEF)*, no. 1, pp. 213–222, 2012.
- [67] J. Kong and C. Bae, “Effect of nozzle hole geometry on non-evaporating diesel spray characteristics at high-pressure injection,” *Atomization and Sprays*, vol. 22, no. 1, pp. 1–21, 2012.
- [68] K. S. Im, S. K. Cheong, C. F. Powell, and M. C. L. J. Wang, “Unraveling the geometry dependence of in-nozzle cavitation in high-pressure injectors,” *Nature, Scientific Report*, no. 3, p. 2067, 2013.
- [69] H. Liao, R. Chen, L. Wang, and L. Zhu, “Effect of impacting distance and confining pressure on cavitation bubble collapse characteristics,” *Atomization and Sprays*, vol. 23, no. 3, pp. 249–264, 2013.
- [70] F. Xiao, M. Dianat, and J. J. McGuirk, “Large eddy simulation of liquid-jet primary breakup in air crossflow,” *AIAA Journal*, no. 51, pp. 2878–2893, 2013.
- [71] O. Desjardins, J. McCaslin, M. Owkes, and P. Brady, “Direct numerical and largeeddy simulation of primary at-omization in complex geometries,” *Atomization and Sprays*, vol. 23, no. 11, pp. 1001–1048, 2013.
- [72] B. Balewski, B. Heine, and C. Tropea, “Experimental investigation of the correlation between nozzle flow and spray using laser doppler velocimeter, phase dop-pler system, high-speed photography, and x-ray radiography,” vol. 20, no. 1, pp. 57–70, 2010.

- [73] S. Hossainpour and A. Binesh, “Investigation of fuel spray atomization in a {DI} heavy-duty diesel engine and comparison of various spray breakup models,” *Fuel*, vol. 88, no. 5, pp. 799–805, 2009.
- [74] J. J. Escobar-Chávez, I. M. Rodríguez-Cruz, and C. L. Domínguez-Delgado, *Chemical and Physical Enhancers for Transdermal Drug Delivery*. INTECH Open Access Publisher, 2012. [Online]. Available: <http://www.intechopen.com/books/pharmacology/chemical-and-physical-enhancers-for-transdermal-drug-delivery>
- [75] L. Qin, P. Fok, H. Lu, S. Shi, Y. Leng, and K. Leung, “Low intensity pulsed ultrasound increases the matrix hardness of the healing tissues at bone–tendon insertions: a partial patellectomy model in rabbits,” *Clinical Biomechanics*, vol. 21, no. 4, pp. 387–394, 2006.
- [76] H. El-Mowafi and M. Mohsen, “The effect of low-intensity pulsed ultrasound on callus maturation in tibial distraction osteogenesis,” *International orthopaedics*, vol. 29, no. 2, pp. 121–124, 2005.
- [77] S. R. Angle, K. Sena, D. R. Sumner, and A. S. Viridi, “Osteogenic differentiation of rat bone marrow stromal cells by various intensities of low-intensity pulsed ultrasound,” *Ultrasonics*, vol. 51, no. 3, pp. 281–288, 2011.
- [78] J. E. Lingeman, J. A. McAteer, E. Gnessin, and A. P. Evan, “Shock wave lithotripsy: advances in technology and technique,” *Nature Reviews Urology*, vol. 6, no. 12, pp. 660–670, 2009.
- [79] T. Sauerbruch, M. Delius, J. Holl, O. Wess, W. Weber, W. Hepp, W. Brendel, and G. Paumgartner, “Fragmentation of allstones in humans by extracorporeal shock-wave treatment,” in *Hepatology*, vol. 5, no. 5. WB Saunders CO Independence Square West Curtis Center, STE 300, Philadelphia, PA 19106-3399, 1985, pp. 977–977.
- [80] W. Sass, M. Bräunlich, H. P. Dreyer, E. Matura, W. Folberth, H. G. Priesmeyer, and J. Seifert, “The mechanisms of stone disintegration by shock waves,” *Ultrasound in medicine & biology*, vol. 17, no. 3, pp. 239–243, 1991.

- [81] N. G. Holmer, L. O. Almquist, T. G. Hertz, A. Holm, E. Lindstedt, H. W. Persson, and C. H. Hertz, "On the mechanism of kidney stone disintegration by acoustic shock waves," *Ultrasound in medicine & biology*, vol. 17, no. 5, pp. 479–489, 1991.
- [82] C. H. Chaussy, W. Brendel, and E. Schmiedt, "Extracorporeally induced destruction of kidney stones by shock waves," *The Lancet*, vol. 316, no. 8207, pp. 1265–1268, 1980.
- [83] S. CD, Jr, L. JC, D. AW, and et al, "Comparative effectiveness of shock wave lithotripsy and ureteroscopy for treating patients with kidney stones," *JAMA Surgery*, vol. 149, no. 7, pp. 648–653, 2014. [Online]. Available: [+http://dx.doi.org/10.1001/jamasurg.2014.336](http://dx.doi.org/10.1001/jamasurg.2014.336)
- [84] H. Wu, J. Wang, J. Lu, Y. Wang, and Z. Niu, "Treatment of renal stones 20 mm with extracorporeal shock wave lithotripsy," *Urologia Internationalis*, vol. 96, no. 6, pp. 99–105, 2016.
- [85] J. V. Kaude, C. M. Williams, M. R. Millner, K. N. Scott, and B. Finlayson, "Renal morphology and function immediately after extracorporeal shock-wave lithotripsy," *American journal of roentgenology*, vol. 145, no. 2, pp. 305–313, 1985.
- [86] L. Howle, D. G. Schaeffer, M. Shearer, and P. Zhong, "Lithotripsy: the treatment of kidney stones with shock waves," *SIAM review*, vol. 40, no. 2, pp. 356–371, 1998.
- [87] J. H. Parks, F. L. Coe, A. P. Evan, and E. M. Worcester, "Urine ph in renal calcium stone formers who do and do not increase stone phosphate content with time," *Nephrology dialysis transplantation*, vol. 24, no. 1, pp. 130–136, 2009.
- [88] J. C. W. Jr., T. Hameed, M. E. Jackson, S. Aftab, A. Gambaro, Y. A. Pishchalnikov, J. E. Lingeman, and J. A. McAteer, "Fragility of brushite stones in shock wave lithotripsy: Absence of correlation with computerized tomography visible structure," *The Journal of Urology*,

- vol. 188, no. 3, pp. 996 – 1001, 2012. [Online]. Available: <http://www.sciencedirect.com/science/article/pii/S0022534712036543>
- [89] R. Pramanik, J. R. Asplin, M. E. Jackson, and J. C. Williams, “Protein content of human apatite and brushite kidney stones: significant correlation with morphologic measures,” *Urological Research*, vol. 36, no. 5, pp. 251–258, 2008.
- [90] R. Kacker, J. J. Meeks, L. Zhao, and R. B. Nadler, “Decreased stone-free rates after percutaneous nephrolithotomy for high calcium phosphate composition kidney stones,” *The Journal of urology*, vol. 180, no. 3, pp. 958–960, 2008.
- [91] A. P. Evan, F. L. Coe, B. A. Connors, R. K. Handa, J. E. Lingeman, and E. M. Worcester, “Mechanism by which shock wave lithotripsy can promote formation of human calcium phosphate stones,” *American Journal of Physiology - Renal Physiology*, vol. 308, no. 8, pp. F938–F949, 2015.
- [92] L. A. Crum, “Cavitation microjets as a contributory mechanism for renal calculi disintegration in eswl.” *The Journal of urology*, vol. 140, no. 6, pp. 1587–1590, 1988.
- [93] G. Delacretaz, K. Rink, G. Pittomvils, J. Lafaut, H. Vandeursen, and R. Boving, “Importance of the implosion of eswl-induced cavitation bubbles,” *Ultrasound in medicine & biology*, vol. 21, no. 1, pp. 97–103, 1995.
- [94] K. Z. Sheir, T. A. El-Diasty, and A. M. Ismail, “Evaluation of a synchronous twin-pulse technique for shock wave lithotripsy: the first prospective clinical study,” *BJU international*, vol. 95, no. 3, pp. 389–393, 2005.
- [95] G. Canseco, M. de Icaza-Herrera, F. Fernández, and A. M. Loske, “Modified shock waves for extracorporeal shock wave lithotripsy: a simulation based on the gilmore formulation,” *Ultrasonics*, vol. 51, no. 7, pp. 803–810, 2011.
- [96] A. M. Loske, J. Campos-Guillen, F. Fernández, and E. Castaño-Tostado, “Enhanced shock wave-assisted transformation of escherichia coli,” *Ultrasound in medicine & biology*, vol. 37, no. 3, pp. 502–510, 2011.

- [97] A. M. Loske, F. Fernández, H. Zendejas, M. Paredes, and E. Castaño-Tostado, “Dual pulse shock wave lithotripsy: in vitro and in vivo study,” *The Journal of urology*, vol. 174, no. 6, pp. 2388–2392, 2005.
- [98] A. M. Loske, F. E. Prieto, F. Fernández, and J. van Cauwelaert, “Tandem shock wave cavitation enhancement for extracorporeal lithotripsy,” *Physics in medicine and biology*, vol. 47, no. 22, p. 3945, 2002.
- [99] U. M. Álvarez, A. Ramírez, F. Fernández, A. Méndez, and A. M. Loske, “The influence of single-pulse and tandem shock waves on bacteria,” *Shock Waves*, vol. 17, no. 6, pp. 441–447, 2008.
- [100] X. Xi and P. Zhong, “Improvement of stone fragmentation during shock-wave lithotripsy using a combined eh/peaa shock-wave generator?in vitro experiments,” *Ultrasound in medicine & biology*, vol. 26, no. 3, pp. 457–467, 2000.
- [101] P. Zhong, X. Xi, S. Zhu, F. H. Cocks, and G. M. Preminger, “Recent developments in swl physics research,” *Journal of endourology*, vol. 13, no. 9, pp. 611–617, 1999.
- [102] F. Fernández, G. Fernández, and A. M. Loske, “Treatment time reduction using tandem shockwaves for lithotripsy: an in vivo study,” *Journal of Endourology*, vol. 23, no. 8, pp. 1247–1253, 2009.
- [103] P. Lukes, P. Sunka, P. Hoffer, V. Stelmashuk, P. Pouckova, M. Zadinova, J. Zeman, L. Dibdiak, H. Kolarova, K. Tomankova, S. Binder, and J. Benes, “Focused tandem shock waves in water and their potential application in cancer treatment,” *Shock Waves*, vol. 24, no. 1, pp. 51–57, 2013.
- [104] A. M. Loske, F. Fernández, D. Magaa-Ortiz, N. Coconi-Linares, E. Ortiz-Vzquez, and M. A. Gmez-Lim, “Tandem shock waves to enhance genetic transformation of aspergillus niger,” *Ultrasonics*, vol. 54, no. 6, pp. 1656 – 1662, 2014.
- [105] M. de Icaza-Herrera, F. Fernández, and A. M. Loske, “Combined short and long-delay tandem shock waves to improve shock wave lithotripsy according to the gilmoreaikulichev theory,” *Ultrasonics*, vol. 58, pp. 53 – 59, 2015.

- [106] S. Zhu and P. Zhong, “Shock wave–inertial microbubble interaction: A theoretical study based on the gilmore formulation for bubble dynamics,” *The Journal of the Acoustical Society of America*, vol. 106, no. 5, pp. 3024–3033, 1999.
- [107] J. C. Williams, M. A. Stonehill, K. Colmenares, A. P. Evan, S. P. Andreoli, R. O. Cleveland, M. R. Bailey, L. A. Crum, and J. A. McAteer, “Effect of macroscopic air bubbles on cell lysis by shock wave lithotripsy in vitro,” *Ultrasound in medicine & biology*, vol. 25, no. 3, pp. 473–479, 1999.
- [108] T. Ikeda, S. Yoshizawa, M. Tosaki, J. S. Allen, S. Takagi, N. Ohta, T. Kitamura, and Y. Matsumoto, “Cloud cavitation control for lithotripsy using high intensity focused ultrasound,” *Ultrasound in medicine & biology*, vol. 32, no. 9, pp. 1383–1397, 2006.
- [109] S. Yoshizawa, T. Ikeda, A. Ito, R. Ota, S. Takagi, and Y. Matsumoto, “High intensity focused ultrasound lithotripsy with cavitating microbubbles,” *Medical & biological engineering & computing*, vol. 47, no. 8, pp. 851–860, 2009.
- [110] E. Johnsen and T. Colonius, “Numerical simulations of non-spherical bubble collapse,” *Journal of fluid mechanics*, vol. 629, pp. 231–262, 2009.
- [111] ———, “Shock-induced collapse of a gas bubble in shockwave lithotripsy,” *The Journal of the Acoustical Society of America*, vol. 124, no. 4, pp. 2011–2020, 2008.
- [112] Y. A. Pishchalnikov, O. A. Sapozhnikov, M. R. Bailey, J. C. Williams Jr, R. O. Cleveland, T. Colonius, L. A. Crum, A. P. Evan, and J. A. McAteer, “Cavitation bubble cluster activity in the breakage of kidney stones by lithotripter shockwaves,” *Journal of Endourology*, vol. 17, no. 7, pp. 435–446, 2003.
- [113] E. Fuh, G. E. Haleblian, R. D. Norris, W. D. M. Albala, N. Simmons, P. Zhong, and G. M. Preminger, “The effect of frequency doubled double pulse nd: Yag laser fiber proximity to the target stone on transient cavitation and acoustic emission,” *The Journal of urology*, vol. 177, no. 4, pp. 1542–1545, 2007.

- [114] M. Calvisi, J. Illoreta, and A. Szeri, “Dynamics of bubbles near a rigid surface subjected to a lithotripter shock wave. part 2. reflected shock intensifies non-spherical cavitation collapse,” *Journal of Fluid Mechanics*, vol. 616, pp. 63–97, 2008.
- [115] J. A. Rooney, “Hydrodynamic shearing of biological cells,” *Journal of Biological Physics*, vol. 2, no. 1, pp. 26–40, 1974.
- [116] J. A. Roney, “Shear as a mechanism for sonically induced biological effects,” *The Journal of the Acoustical Society of America*, vol. 52, no. 6B, pp. 1718–1724, 1972.
- [117] D. Palanker, A. Vankov, J. Miller, M. Friedman, and M. Strauss, “Prevention of tissue damage by water jet during cavitation,” *Journal of applied physics*, vol. 94, no. 4, pp. 2654–2661, 2003.
- [118] I. Toytman, A. Silbergleit, D. Simanovski, and D. Palanker, “Multifocal laser surgery: Cutting enhancement by hydrodynamic interactions between cavitation bubbles,” *Physical Review E*, vol. 82, no. 4, p. 046313, 2010.
- [119] L. B. Feril, T. Kondo, Z.-G. Cui, Y. Tabuchi, Q.-L. Zhao, H. Ando, T. Misaki, H. Yoshikawa, and S.-i. Umemura, “Apoptosis induced by the sonomechanical effects of low intensity pulsed ultrasound in a human leukemia cell line,” *Cancer letters*, vol. 221, no. 2, pp. 145–152, 2005.
- [120] E.-A. Brujan, “Cardiovascular cavitation,” *Medical engineering & physics*, vol. 31, no. 7, pp. 742–751, 2009.
- [121] C. C. Wen and S. Y. Nakada, “Treatment selection and outcomes: renal calculi,” *Urologic Clinics of North America*, vol. 34, no. 3, pp. 409–419, 2007.
- [122] B. A. Connors, A. P. Evan, L. R. Willis, P. M. Blomgren, J. E. Lingeman, and N. S. Fineberg, “The effect of discharge voltage on renal injury and impairment caused by lithotripsy in the pig,” *Journal of the American Society of Nephrology*, vol. 11, no. 2, pp. 310–318, 2000.

- [123] J. A. McAteer and A. P. Evan, “The acute and long-term adverse effects of shock wave lithotripsy,” in *Seminars in nephrology*, vol. 28, no. 2. Elsevier, 2008, pp. 200–213.
- [124] F. Recker, A. Bex, W. Hofmann, G. Uhlschmid, and R. Tscholl, “Pathogenesis and shock wave rate dependence of intrarenal injury from extracorporeal lithotripsy,” *Journal of Endourology*, vol. 6, no. 3, pp. 199–204, 1992.
- [125] G. Schelling, M. Delius, M. Gschwender, P. Grafe, and S. Gambihler, “Extracorporeal shock waves stimulate frog sciatic nerves indirectly via a cavitation-mediated mechanism.” *Biophysical journal*, vol. 66, no. 1, p. 133, 1994.
- [126] K. A. Al-Awadi, E. O. Kehinde, I. Loutfi, O. A. Mojiminiyi, A. Al-Hunayan, H. Abdul-Halim, A. Al-Sarraf, A. Memon, and M. P. Abraham, “Treatment of renal calculi by lithotripsy: minimizing short-term shock wave induced renal damage by using antioxidants,” *Urological research*, vol. 36, no. 1, pp. 51–60, 2008.
- [127] Y. Aksoy, I. Malkoc, A. F. Atmaca, H. Aksoy, K. Altinkaynak, and F. Akcay, “The effects of extracorporeal shock wave lithotripsy on antioxidant enzymes in erythrocytes,” *Cell biochemistry and function*, vol. 24, no. 5, pp. 467–469, 2006.
- [128] L. Benyi, Z. Weizheng, and L. Puyun, “Protective effects of nifedipine and allopurinol on high energy shock wave induced acute changes of renal function,” *The Journal of urology*, vol. 153, no. 3, pp. 596–598, 1995.
- [129] P. V. Barbosa, A. A. Makhlof, D. Thorner, R. Ugarte, and M. Monga, “Shock wave lithotripsy associated with greater prevalence of hypertension,” *Urology*, vol. 78, no. 1, pp. 22–25, 2011.
- [130] F. R. Orozco, P. J. Iglesias, H. J. Massarrah, G. J. Mancebo, and E. E. Perez-Castro, “[renal hematoma after extracorporeal shockwave lithotripsy in a series of 324 consecutive sessions with the doli-s lithotripter: incidents, characteristics, multifactorial analysis and review].” *Archivos espanoles de urologia*, vol. 61, no. 8, pp. 889–914, 2008.

- [131] J. S. Morris, D. Husmann, W. Wilson, J. Denstedt, P. Fulgham, R. Clayman, and G. Preminger, “A comparison of renal damage induced by varying modes of shock wave generation.” *The Journal of urology*, vol. 145, no. 4, pp. 864–867, 1991.
- [132] A. E. Krambeck, M. T. Gettman, A. L. Rohlinger, C. M. Lohse, D. E. Patterson, and J. W. Segura, “Diabetes mellitus and hypertension associated with shock wave lithotripsy of renal and proximal ureteral stones at 19 years of followup,” *The Journal of urology*, vol. 175, no. 5, pp. 1742–1747, 2006.
- [133] Y. Shao, B. A. Connors, A. P. Evan, L. R. Willis, D. A. Lifshitz, and J. E. Lingeman, “Morphological changes induced in the pig kidney by extracorporeal shock wave lithotripsy: nephron injury,” *The Anatomical Record Part A: Discoveries in Molecular, Cellular, and Evolutionary Biology*, vol. 275, no. 1, pp. 979–989, 2003.
- [134] B. Sturtevant and M. Lokhandwalla, “Biomechanical effects of eswl shock waves,” *The Journal of the Acoustical Society of America*, vol. 103, no. 5, pp. 3037–3038, 1998.
- [135] C. Chaussy, E. Schmidt, and D. Jocham, “Extracorporeal shock wave lithotripsy: a new aspect in the treatment of kidney stones,” in *Current Status of Clinical Organ Transplantation*. Springer, 1984, pp. 305–317.
- [136] W. Eisenmenger, “The mechanisms of stone fragmentation in eswl,” *Ultrasound in medicine & biology*, vol. 27, no. 5, pp. 683–693, 2001.
- [137] O. A. Sapozhnikov, A. D. Maxwell, B. MacConaghy, and M. R. Bailey, “A mechanistic analysis of stone fracture in lithotripsy,” *The Journal of the Acoustical Society of America*, vol. 121, no. 2, pp. 1190–1202, 2007.
- [138] “Ansys academic research, release 17.1, help system, coupled field analysis guide, ansys, inc.” 2016.
- [139] A. K. Singhal, H. Y. Li, M. M. Athavale, , and Y. Jiang, “Mathematical basis and validation of the full cavitation model,” *ASME FEDSM’01, New Orleans, Louisiana, USA*, 2001.

- [140] P. J. Zwart, A. G. Gerber, and T. Belamri, “A two-phase flow model for predicting cavitation dynamics,” *In Fifth International Conference on Multiphase Flow, Yokohama, Japan, 2004*.
- [141] G. H. Schnerr and J. Sauer, “Physical and numerical modeling of unsteady cavitation dynamics,” *In Fourth International Conference on Multiphase Flow, New Orleans, USA, 2001*.
- [142] H. Lee, H. Yoon, and M. Ha, “A numerical investigation on the fluid flow and heat transfer in the confined impinging slot jet in the low reynolds number region for different channel heights,” *International Journal of Heat and Mass Transfer*, vol. 51, no. 15-16, pp. 4055–4068, 2008.
- [143] P. J. Roache, “Verification and validation in computational science and engineering,” *Hermosa Publishers, Albuquerque*, vol. 1, pp. 8–9, 1998.
- [144] D. Chisholm, “Two-phase flow in pipelines and heat exchangers,” *Longman Group Ed., London, UK, 1983*.
- [145] W. H. Nurick, “Orifice cavitation and its effect on spray mixing,” *ASME Journal of Fluid Engineering*, vol. 98, pp. 681–687, 1976.
- [146] V. Srinivasan, A. J. Salazar, and K. Saito, “Numerical simulation of cavitation dynamics using a cavitation-induced-momentum-defect (cimd) correction approach,” *Applied Mathematical Modelling*, vol. 33, no. 3, pp. 1529–1559, 2009.
- [147] S. Kline and F. McClintock, “Describing uncertainties in single-sample experiments,” *Mechanical Engineering*, vol. 75, p. 38, 1953.
- [148] V. Moholkar and A. Pandit, “Bubble behavior in hydrodynamic cavitation: Effect of turbulence,” *AlChE Journal*, vol. 43, pp. 1641–1648, 1997.
- [149] P. Kumar, S. Khanna, and V. Moholkar, “flow regime maps and optimization thereby of hydrodynamic cavitation reactors,” *AlChE Journal*, vol. 58, pp. 3858–3866, 2012.

- [150] L. V. Wijngaarden, “on the equation of motion for mixture of liquid and gas bubbles,” *Journal of Fluid Mechanics*, vol. 33, pp. 465–474, 1968.
- [151] Y. C. Wang and C. E. Brennen, “one dimensional cavitating flows through a converging-diverging nozzle,” *ASME Journal of Fluids Engineering*, vol. 10, pp. 166–170, 1998.
- [152] R. Toegel, B. Gompf, R. Pecha, and D. Lohse, “Does water vapor prevent upscaling sonoluminescence?” *Physical Review Letters*, vol. 85, pp. 3165–3168, 2000.
- [153] J. H. Xing, A. Boguslawski, A. Soucemarianadin, P. Atten, and P. Attane, “Experimental investigation of capillary instability: results on jet stimulated by pressure modulations,” *Experiments in Fluids*, vol. 20, no. 4, pp. 302–313, 1996.
- [154] G. O. Collantes, E. Yariv, and I. Frankel, “Effects of solute mass transfer on the stability of capillary jets,” *Journal of Fluid Mechanics*, vol. 474, pp. 95–115, 2003.
- [155] M. Saroka, Y. Guo, and N. Ashgriz, “Nonlinear instability of an evaporating capillary jet,” *AIAA Journal*, vol. 39, pp. 1728–1734, 2010.
- [156] R. Suryo, P. Doshi, and O. A. Basaran, “Nonlinear dynamics and breakup of compound jets,” *Physics of Fluids*, vol. 18, no. 8, 2006.
- [157] R. W. Lockhart and R. C. Martinelli, “Proposed correlation of data for isothermal two-phase, two-component flow in pipes,” *Chemical Engineering Progress*, vol. 45, pp. 39–48, 1949.
- [158] N. Lekic and M. Birouk, “Liquid jet breakup in quiescent atmosphere: a review,” *Atomization and Sprays*, vol. 19, no. 6, pp. 501–528, 2009.
- [159] P.-K. Wu, R. F. Miranda, and G. M. Faeth, “Effects of initial flow conditions on primary breakup of nonturbulent and turbulent round liquid jets,” *Atomization and Sprays*, vol. 5, no. 2, pp. 175–196, 1995.

- [160] H. Hiroyasu, “Spray breakup mechanism from the hole-type nozzle and its applications,” *Atomization and Sprays*, vol. 10, no. 3-5, pp. 511–527, 2000.
- [161] N. Tamaki, M. Shimizu, and H. Hiroyasu, “Enhancement of the atomization of a liquid jet by cavitation in a nozzle hole,” *Atomization and Sprays*, vol. 11, no. 2, 2001.
- [162] H. Hiroyasu, “Break-up length of a liquid jet and internal flow in a nozzle,” *ICLASS-91*, 1991.
- [163] S. Gopalan and J. Katz, “Flow structure and modeling issues in the closure region of attached cavitation,” *Physics of Fluids*, vol. 12, no. 4, pp. 895–911, 2000.
- [164] W. Kim, K. Park, J. Oh, J. Choi, and H.-Y. Kim, “Visualization and minimization of disruptive bubble behavior in ultrasonic field,” *Ultrasonics*, vol. 50, no. 8, pp. 798–802, 2010.
- [165] J. P. Dear, J. E. Field, and A. J. Walton, “Gas compression and jet formation in cavities collapsed by a shock wave,” *Nature*, vol. 332, pp. 505–508, 1988.
- [166] C.-D. Ohl, M. Arora, R. Dijkink, V. Janve, and D. Lohse, “Surface cleaning from laser-induced cavitation bubbles,” *Applied Physics Letters*, vol. 89, no. 7, 2006.
- [167] S. Arrojo and Y. Benito, “A theoretical study of hydrodynamic cavitation,” *Ultrasonics Sonochemistry*, vol. 15, no. 3, pp. 203–211, 2008.
- [168] E. Brujan, T. Ikeda, K. Yoshinaka, and Y. Matsumoto, “The final stage of the collapse of a cloud of bubbles close to a rigid boundary,” *Ultrasonics sonochemistry*, vol. 18, no. 1, pp. 59–64, 2011.
- [169] G. L. Chahine, A. Kapahi, J.-K. Choi, and C.-T. Hsiao, “Modeling of surface cleaning by cavitation bubble dynamics and collapse,” *Ultrasonics Sonochemistry*, vol. 29, pp. 528–549, 2016.
- [170] F. Su, X. Ma, and J. Chen, “Effect of nanoparticles on forming process of bubbles in a nanofluid,” *ASME 2009 Second International Conference on Micro/Nanoscale Heat Mass Transfer*, pp. 425–430, 2009.

Curriculum Vitae and Publications

Personal information

Name: Morteza Ghorbani
Date of birth: August 11th, 1986
Nationality: Iranian

Journal Publications

[1] **Morteza Ghorbani**, Abdolali Khalili Sadaghiani, Mehmet Yildiz and Ali Kosar, "Experimental and Numerical Investigations on the Spray Collapse under the Effect of Cavitation Phenomenon in a Microchannel", *J Mech Sci Tech*, 31, 1-13, 2017.

[2] **Morteza Ghorbani**, Ozlem Oral, Sinan Ekici, Devrim Gozuacik and Ali Kosar, "Review on Lithotripsy and Cavitation in Urinary Stone Therapy", *IEEE Rev Biomed Eng*, 9, 264-283, 2016.

[3] **Morteza Ghorbani**, Gokhan Alcan, Mustafa Unel, Asf Sabanovic, Huseyin Uvet, Devrim Gozuack and Ali Kosar, "Visualization of microscale cavitating flow regimes via particle shadow sizing imaging and vision based estimation of the cone angle", *Exp Thermal Fluid Sci*, 78, 322-333, 2016.

[4] **Morteza Ghorbani**, Mehmet Yildiz, Devrim Gozuack and Ali Kosar, "Cavitating Nozzle Flow in Micro and Mini Channels under the Effect of Turbulence", *J Mech Sci Tech*, 30, 2565-2581, 2016.

[5] Gokhan Alcan, **Morteza Ghorbani**, Ali Kosar and Mustafa Unel, "A New Visual Tracking Method for the Analysis and Characterization of Jet Flow", *Flow Meas Instrum*, 51, 55-67, 2016.

[6] Mehrdad Karimzadehkhoei, **Morteza Ghorbani**, Kursat Sendur, M. Pinar Menguc, Yusuf Leblebici and Ali Kosar, "Increasing the Stability of Nanofluid with Cavitating Flows in Microorifices", *Appl Phys Lett*, 109 (10), 104101, 2016.

[7] **Morteza Ghorbani**, Gokhan Alcan, Ali Mohammadi, Abdolali Khalili Sadaghiani, Mustafa Unel and Ali Kosar, "Spray Behavior due to Bubbly Cavitating Flows in Micro Orifices", *Int J Multiphas Flow*, Under Review.

Book Chapters

[1] **Morteza Ghorbani**, Gokhan Alcan, Dilara Yilmaz, Mustafa Unel, and Ali Kosar, "Visualization and Image Processing of Spray Structure under the Effect of Cavitation Phenomenon", *IOP J Phys: Conf Ser*, 656, 012115, 2015.

[2] Gokhan Alcan, **Morteza Ghorbani**, Ali Kosar, and Mustafa Unel, "Single Droplet Tracking in Jet Flow", *ICIAR 2016*, LNCS 9730, pp. 18, 2016.

Conference Papers

[1] Gokhan Alcan, **Morteza Ghorbani**, Ali Kosar, Mustafa Unel, "Vision Based Cone Angle Estimation of Bubbly Cavitating Flow and Analysis of Scattered Bubbles using Micro Imaging Techniques", *41st Annual Conference of the IEEE Industrial Electronics Society (IECON2015)*, Yokohama, Japan, November 9-12, 2015.

[2] **Morteza Ghorbani**, Ali Koar, "Visualization of Spray Structure at the Outlet of the Micro Orifices", *InterPACKICNMM2015-48304, Proceedings of the ASME 2015 International Technical Conference and Exhibition on Packaging and Integration of Electronic and Photonic Microsystems and ASME 2015 12th International Conference on Nanochannels, Microchannels, and Minichannels InterPACK-ICNMM2015*, San Francisco, California, USA, July 6-9, 2015.

[3] **Morteza Ghorbani**, Ali Kosar, "Collapse of the Cavitation Bubbles at the Outlet of Microchannels", *Smart and Green interfaces Conference-2015 and Annual MC meeting COST MP 1106*, Belgrade, Serbia, March 30th to April 1st 2015.